Impact of Structural Modifications on Ultrafast Correlation-Driven Charge Migration in Organic Molecules: For Molecular Engineering

PhD Thesis

Kalyani Chordiya

University of Szeged

Doctoral School of Physics

Impact of Structural Modifications on Ultrafast Correlation-Driven Charge Migration in Organic Molecules: For Molecular Engineering

PhD Thesis

Kalyani Chordiya

Supervisor

Mousumi Upadhyay Kahaly (PhD)

ELI-ALPS, Wolfgang Sandner utca 3, H-6728 Szeged, Hungary

Co-advised by

Prof. Alexander I. Kuleff

Theoretische Chemie, Physikalisch-Chemisches Institut (PCI), Universität Heidelberg, Im Neuenheimer Feld 229, 69120 Heidelberg, Germany

Doctoral School of Physics

Institute of Physics

University of Szeged

Faculty of Science and Informatics

2022

Szeged

This thesis is dedicated to my parents.

Contents

1 Introduction **7**

2 Theory **15**
- 2.1 Hartree Fork (HF) approximation 16
- 2.2 Density functional theory (DFT) 17
- 2.3 Green's function method 18
- 2.4 Algebraic diagrammatic construction (ADC) 19
- 2.5 Charge migration dynamics 20
- 2.6 Vibronic coupling Hamiltonian (VCH) 20
- 2.7 The multiconfiguration time-dependent Hartree (MCTDH) method 23
- 2.8 Laser-induced alignment and orientation: the TDSE method 24

3 Insights Into Intramolecular Charge Transfer: An Ab Initio Approach **27**
- 3.1 Motivation 27
- 3.2 Computational method 29
- 3.3 Results and discussions 30
- 3.4 Summary and conclusions 33

4 Attosecond to Femtosecond Pure Charge Migration Dynamics **35**
- 4.1 Methods 36
- 4.2 Photo-ionization spectra 36
- 4.3 Clocking the sudden ionization response time 37
- 4.4 Femtosecond charge migration dynamics 40

5 The Effect of Different Molecular Structures on CMD **47**
- 5.1 DNA nucleobases 48
- 5.2 Pi-spacers 56
- 5.3 Summary and conclusions 58

6 Non-adiabatic Dynamics **63**
- 6.1 Electronic structure calculations 64
- 6.2 VCH and MCTDH 64

7 Laser-Induced Alignment Dynamics **69**
- 7.1 Computational method 70
- 7.2 Results and discussions 70
- 7.3 Summary and conclusions 74

8 Summary and Outlook 77

9 Magyar nyelvű összefoglaló 81

Publications 85

Bibliography 90

List of Figures

1.1 Summarized results from various studies discussed in this thesis. (Left panel) Results showing the difference in response time for keto-enol tautomers of uracil, to sudden ionization in the attosecond timescale and the difference in the charge migration dynamics in the sub-*fs* timescale. (Right panel, upper block) The difference in charge migration between the cis and trans isomers of cytosine. (Right panel, lower block) Comparison of the charge migration dynamics in the non-aromatic cyclopentadiene and aromatic 1,2,3-benzothiadiazole molecules. 12

3.1 (I) Schematics of DSSC with electron transfer processes and the associated time scales involved. (II) Structure and the experimentally reported power conversion efficiency (PCE) of dye (a) ADEKA1. Atom colours: C (dark grey), S (golden), O (red), N (blue), H (light grey). 28

3.2 Difference between the excited (red) and cationic state (blue) bond lengths, with respect to the ground state. The values Δ >0.01 Å are marked with "*". The boxes highlighted in red and blue indicate changes for the acceptor group and the donor groups, respectively. 32

3.3 The distance measured between the donor and acceptor group of ADEKA1 in three states: ground state, excited state and cationic state. The blue highlighted boxes show the variation in the planar acceptor anchoring site, while the red boxes show the variations for the donor group. 32

4.1 Ionization spectra of (a) keto and (b) enol, with the corresponding molecular structures in inset. 37

4.2 Evolution of the hole-occupation numbers $\tilde{n}_i(t)$ for the first 200 as, after ionization of the five highest occupied molecular orbitals. The response time for each orbital is marked ("*") at the first stationary point in the corresponding $\tilde{n}_i(t)$ curve. 38

4.3 HOMO to HOMO-6 orbitals in a$''$ and a$'$ symmetry for keto-**U** (upper row) and enol-**U** (lower row) (iso-surfaces of 0.02 e/Å^3). 38

4.4 Iso-surface of the hole density at 10 *as*, 30 *as* and 60 *as* after the sudden ionization of the two outermost molecular orbitals in a$'$ symmetry, (a, b) in keto-**U**, and (c, d) in enol-**U**. The iso-surfaces in blue and red represent hole and electron density, respectively. Decreasing opacity is used to indicate the different iso-surface values: ± 0.0128 arb. units, ± 0.0032 arb. units and ± 0.0008 arb. units. 39

4.5 Iso-surface of the hole density at 10 *as*, 30 *as* and 60 *as* after the sudden ionization of the two outermost molecular orbitals in the a$''$ symmetry, (a, b) in keto-**U**, and (c, d) in enol-**U**. The iso-surfaces in blue and red represent hole and electron density, respectively. Decreasing opacity is used to indicate the different iso-surface values: $\pm$ 0.0128 arb. units, $\pm$ 0.0032 arb. units and $\pm$ 0.0008 arb. units). 40

4.6 Rate of change in hole density, $dQ(\vec{r},t)/dt$, at selected molecular sites. Blue dash-dot line for O7, light blue dotted line for N3, orange solid line for N1, purple dashed line for C5, brown dash-dot line for Ht, and light blue dashed line for O8. 41

4.7 The temporal evolution of hole density after the photo-ionization of (a) HOMO-4, (b) HOMO-5, of keto-**U** (iso-value 0.01 e/Å^3, hole density in green and electron density in orange), (c) HOMO-4, (d) HOMO-6 of enol-**U** (with an iso-value of 0.03 charge/Å^3). The coloured circles surrounding the iso-surface represent the corresponding molecular orbitals contributing during charge migration. 43

4.8 Snapshots of the averaged temporal hole density at 0.0 *fs*, 1.2 *fs*, 2.8 *fs*, and 4.4 *fs* after the photo-ionization of orbitals in a$''$ (top row) and a$'$ (bottom row) symmetry of keto (left panel) and enol (right panel). The brown iso-surface (0.005 a.u.) and the yellow iso-surface (-1×10^{-6} a.u.) represent hole density and electron density, respectively. 44

5.1 Molecular structures of different tautomers of DNA nucleobases, (a) **A**, (b) **T**, (c) **G**, and (d) **C**. The black circle highlights the position of the tautomeric hydrogen. The numbering of atoms is given for each parent nucleobase (**A, T, G, C**) and it remains the same for the corresponding tautomeric forms. 47

5.2 Ionization spectra for the tautomers of adenine 48

5.3 CMD in adenine tautomers in 5 *fs* after the ionization of the HOMO-7 molecular orbital. 49

5.4 Ionization spectra for the tautomers of thymine 50

5.5 CMD in thymine tautomers in 5 *fs* after the ionization of HOMO-6. 51

5.6 Ionization spectra for the tautomers of guanine 52

5.7 CMD in guanine tautomers in 5 *fs* after the ionization of HOMO-7. 53

5.8 Ionization spectra for the tautomers of cytosine 55

5.9 CMD in cytosine, and the cis-trans isomers of enol-cytosine in 5 *fs* after the ionization of HOMO-5. 56

5.10 CMD in cis-trans isomers of imino-cytosine at 1 *fs* to 5 *fs* after the ionization of HOMO-5. 57

5.11 Molecular structure for (a) pyrrole, (b) cyclopentadiene, (c) 2,1,3-benzothiadiazole, (d) furan, (e) thiophene, (f) 1,2-thiazole and (g) 1,2,5-thiadiazole. 57

5.12 Ionization spectra up to 25 *eV* for (a) pyrrole, (b) cyclopentadiene, (c) 2,1,3-benzothiadiazole, (d) furan, (e) thiophene, (f) 1,2,5-thiadiazole, (g) 1,2-thiazole. The contribution from the HOMO to HOMO-7 orbitals in the ionization spectra are represented by coloured lines, while the rest is given in black. 59

5.13 CMD in (a) HOMO-4 of pyrrole, (b) HOMO-1 of cyclopentadiene, (c-d) HOMO-2 and HOMO-4 of 2,1,3-benzothiadiazole, (e-f) HOMO-2 and HOMO-3 of furan, (g) HOMO-3 of thiophene, (h) HOMO-4 of 1,2-thiazole and (i-j) HOMO-3 and HOMO-4 of 1,2,5-thiadiazole; within 5 *fs* after the ionization of the corresponding molecular orbitals. 60

6.1 Vibration spectra for the uracil molecule calculated with the MP2/LANL2DZ method. 64

6.2 Comparison of the individual single-point energy (dots: non-Dyson ADC(3) method) and potentials energy curves fitted with the adiabatic model (lines) for the normal coordinates of the selected vibrational modes. 66

6.3 The non-adiabatic state population dynamics for all twelve states of U^+. The first four panels show the population transfer in modes (a) ν_1, (b) ν_5, (c) ν_7 and (d) ν_9. (e) The dynamics with the combination of the ν_1, ν_5, and ν_7 modes. (f) The dynamics for the combination of ν_1 to ν_{10} modes. 67

7.1 Alignment dynamics with varying (a) Temperature, (b) FWHM and (c) Intensity. The maximum value for alignment during each variation is given in: (d) Temperature, (e) FWHM and (f) The range of the varying parameters for an 800 *nm* pulse are given in Table. 7.2 and the laser pulse is at 5 *ps*. 71

7.2 Rotational states excited after varying the pulse duration for an 800 *nm* pulse. Other pulse parameters are given in Table. 7.2 72

7.3 For the highest achieved alignment presented in Fig. 7.1 the population of the rotational states $|J, M\rangle$ are given: (a) temperature of 0 K (b) 150 *fs* FWHM and (c) Intensity of 100 TW/cm^2. 73

7.4 Temporal population distribution for different J states ($\sum_K |C_{J,K,M=0}(t)|^2$) for FWHM = 500 *fs*, 200 *fs* and 100 *fs* (going from top to bottom). The centre of the pulse is at 5 *ps*. 73

List of Tables

3.1 Presence of different types of fused groups such as D, π-spacer and A group in dye, calculated values of the reorganization energy for electron (λ_e), hole (λ_h), total (λ) and difference in reorganization energy ($\lambda' = \lambda_e - \lambda_h$) in *eV*, for ADEKA1 ("NA" means not applicable) 29
3.2 Calculated values for the absorption peaks (λ, nm), molecular orbital transitions, oscillator strength (OS) and excitation lifetime τ (*ns*) for ADEKA1. 31
3.3 Changes in the structural parameters of ADEKA1 for bond angle (A,°) and dihedral angle (D,°) in the excited state (ΔE) and the cationic state (ΔC) with respect to the ground state. 33

4.1 The overall electronic response time to the removal of an electron from the five outermost molecular orbitals of keto-**U** and enol-**U**, and the maximum-variation time (τ) at the atomic site with the highest charge density response is given in brackets. 40

6.1 Frequency and symmetry for the normal modes of the **U** molecule. 65
6.2 Single-particle functions (SPF) and the number of primitive basis functions for modes 1 to 10 for the uracil cation. 65

7.1 The tunable range of the experimentally feasible pulse parameters for 800 *nm* . . . 69
7.2 The alignment dynamics presented in Fig. 7.1 with varying ("*") 800 *nm* pulse parameters. Here we vary the marked parameter keeping the others fixed during the simulations. 70

Chapter 1

Introduction

In the natural world we can witness many different photo-chemical or photo-catalytic reactions governing photosynthesis, radiation damage, gene mutation and many other biological processes. The understanding and artificial replication of these processes can help humankind in the development of new chemical synthesis techniques and in the generation of clear energy. All these processes are mainly dependent on the quantum chemical dynamics of electrons and nuclei. This dependence is due to the overlaps between the atomic orbitals, which determine the formation of molecular bonds that control the mobility of charge and hence the reaction processes. Therefore, investigation of the relation between the migration of charge and the rearrangement of nuclei is of fundamental interest. Energy absorption by a molecule during such photo-induced processes results in physical and chemical changes such as: charge transfer, fluorescence, structural transformations, or fragmentation dynamics. To foresee them it is also essential to thoroughly understand the molecular properties in the ground, excited and ionic states. In addition to photons, molecular orbitals excitation can be further influenced by the different external factors such as solvent, temperature, or intermolecular interactions. Understanding the molecular response under different conditions will also foster efficient molecular designing, which will boost the integration of organic molecules for optoelectronic devices[1, 2], organic or hybrid solar cells[3]; in drug delivery[4], tumour cell detection[5]; to name a few. The biggest question researchers now face is how to trigger, trace and control these responses? It is also important to note the timescales involved in studying each of these processes, which can vary from the attosecond (*as*, 10^{-18} *s*) to the femtosecond (*fs*, 10^{-15}s) timescales.

The timescales involved in the various responses are important as, initially, within a few *fs*, before the onset of nuclear motion, one can observe only pure charge migration dynamics. Due to their light mass, electrons move very rapidly in comparison to nuclei. Hence, from the *as* to the sub-*fs* timescales one can safely ignore the motion of the nuclei. Beyond the sub-*fs* timescale, the motion of the electrons starts to couple with the nuclei and this coupled electron-nuclear dynamics eventually leads to the rearrangement of nuclear positions within the molecule. To study the above mentioned motions, one needs to understand various electronic structures, vibrational modes, and electron-nuclei coupled interactions for a given system. Additionally, to measure these motions one needs extremely advanced, higher resolution techniques capable of capturing such ultrafast dynamics. Note that tracing such ultrafast processes both theoretically and through experimental techniques is not trivial.

Over the years, with the advancements in laser sources, one has become able to achieve temporal resolution as well as spatial resolution at the atomic scales. Lasers can be used not only for exploring the fundamental properties of charge dynamics, but also to control them. Lasers can also be used for freezing an atomic or molecular system far from its equilibrium and for observing the real-time vibrational motion in[6]. Using a laser pulse to steer a chemical reaction in desired channel is today called “femtosecond chemistry”, which has become a very well established field of research. The persistent efforts to understand and visualize the motion of charge in the real-time gave birth to something we today call “attosecond science”. A new paradigm in the field of attosecond science or chemistry is to use charge dynamics and quantum interference to influence chemical reactions. The investigation of such dynamics experimentally is an extremely challenging task. Until now, several different schemes have been employed to study the charge migration dynamics for molecular systems both in gaseous and liquid phases[7]. These experiments have demonstrated that the charge migration dynamics can be captured and reconstructed indirectly by measuring the yield of fragments[8] for doubly positively charged molecular ions at different delays between XUV and IR pulses, or directly via high harmonic generation using intense ultrashort laser pulses [9, 10, 11, 12]. To access and control the electron motions at such an ultrafast timescale can possibly be central for the optimization of the charge transfer routes in a molecule in a pre-determined, tailored manner. Dedicated research efforts – resulting in sophisticated models which can then trace the charge dynamics based on the observation of fragmentation channels – were initially reported by R. Weinkauf et al.[8]. Incorporation of the aligned molecules to measure the high harmonic signal was reported by P. Kraus et. al. to reconstruct charge migration dynamics[13]. In this report they measured the high harmonic spectra for the same molecule with different angles between the aligned molecules and laser pulse polarization. Current state-of-the-art HHG-driven *as* XUV setups for XUV-pump–XUV-probe experiments are yet to overcome certain bottlenecks for full implementation. There are a few facilities around the world, including ELI ALPS[14], and XFEL[15, 16] that have the potential to host such experiments in the near future. Such experiments can help understand the correlated charge migration dynamics and electron-nuclei coupled non-adiabatic charge dynamics in real-time.

Theoretical developments have played an important role in the advancement of attosecond and femtosecond science. With theoretical advancements in density functional theory (DFT) and time-dependent density functional theory (TDDFT), it is now possible to study the intramolecular or intermolecular charge transfer for larger systems ($>$100 atoms) in the static regime[17]. Further developments are in progress to study the charge transfer dynamics by investigating the crossing between the potential energy curves[18]. Such methods have been very useful, and showed promising results. A huge advantage of using the DFT method is the possibility to handle larger systems in a realistic environment. This is particularly important when the basic electronic, or vibrational properties of the system are to be explored. For example, using DFT based calculations one can create databases for electronic and structural properties for a large number of molecules. These databases can be further evaluated to select effective systems for photo-induced charge transfer processes[19]. These databases can also be used for machine learning and for further molecular modelling[3, 20, 21]. However, it is important to note that the usual DFT approach, and the resulting databases are based on ground state electronic properties, and do not shed light on the temporal evolution of the electronic cloud during different chemical processes, and lack information on real-time charge migration dynamics.

The pioneering work by Cederbaum and Zobeley paved the way for studying real-time ultrafast charge migration study[22]. Their results showed that the removal of charge from a molecular orbital can lead to the creation of an electron wavepacket. This electron wavepacket (in static nuclei approximation) is created by the excitation of several cationic states simultaneously. Furthermore, this wavepacket can be evolved in time. Using this method, several bio-relevant and astronomically important molecules have been studied over the past few years. In a report by A. Marciniak et al., polycyclic aromatic hydrocarbons (PAHs) were studied using experimental and theoretical methods[23]. In this report ultrafast relaxation in few tens of femtoseconds was measured[23]. This study shows the transfer of energy from the electronic to vibrational degrees of freedom. This ultrafast charge migration method has also been used in the development of molecular modelling by V. Despre et. al., who studied the effect of carbon chain on the charge migration time[24].

I start my thesis by presenting our results about intramolecular charge transfer in large systems ($>$100 atoms) used in dye sensitized solar cells with the DFT and TDDFT methods. With these methods I show how the variation in the structural parameters play a critical role in understanding the correlation between photo-excitation and charge redistribution processes. Our approach helps in obtaining a preliminary understanding of the extent of π-conjugation in an extended system. It is important to note that the proposed approach is computationally cost-effective and can handle large systems, and can be used widely to study the molecules used in photovoltaic, sensors and opto-electronic devices. With this approach one can study the linear response of the system in static nuclei approximation. Then I present our results on ultrafast charge migration to investigate real-time charge migration dynamics (CMD). I have studied several molecules to address the effect of chemical and structural variations on the charge migration dynamics. For this study, I have applied an advanced theoretical method which takes into account the correlation effect during the CMD, using the ADC code, which was developed by the group of Lorenz S. Cederbaum at the University of Heidelberg, Germany. This code can be used to propagate charge density after sudden ionization, and to trace pure charge migration in the *as* to *fs* timescale.

The ultrafast charge dynamics was initiated by the sudden ionization of the molecule. Then the effect of symmetry and role of tautomeric hydrogen on the response time of different orbitals was studied in the *as* timescale. Furthermore, I investigated the CMD in smaller systems such as five nucleobases in RNA and DNA, their tautomers and isomers, along with seven different π-spacer systems to understand the effect of tautomeric hydrogen, cis-trans forms, methylation and aromaticity on pure CMD. The observations of these studies can be used as general molecular modelling rules. These rules can be applied to modify charge delocalization in a given system. Pure CMD can last for $\sim$ 3 *fs* or longer. After 3 *fs*, nuclear dynamics can come into the picture and result in non-adiabatic dynamics, which can eventually promote the fragmentation process. Hence, to study electron-nuclei coupled non-adiabatic dynamics I used the linear vibronic coupling (LVC) model. With the LVC model I constructed the vibronic coupling Hamiltonian, and used the multiconfiguration time-dependent Hartree (MCTDH) method to study time evolution and population transfer between the excited electronic states. I present the results for the nuclear coupled non-adiabatic dynamics in coherently ionized states. These methods help us take into account the electron-nuclei coupled cationic states, which can be excited by an attosecond pulse. Based on this study we check the feasibility of the uracil molecule to investigate the charge migration process experimentally. For the experimental measurements we need an advanced XUV-pump–XUV-probe setup which will be available in advanced facilities like ELI ALPS. Until now, these dynamics were measured experimentally, with fragmentation dynamics, attosecond transient absorption spectroscopy and self-probing using high harmonic generation from the studied molecular systems. To investigate real-time CMD with ultrashort lasers, the alignment and orientation of molecules must have a high signal to noise ratio. Hence, using CH_3F as a prototype molecule I presented a study to improve the alignment dynamics with experimentally feasible pulse parameters and conditions.

After the introduction to the thesis in this chapter, I provide a brief summary on the following chapters:

Chapter 2

In this chapter I will briefly describe the different quantum mechanical approaches I have used in the simulation of ultrafast molecular processes. Using these simulations I have calculated the photo-induced charge transfer and charge migration dynamics in molecules. I start with the theoretical background for the DFT and TDDFT based simulations used in this thesis to calculate the intramolecular charge transfer in large molecular systems. Using these methods, the molecular structural parameters are analyzed to determine the overall charge transfer in an extended molecular system. The results for the charge transfer in a large molecule are given in Chapter 3. Followed by this, I give a brief theoretical description for the single particle non-Dyson Green's function ADC(3) method used in the calculation of pure photo-ionization induced CMD in a small molecules. The results obtained by calculating the ultrafast charge migration dynamics using the non-Dyson ADC(3) method are given in Chapter 4 and Chapter 5. Then, the theory behind the linear vibronic coupling model to couple electron and nuclear dynamics is discussed. This theory is applied to study non-adiabatic ultrafast dynamics in a uracil molecule, and the results are presented in Chapter 6. In performing experimental studies, the molecular alignment and orientation for such complicated systems is a very important factor. Hence, I describe the theory used for studying the laser-induced alignment and orientation dynamics in this chapter, and present the results for molecular alignment and orientation in Chapter 7.

Chapter 3

In organic or hybrid solar cells or organic LEDs, efficient photo-induced intramolecular charge transfer (ICT) is one of the key factors in achieving high device efficiency. In this chapter I discuss in detail a novel and cost-effective way to understand the ICT process in photo-excited dye molecules. In this study I analyze the electronic and structural properties of a chosen experimentally synthesized donor-acceptor (D-A) type dye molecule in its ground, excited, and cationic states. The correlation between structural modification and charge redistribution in different parts of the molecule helps identify the extent of π-conjugation and the spatial rearrangement of electron density localization along the molecular skeleton. I have found that the prominent change in bond length, bond angle, and the twisting of several groups promote efficient donor to acceptor ICT. Thus, based on the modest computation of the structural and electronic properties of dye molecules in their respective ground, excited, and cationic states, I identify the structural changes that facilitate tunable intramolecular charge transfer to highlight a simple and direct "recipe" to screen out probable efficient dye molecules among many samples.

Chapter 4

The motion of the electrons in a molecular system is correlated with the long-range Coulomb interaction. Hence, perturbation applied to an electron is experienced by the entire electronic cloud in a largely extended system. This dramatic response of the charge particles can lead to prominent rearrangements in the electronic and structural properties. In the recent years, electron correlation and the processes driven by it, i.e. autoionization [25], population of satellite states on photo-ionization [26], energy transfer [27, 28], and charge migration [22, 29]; have been the subject of intensive research both by theory and experiment. The correlation effects can be used to answer the following important questions: How long does it take the electronic cloud to respond to such perturbation? Can the response time be tuned by small structural modifications? Can we use the results of these studies to design new materials? and so on. In their seminal paper[30], Breidbach and Cederbaum concluded that irrespective of the system, the global response time taken by the hole density after the sudden removal of an electron is around 50 *as*. Although this time is universal, it is certainly not the shortest response time and can vary depending on the degree of correlation [31].

In this chapter I present the ultrafast multi-electron dynamics in uracil (**U**) after XUV photo-ionization. **U** neutral molecule is observed in C_s symmetry, which has two irreducible symmetries (a' and a''). From our study we find that the response time or the charge migration for orbitals in a' symmetry does not show a prominent difference, whereas the orbitals with a'' symmetry show a prominent difference. Next, in the first few femtoseconds, charge migration dynamics is dominated by the correlation effect[22, 32]. We use the two stable tautomers of **U** and analyze the difference in their response time. This leads us to investigate how small structural modifications can actually impact this electron-correlation based mechanism (see Fig.1.1 for highlighted results). In this chapter we also present our results for specific correlation-driven CMD, initiated by the ionization of individual molecular orbitals. It can be later realized that tautomerism is one of the promising paths for the development of an appropriate molecular design for the desired charge migration [24]. This chapter also serves as a general proposition to understand the analysis of the ionization spectra, CMD and to identify the role of molecular structural and electronic properties. This understanding will be further used in analyzing more systems to be presented in Chapter 5.

Chapter 5

To unravel the photo-damage of RNAs, DNAs, and bio-molecules in general, or to study the effective charge migration capability of the system we must have a complex understanding of the response of molecules to ionization by XUV-UV radiation[33, 34, 35]. Some of the effects can be irreversible and lead to alterations or permanent damage in the DNA or RNA. Permanent damage can be caused by ring-opening photo-chemical reaction on nucleobases, fragmentation [36], or the initialization of other chemical reactions with the molecules in the environment[37]. There can be photo-protective effects which can be observed through the evolution of hole density with σ to π-type character, and can result in other non-fragmentation pathways leading to tautomerization or isomerization[38, 39]. In fact, many molecular systems in nature display multiple elements of symmetry and tautomeric forms, stereoisomers, functionalization of system by methylation, which impact their photo-chemical response. Prior to the photo-excitation or ionization induced detrimental excited-state reactions, the initial response is dominated by pure electron dynamics, with timescales typically up to a few *fs*. These are presented in Chapter 4 and Chapter 5, and studied using the electron correlation effect. This ultrafast response to external perturbation results in the rearrangement of the electronic cloud, which can dictate the relaxation pathways of the molecule. Hence, in this chapter we present an extensive and computationally expensive study where we investigate the effect of tautomers, stereoisomers, methylated system, and different elements and groups on the cyclic molecules (see Fig.1.1 for highlighted results). The pure charge migration process can last for a short time (typically $<$15 *fs*). Hence, in Chapter 6 we present the results for non-adiabatic charge migration dynamics on these correlated systems.

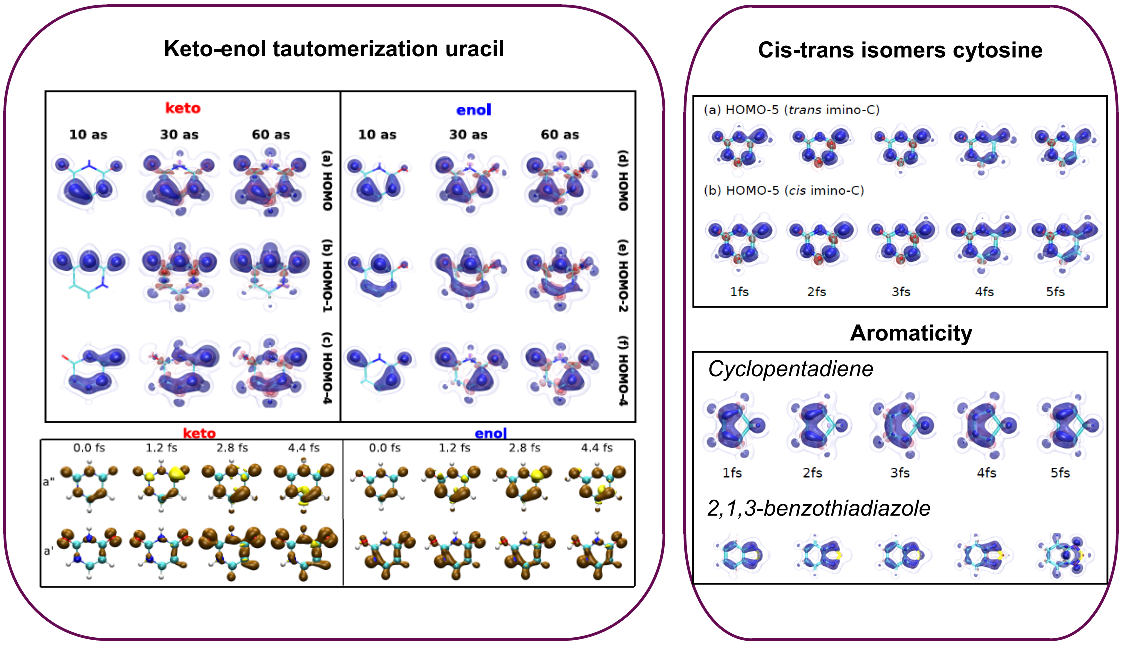
Keto-enol tautomerization uracil
keto
enol
10 as
30 as
60 as
(a) HOMO
(b) HOMO-1
(c) HOMO-4
(d) HOMO
(e) HOMO-2
(f) HOMO-4
0.0 fs
1.2 fs
2.8 fs
4.4 fs
a"
a'
Cis-trans isomers cytosine
(a) HOMO-5 (trans imino-C)
(b) HOMO-5 (cis imino-C)
1fs
2fs
3fs
4fs
5fs
Aromaticity
Cyclopentadiene
2,1,3-benzothiadiazole

Figure 1.1: *Summarized results from various studies discussed in this thesis. (Left panel) Results showing the difference in response time for keto-enol tautomers of uracil, to sudden ionization in the attosecond timescale and the difference in the charge migration dynamics in the sub-fs timescale. (Right panel, upper block) The difference in charge migration between the cis and trans isomers of cytosine. (Right panel, lower block) Comparison of the charge migration dynamics in the non-aromatic cyclopentadiene and aromatic 1,2,3-benzothiadiazole molecules.*

Chapter 6

The population of the excited states and the correlated charge dynamics can vary depending on the laser pulse used, which can lead to different charge migration dynamics. Note that charge migration is the process in which charge oscillation occurs between two atomic sites in a molecule whereas, the process of charge transfer involves the transfer of charge from electronic to nuclear degrees of freedom. Using the pure charge migration dynamics, we can observe the two atomic sites in a molecule between which the charge oscillates. These oscillations will initial the electron-nuclei coupled non-adiabatic dynamics, which will ultimately lead to charge transfer in the system and/or fragmentation. Before going from charge migration to charge transfer we need to understand the non-adiabatic dynamics. To study this we need to involve all the necessary electronic states and nuclear degrees of freedom, which can be excited by a laser pulse. In this chapter I study the non-adiabatic dynamics in an uracil cation system. For this study I used the vibronic coupling model to couple the electronic states with the nuclear degrees of freedom, which can be excited by an ultrashort laser pulse. Then I propagated the wavepacket using the MCTDH method. This gives us the information regarding the states participating in the non-adiabatic population transfer dynamics and up to how many *fs* the system shows adiabatic dynamics.

Chapter 7

Molecular alignment and orientation (A&O) techniques were extensively studied in the past for controlling photo-induced chemical reactions. Today, the increasing interest in strong-field physics, high-harmonics generation, charge migration dynamics, and molecular imaging of gaseous targets also demand high molecular alignment. In this chapter, we examine the role of all optical pulse parameters on the field-free alignment dynamics. For this study we used $\mathrm{CH_3F}$ as a prototype molecule, and selected the experimentally feasible optical laser parameters for maximal alignment. The varying parameters used for the study are: rotational temperature, pulse duration, intensity, and carrier envelop phase (CEP). Additionally, I analyzed the interplay between the laser pulse parameters and rotational population distribution. As the pulse parameters vary, the rotational revivals show two qualitatively different behaviours and I can interpret the transition by establishing the connection between the pulse parameters and the population of excited rotational states. Here I reported, using a single pulse at 2 *K*, the highest alignment of $\langle \cos^2\theta \rangle = 0.843$ for the $\mathrm{CH_3F}$ molecule.

In summary, I aim to understand and correlate the variation in charge migration dynamics with the change in molecular structure. For this study I investigated the dynamics in different timescales with appropriate quantum mechanical simulation methods. The analysis of these results is important for the development of molecular modelling. I examined how certain structural engineering of molecules can prominently impact charge reorganization over different parts of the molecular backbone, resulting in the ultrafast spatial rearrangement of electron density. I elucidated how charge transfer and charge migration critically depend on the factors such as the extent of π-conjugation, the strength of the electron correlation, arrangement of nuclei and the symmetry for the excited molecular orbitals. My analysis revealed the differences in the ultrafast charge transfer, redistribution of the electronic cloud and charge migration processes in the context of chemical and structural variations in multi-nuclear systems. In this thesis I identify the exact time when the onset of the correlation effect in the attosecond timescale is observed. Furthermore, I present the calculations for prototype systems to study the ultrafast charge migration dynamics, which can be used by the experimental groups. For experimental measurements to study charge migration dynamics, molecular alignment is an important factor as it improves the signal to noise ratio. I have included the quantum mechanical analysis to improve the alignment and orientation of poly-atomic molecules – particularly for laboratory conditions and laser parameters as available in state-of-the-art laser facilities like ELI ALPS. The summary of our analysis and outlook for the study presented in this thesis are reported in detail at the end of each chapter and in Chapter 8.

Chapter 2

Theory

Quantum chemistry calculations have helped chemists and physicists over many years in understanding the molecular structural, electronic, and vibrational properties in different environments. The quantum electronic structure calculations are based on the solution of the Schrödinger equation (SE). Solution to the SE gives the wave function (Ψ), which holds all the information about a particle in a system. A typical time-independent SE for a many-body system is given by:

$$\hat{H}\Psi = E\Psi \quad , \tag{2.1}$$

where $\hat{H}$ is a Hamiltonian operator that represents the total energy of the system.

$$H = \underbrace{-\sum_i \frac{\hbar^2}{2m_e}\nabla_i^2}_{KE\ of\ electrons} \underbrace{-\sum_i \frac{\hbar^2}{2m_A}\nabla_A^2}_{KE\ of\ nuclei} + \underbrace{\sum_{i<j}\frac{e^2}{r_i - r_j}}_{electron\ repulsion} + \underbrace{\sum_{A<B}\frac{e^2 Z_A Z_B}{|r_A - r_B|}}_{nuclei\ repulsion} - \underbrace{\sum_i\sum_A \frac{e^2 Z_A}{|r_i - r_A|}}_{electron-nuclei\ interaction} \tag{2.2}$$

The first two terms in Eq. 2.2 are for kinetic energy (KE), the next two terms are for the potential energy (PE) and the last one is for the interaction potential between the electrons and nuclei[18, 40, 41, 42, 43, 44]. Solving the exact SE given in Eq. 2.2 for a many-electron system is not trivial. Hence, we need to reduce the problem with some suitable approximations. According to the Born-Oppenheimer approximation, which is central to quantum chemistry, the nucleus moves slower compared to the electrons in a molecule, hence the terms corresponding to kinetic energy and the repulsion between the nuclei from Eq. 2.2 can be neglected[41, 44]. The remaining equation for the Hamiltonian will now be the electronic Hamiltonian, the solution to which will give the electronic wave function describing the energy and the motion of the electrons. They depend definitively on the electronic coordinates and parametrically on the nuclear coordinates. The wave function of an electron is also known as an orbital ($\Psi_i(r)$), which in case of a molecule will be called a molecular orbital. The probability (P(r)) of finding an electron in the small volume dr around r is given by $|\Psi_i(r)|^2 dr$. In case of molecules, the spatial molecular orbitals will form an orthonormal set:

$$\int_{r_1}^{r_2} dr\Psi_i^*(r)\Psi_j(r) = \delta_{ij} \quad . \tag{2.3}$$

In general, for a complete set of spatial orbitals, an arbitrary function will be expanded in the form of an infinite set, which is not practical. However, it is possible to consider a finite set of N orbitals, $\{\Psi_i | i = 1, 2, \ldots, N\}$, which spans a certain region of the complete set. Furthermore, before considering a system with interacting particles it is simple to consider a system with noninteracting particles (electrons). The Hamiltonian for such a system will take the form

$$\mathcal{H}\Psi^{HP} = E\Psi^{HP} \quad , \tag{2.4}$$

where $\mathcal{H}$ is the sum of all one-electron Hamiltonians, Ψ^{HP} is the product of all spin orbitals (orbitals with space and spin coordinates, $\chi_i(x) = \Psi(r,\sigma)$) and E is the sum of all the eigenvalues of the spin orbitals.

$$\Psi^{HP}(x_1, x_2, x_3, \dots, x_n) = \chi_1(x_1), \chi_2(x_2), \chi_3(x_3), \dots, \chi_n(x_n) \tag{2.5}$$

Such many-electron wave function given above is known as the Hartree product (HP). However, it does not satisfy the antisymmetry principle. The antisymmetrized wave function can be written in form of the Slater determinant. In this determinant, N electrons occupy N spin orbitals $(\chi_a, \chi_b, \chi_c, \dots, \chi_n)$. As it is not specified which electron occupies which orbital, on interchanging the coordinates of two electrons corresponding rows in the Slater determinant will be interchanged. Therefore, the sign of the determinant will be changed. Hence the Slater determinant satisfies the antisymmetry principle. In case two electrons occupy the same spin orbital, will give two equal columns in the determinant. Thus, the wave function vanishes if two electrons occupying the same spin orbital. The term $\sqrt{N!}$ in Eq. 2.6, is the normalization factor[45].

$$\Psi(x_1, x_2, x_3, \dots, x_N) = \frac{1}{\sqrt{N!}} \begin{vmatrix} \chi_a(x_1) & \chi_b(x_1) & \dots & \chi_n(x_1) \\ \chi_a(x_2) & \chi_b(x_2) & \dots & \chi_n(x_2) \\ \vdots & \vdots & & \vdots \\ \chi_a(x_N) & \chi_b(x_N) & \dots & \chi_n(x_N) \end{vmatrix} \tag{2.6}$$

2.1 Hartree Fork (HF) approximation

The Hartree-Fork approximation is central to solving the many-electron problem. A single Slater determinant is the determinant form of the antisymmetric wave function used to describe the ground state of a many-electron system.

$$\Phi_0 = |\chi_1 \chi_2 \cdots \chi_N\rangle \tag{2.7}$$

The variation principle[46] states that the lowest possible energy for a system is obtained with the best wave function of this functional form.

$$E_0 = \langle \Phi_0^N | \mathcal{H} | \Phi_0^N \rangle_r \tag{2.8}$$

Hence the variational flexibility is the choose of the spin orbitals in the wave function. By minimizing the energy with respect to the spin orbitals, we can derive an eigenvalue Hartree-Fork (HF) equation of the form

$$\hat{h}(i)\chi_a(x_i) = \epsilon\chi_a(x_i) \quad , \tag{2.9}$$

where $\hat{h}(i)$ includes the HF potential, which is equivalent to the "field" observed by the electron (i) and is given as

$$\hat{h}(i) = -\frac{1}{2}\nabla_i^2 - \sum_{a=1}^{O} \frac{Z_a}{r_i - R_a} + \sum_{\beta} \langle \phi_\beta(j) | \frac{1}{|r_i - r_j|}(1 - \hat{P}_{ij}) | \phi_\beta(j) \rangle_{r_j} \quad , \tag{2.10}$$

where $\hat{P}_{ij}$ is an operator that interchanges the electrons j and i between the $\phi(i)$ and $\phi(j)$ orbitals. The HF equation is a nonlinear equation solved iteratively using the self-consistent-field (SCF) method. The solution to Eq. 2.9 will yield a set of orthonormal HF spin orbitals and energies, $\{\chi_M\}$ and $\{\epsilon_M\}$[43, 45]. Subscript M is the size of the set of spatial basis functions $\{\phi_\gamma | \gamma = 1, 2, \ldots, M\}$ with 2M spin orbitals (M with α spin and M with β spin). This will give N occupied orbitals and 2M-N unoccupied orbitals. The value of E_0 will be lowered until the *Hartree-Fork* limit is reached with larger and larger basis sets.

2.2 Density functional theory (DFT)

As discussed earlier, solving an exact SE for a many-body problem is not trivial and the HF method is a good approximation. However, this method does not take into account the electron correlation effects and hence the final energy is not as low as the exact energy. The correlation effect can be incorporated by using methods based on wave function. Wave functional approaches such as the Møller-Plesset (MP) perturbation theory, or the coupled-cluster theory are quite accurate, however they cannot be applied for a very large system. On the other hand, the density functional theory (DFT) is very cost-effective, and up to a certain level it is an precise approach for large systems.

In 1964, Hohenberg and Kohn (HK) stated two important theorems[47]. The first theorem states that 'the ground state of any interacting many-particle system with a given fixed inter-particle interaction is a unique functional of the electron density $\eta(r)$'. According to which there is one-to-one correspondence between the energy of a many-body system in non-degenerate ground state and the ground-state electron density. The second theorem states that 'the electron density that minimizes the energy of the overall functional is the true electron density corresponding to the full solutions of the SE'. This means that E[$\eta(r)$] will be the minimal $\eta(r)$ when it is in its true ground-state density. The minimization of E[$\eta(r)$] can be achieved using the variation principle[43]. The relation between the ground state energy E and density in terms of the single-electron wave function $\Psi_i[\eta(r)]$ is given as

$$E[\Psi_i[\eta(r)]] = \frac{\hbar^2}{m}\sum_i \int \Psi_i^* \nabla^2 \Psi_i d^3r + \int V(r)\eta(r) d^3r + \frac{e^2}{2}\int\int \frac{\eta(r)\eta(r')}{|r - r\prime|} d^3r d^3r' + E_{ion} + E_{XC}[\eta(r)] \, . \tag{2.11}$$

The terms on the right side of Eq. 2.11 represents the KE of electrons, the electron-nuclei Coulomb interactions, the electron-electron Coulomb interactions, the nuclei-nuclei Coulomb interactions and the exchange-correlation functional. Although solving Eq. 2.11 is easier than solving the exact SE, it is still not as trivial as it sounds. This problem was further simplified by Kohn and Sham in 1965, when they showed that the energy can be given as a functional of the one-particle density (Eq. 2.12)[48, 49].

$$\Big[\frac{\hbar^2}{m}\nabla^2 + V(r) + V_H(r) + V_{XC}(r)\Big]\phi_i = \epsilon_i \phi_i \tag{2.12}$$

In Eq. 2.12, $V(r)$ is the electron-nuclei interaction potential, $V_H(r)$ is the Hartree potential ($V_H(r) =$

$e^2 \int \frac{\eta(r')}{|r-r'|} d^3r'$) and $V_{XC}(r)$ is the exchange correlation potential, $V_{XC}(r) = \frac{\delta E_{XC}(r)}{\delta \eta(r)}$. In the KS equation one needs to specify $E_{XC}[\{\phi(r)\}]$, which is cumbersome as the true form of this term is unknown. However, using theoretical or experimental considerations, an approximate exchange-correlation energy can be designed.

In 1984, Runge and Gross extended the HK theorems from static to time dependent domain. According to Runge and Gross, for a many-body system evolving from Ψ_0, one-to-one mapping between the time dependent external potential, $V_{ext}(r,t)$ and the electronic one-electron density, $\eta(r,t)$[50] exist. The time-dependent Schrödinger equation (TDSE) for the electronic ground state of a system is given by Eq. 2.13.

$$i\hbar \frac{\partial \psi(\overrightarrow{r}, t)}{\partial t} = \widehat{H} \psi(\overrightarrow{r}, t) \tag{2.13}$$

In Eq. 2.13, the Hamiltonian is given by Eq. 2.14,

$$\widehat{H} = \widehat{T} + \widehat{V}_{ee} + \widehat{V}(\overrightarrow{r}, t) \quad , \tag{2.14}$$

where $\widehat{T}$ is the kinetic energy, $\widehat{V}_{ee}$ is the electron-electron repulsion and $\widehat{V}(\overrightarrow{r}, t)$ is the external potential. For the given external potential it is possible to solve the TDSE, where the density is given by

$$n(r,t) = M \int d^3r_2 \int d^3r_3 \ldots \int d^3r_M \, |\Psi(r, r_2, \ldots, r_M, t)|^2 \quad . \tag{2.15}$$

2.3 Green's function method

We consider an N-electron system with energy E_0^N in the nondegenerate ground state $|\Psi_0^N\rangle$. For such a system, the one-particle Green's function spectral representation is given by

$$G_{pq}(\omega) = \underbrace{\sum_{m \in \{N+1\}} \frac{\langle \Psi_0^N | \hat{a}_p | \Psi_m^{N+1} \rangle \langle \Psi_m^{N+1} | \hat{a}_q^\dagger | \Psi_0^N \rangle}{\omega - (E_m^{N+1} - E_0^N) + i\eta}}_{G_{pq}^{+}(\omega)} + \underbrace{\sum_{m \in \{N-1\}} \frac{\langle \Psi_0^N | \hat{a}_q^\dagger | \Psi_m^{N-1} \rangle \langle \Psi_m^{N-1} | \hat{a}_p | \Psi_0^N \rangle}{\omega - (E_m^{N-1} - E_0^N) - i\eta}}_{G_{pq}^{-}(\omega)} \quad . \tag{2.16}$$

Here a single-particle representation is based on the HF orbitals in the ground state $|\psi_p\rangle$. In Eq. 2.16, $|\Psi_m^{N\pm1}\rangle$ has a complete sets of (N ± 1) particles eigenstates with eigenenergies $E_m^{N\pm1}$. The terms $\hat{a}_p$ and $\hat{a}_q^\dagger$ are the annihilation and creation operators, respectively. The term η is a positive infinitesimal required to define the Fourier transformation between the time and energy representations of Green's function. The first part for $G_{pq}^{+}(\omega)$ in Green's function describes a system with one extra electron, or electron affinity, while the second part ($G_{pq}^{-}(\omega)$) describes a system with one electron less, or ionization[51].

The compact matrix notation for the above equation can be given by

$$G^{\pm}(\omega) = f^\dagger (\omega - \Omega^{\pm})^{-1} f \quad , \tag{2.17}$$

where $\Omega^{\pm}$ is the diagonal matrix of the ionization energies and the electron affinities. This matrix can be expanded as:

$$\Omega_{mm}^{\pm} = \mp (E_0^N - E_m^{N\pm1}) \quad . \tag{2.18}$$

For $G^{-}_{pq}(\omega)$, the negative pole positions, which are the ionization energies of the system, are given by the difference between E^{N-1}_{m} and E^{N}_{0}, whereas the spectral amplitudes are given by

$$x_{np} = \langle \Psi^{N-1}_{m} | \hat{a}_p | \Psi^{N}_{0} \rangle \quad . \tag{2.19}$$

2.4 Algebraic diagrammatic construction (ADC)

The one-particle Green's function formalism has been used to access the accurate ionization energies and spectral intensities. This electron propagator relies on the Dyson equation to relate the Green's function **G** to the self-energy part Ξ. The Dyson equation is given as

$$G(\omega) = G^{(0)}(\omega) + G^{(0)}(\omega)\Xi(\omega)G(\omega) \quad . \tag{2.20}$$

Using Eq. 2.20, one can give the relation between $G(\omega)$ and the self energy $\Xi(\omega)$ (Eq. 2.21)

$$\Xi(\omega) = \Xi(\infty) + P(\omega) \quad . \tag{2.21}$$

In Eq. 2.21, $\Xi(\infty)$ is the ω-independent static term and $P(\omega)$ is the ω-dependent dynamic term. The quantity Ξ compared to G is a simpler subject for a diagrammatic perturbation expansion. The Ξ can be approximated up to the third- or fourth-order by the Algebraic diagrammatic construction (ADC) procedure[52, 53]. The ADC is a very general approach and can be applied directly to G or separately to either $G^{-}_{pq}(\omega)$ or $G^{+}_{pq}(\omega)$ parts. This splitting of the Dyson-type secular equation to two separate sets of equations leads to more involved theoretical perturbation expressions for getting the secular matrix elements.

Our main focus is on the $G^{-}_{pq}(\omega)$ part of the spectral representation. Using the ADC approach, the nondiagonal representation for $G^{-}_{pq}(\omega)$ can be given by

$$G^{-}_{pq}(\omega) = f^{\dagger}(\omega - L - D)^{-1} f \quad . \tag{2.22}$$

This form is a result of a complete set of intermediate states included in $G^{-}_{pq}(\omega)$ term[54, 55]. The relation between the intermediate states $|\Psi^{N-1}_{m}\rangle$ and the correlated excited states is given by $\hat{A}_J |\Psi^{N}_{0}\rangle$, where $\hat{A}_J$ represents the excitation operators of the manifold with indices $j, k, l, \ldots$ for the occupied, and $a, b, c, \ldots$ for the unoccupied orbitals.

$$\hat{A}_J = \hat{a}_j, \hat{a}^{\dagger}_{a}\hat{a}_j\hat{a}_k, \hat{a}^{\dagger}_{a}\hat{a}^{\dagger}_{b}\hat{a}_j\hat{a}_k\hat{a}_l, \ldots \quad , \tag{2.23}$$

The $L + D$ part in Eq. 2.22 is the non-diagonal effective interaction matrix and f is the matrix of effective transition amplitudes. Solving the secular equation (Eq. 2.24), one can be convert the nondiagonal representation to the original form given in Eq. 2.17.

$$(L + D)X = X\Omega, \qquad X^{\dagger}X = 1 \tag{2.24}$$

The term X in above equation represents the matrix of eigenvectors, and the spectroscopic amplitudes can be determined using the relation

$$z = X^{\dagger} f \quad . \tag{2.25}$$

Term "f" represents the effective coupling matrix in Eq. 2.22.

Within the ADC method, the approximate scheme is constructed by the perturbation series expansion of $L + D$ and f as:

$$L + D = L + D^{(1)} + D^{(2)} + \dots \quad , \tag{2.26}$$

$$f = f + f^{(1)} + f^{(2)} + \dots \quad .$$

2.5 Charge migration dynamics

To trace the charge transfer within the molecule and the associated electron dynamics, it is convenient to construct and analyze the time-dependent hole density $Q(\overrightarrow{r}, t)$ created by sudden ionization. This process is solely driven by the electron correlation effect and is known as "charge migration dynamics"[22, 56, 57, 58]. The $Q(\overrightarrow{r}, t)$ term describes the density of the hole at position r and time t and by construction is normalized to 1 at all times t (see Eq. 2.27)[59]. The second-quantization representation of the density operator within a one-particle basis is given by Eq. 2.28, where operator $\hat{a}_p^\dagger$ creates an electron in orbital ϕ_p and $\hat{a}_p$ destroys an electron to create a hole in orbital ϕ_p

$$\begin{aligned} Q(\overrightarrow{r}, t) &= \langle \Psi_0 | \hat{\rho}(\overrightarrow{r}, t) | \Psi_0 \rangle - \langle \Phi_i | \hat{\rho}(\overrightarrow{r}, t) | \Phi_i \rangle \quad , \\ &= \rho_0(\overrightarrow{r}) - \rho_i(\overrightarrow{r}, t) \ ; \end{aligned} \tag{2.27}$$

where

$$\rho_i(\overrightarrow{r}, t) = \sum_{p,q} \phi_p^*(\overrightarrow{r}) \phi_q(\overrightarrow{r}) \hat{a}_p^\dagger \hat{a}_q \quad . \tag{2.28}$$

Within this representation, the hole density takes the form as given in Eq. 2.29.

$$Q(\overrightarrow{r}, t) = \sum_{p,q} \phi_p^*(\overrightarrow{r}) \phi_q(\overrightarrow{r}) N_{pq}(t) \quad , \tag{2.29}$$

where $N_{pq}(t)$ represents the hole density matrix. Hole density is given as a difference between the electronic density of the neutral and that of the cation in Eq. 2.27. Here $\hat{\rho}$ is the density operator, $|\Psi_0\rangle$ is the ground state of the neutral, and $|\Phi_i\rangle$ is the initially prepared cationic state. The term $\rho_i(\overrightarrow{r}, t)$ in Eq. 2.27 is a time dependent density operator, since $|\Phi_i\rangle$ is not an eigenstate of the cation. Further details on the construction of the hole density matrix employing the ADC approach can be found in reference [56, 60].

2.6 Vibronic coupling Hamiltonian (VCH)

Before the photo-ionization process, the ground state is assumed to be isolated from the other excitation states. The ground state Hamiltonian in harmonic approximation is given by Eq. 2.30 with unperturbed nuclear kinetic energy (T_N) and potential energy (V_0).

$$H_0 = \underbrace{-\sum_{i=1}^{f} \frac{\omega_i}{2} \frac{\partial^2}{\partial Q_i^2}}_{T_N} + \underbrace{\sum_{i=1}^{f} \frac{\omega_i}{2} Q_i^2}_{V_0} \tag{2.30}$$

The ω_i term in Eq. 2.30 is the harmonic frequency and Q_i are the dimensionless normal coordinates associated with mode i, whereas f is the number of degrees of freedom. After photo-ionization, the Hamiltonian is described by a set of interacting states. Such Hamiltonian is known as the vibronic coupling Hamiltonian (VCH) and is given by Eq. 2.31 using T_N and the vibronic coupling potential energy matrix ($W(Q)$)[61, 62, 63].

$$H = T_N + V_0 + W \tag{2.31}$$

Using a power series up to the second order, and at the equilibrium position of the ground state we construct the diabatic potential energy matrix W. In this matrix the diagonal and off-diagonal elements are given as Eq. 2.32 and Eq. 2.33, respectively.

$$W_{nn}(Q) = IP_n + \sum_i \kappa_i^{(n)} Q_i + \sum_{i,j} \gamma_{i,j}^{(n)} Q_i Q_j + \dots \tag{2.32}$$

$$W_{nn'}(Q) = \sum_i \lambda_i^{(nn')} Q_i + \sum_{i,j} \mu_{i,j}^{(nn')} Q_i Q_j + \dots \tag{2.33}$$

The quantity IP_n in Eq. 2.32 is for the vertical ionization energies, referring at the centre of the Franck-Condon zone, $Q = 0$. The parameters κ^n and γ^n are the linear and quadratic intrastate coupling constants, $\lambda^{nn'}$ is the interstate linear coupling constant for states n and n'. The term $\mu^{(nn')}$ is an off-diagonal coupling constant, which represents the coupling modes that enter bilinearly into the Hamiltonian. The coupling constants can be derived using the least-square fitting. For molecules with symmetry, the sum given in the above equations runs only for the restricted sets of modes. The modes that modulate the energy gap between the two states are called *tuning modes*. These are given by a set of totally symmetric modes, S_1:

$$S_1 : \Gamma_i \supset \Gamma_A \quad . \tag{2.34}$$

Note that the two states will be coupled with the mode if and only if the direct product between the symmetry of mode and the electronic state is symmetric. The set of mode pair that gives the bilinear and quadratic on-diagonal couplings is S_2:

$$S_2 : \Gamma_i \times \Gamma_j \supset \Gamma_A \quad . \tag{2.35}$$

The set representing the linear coupling between the two interacting states is S_3, within which the modes are called *coupling modes*:

$$S_3 : \Gamma_i \times \Gamma_a \times \Gamma_b \supset \Gamma_A \quad . \tag{2.36}$$

Γ_a and Γ_b are the irreducible representations of the two electronic states considered. The off-diagonal coupling modes bilinearly entering the Hamiltonian are given in set S_4:

$$S_4 : \Gamma_i \times \Gamma_j \times \Gamma_a \times \Gamma_b \supset \Gamma_A \quad . \tag{2.37}$$

For two interacting states, the diabatic potential matrix will take the form given as:

$$
\begin{aligned}
H = (T_N + V_0)\mathbf{1}\begin{pmatrix}-IP_1 & 0\\ 0 & IP_2\end{pmatrix} + \sum_{i\in S_1}\begin{pmatrix}\kappa_1 & 0\\ 0 & \kappa_2\end{pmatrix}Q_i + \sum_{(i,j)\in S_2}\begin{pmatrix}\gamma_{i,j}^{(1)} & 0\\ 0 & \gamma_{i,j}^{(2)}\end{pmatrix}Q_iQ_j \\
+\sum_{i\in S_3}\begin{pmatrix}0 & \lambda_i\\ \lambda_i & 0\end{pmatrix}Q_i + \sum_{(i,j)\in S_4}\begin{pmatrix}0 & \mu_{i,j}\\ \mu_{i,j} & 0\end{pmatrix}Q_iQ_j
\end{aligned} \quad . \tag{2.38}
$$

Using the knowledge of the adiabatic potential energy surfaces (PES) (V_i) generated from the quantum chemistry calculations we can determine the parameters for the construction of the VCH. One can determine these by comparing the adiabatic PES calculated by diagonalizing the diabatic model potential, with the PES obtained from quantum chemistry calculations. For example, let's consider that there are two interacting states, the diabatic potential energy matrix (V) is given as

$$\hat{V}(Q) = \begin{pmatrix}a(Q) & c(Q)\\ c(Q) & b(Q)\end{pmatrix} \quad . \tag{2.39}$$

Using Eq. 2.32

$$a(Q) = -IP_1 + \sum_i \kappa_i^1 Q_i + \sum_{i,j}(\gamma_{i,j}^1 - \frac{\omega_i}{2}\delta_{i,j})Q_iQ_j \quad , \tag{2.40}$$

$$b(Q) = IP_2 + \sum_j \kappa_i^2 Q_i + \sum_{i,j}(\gamma_{i,j}^2 - \frac{\omega_i}{2}\delta_{i,j})Q_iQ_j \quad . \tag{2.41}$$

Using Eq. 2.33

$$c(Q) = \sum_i \lambda_i^{1,2} Q_i + \sum_{i,j}\mu_{i,j}^{1,2} Q_iQ_j \quad . \tag{2.42}$$

The general solution to finding the lowest order coupling constants (at $Q = 0$) is:

$$\kappa_i^{(s)} = \frac{\partial V_s}{\partial Q_i} \ |_{Q=0} \quad , \tag{2.43}$$

$$\lambda_i^2 = \frac{1}{8}\frac{\partial^2}{\partial Q_i^2}[V_2(Q) - V_1(Q)]^2 \ |_{Q=0} \ . \tag{2.44}$$

Comparing the eigenvalues of the diabatic potential matrix (see Eq. 2.39) with the V_i from quantum chemistry calculations we use the following relations:

$$\begin{pmatrix}a(Q) & c(Q)\\ c(Q) & b(Q)\end{pmatrix} = \begin{pmatrix}V_1(Q) & 0\\ 0 & V_2(Q)\end{pmatrix} \quad . \tag{2.45}$$

This gives us equation (Eq. 2.46), which can be solved using some algebraic methods.

$$(V_1(Q) - V_2(Q))^2 = (a(Q) - b(Q))^2 + 4c(Q)^2 \tag{2.46}$$

Note that although it is difficult to perform the adiabatic to diabatic transformation, the diabatic ($V_{dia} = H - T_N\mathbf{1}$) to adiabatic ($V_{adia}$) transformation is easy using the unitary transformation matrix U (in practice it can be expensive):

$$U^{\dagger} V_{dia} U = V_{adia} \quad . \tag{2.47}$$

The fitting is obtained using the weighted least-square fitting procedure. The least-square fitting function is given by:

$$L = L(\boldsymbol{\kappa}, \boldsymbol{\lambda}, \boldsymbol{\gamma}, \boldsymbol{\mu}) \quad , \tag{2.48}$$

$$\begin{aligned} L = &\sum_{f=1}^{M_1} c_1^{(f)} [V_1^{mod}(IP_1, IP_2, \boldsymbol{\kappa}, \boldsymbol{\lambda}, \boldsymbol{\gamma}, \boldsymbol{\mu}; \mathbf{Q}_f) - E_1(\mathbf{Q}_f)]^2 \\ &+ \sum_{f=1}^{M_2} c_2^{(f)} [V_2^{mod}(IP_1, IP_2, \boldsymbol{\kappa}, \boldsymbol{\lambda}, \boldsymbol{\gamma}, \boldsymbol{\mu}; \mathbf{Q}_f) - E_2(\mathbf{Q}_f)]^2 \end{aligned} \quad . \tag{2.49}$$

The coupling constants are given as $\boldsymbol{\kappa}, \boldsymbol{\lambda}, \boldsymbol{\gamma}, \boldsymbol{\mu}$ and $V_{(1,2)}^{mod}$ represents the adiabatic surfaces that are obtained after diagonalization of the potential part of the VCH given in Eq. 2.38. M_1 and M_2 represents the number of points calculated on the PES. $E_{(1,2)}^{(f)}$ are the calculated energy values for Q_f points on the PES in Q-space. The term $c_{(1,2)}^{(f)}$ is a positive weight function and plays an important role in amplifying the importance of the region where the PES density is high and damp in the region of low density. One way of expressing this weight function is given in Eq. 2.50 with positive constants α and β.

$$c_{1,2}^{(f)} = \begin{cases} exp[\alpha(IP_{1,2} - E_{1,2}^{(f)})] : & E_{1,2}^{(f)} \leq IP_{1,2} \\ exp[\beta(IP_{1,2} - E_{1,2}^{(f)})] : & E_{1,2}^{(f)} > IP_{1,2} \end{cases} \tag{2.50}$$

If the quadratic terms (γ and μ) in Eq. 2.38 are set to zero then one arrives at the linear vibronic coupling (LVC) model.

2.7 The multiconfiguration time-dependent Hartree (MCTDH) method

MCTDH is a every efficient method to solve TDSE[64, 65, 66] using a multistate ansatz, where the wave function on each state $\Phi^{(a)}$ is expanded as a linear combination of Hartree products:

$$\Psi(q_1, \ldots, q_p, t) = \sum_a \underbrace{\sum_J A_J^{(a)} \Phi_J^a \left| a \right\rangle}_{\Psi^{(a)}} \quad , \tag{2.51}$$

$$\Psi(q_1, \ldots, q_p, t) = \sum_{a=1}^{s} \sum_{j_1=1}^{n_1^{(a)}} \cdots \sum_{j_p=1}^{n_p^{(a)}} A_{j_1 \ldots j_p}^{(a)}(t) \times \prod_{\kappa=1}^{p} \phi_{j_\kappa}^{(a,\kappa)}(q_\kappa, t) \left| a \right\rangle \quad . \tag{2.52}$$

The number of electronic states and MCTDH particles are given by variables 's' and 'p'. A discrete set of electronic states $|a\rangle$ are labelled by indices $\{a\}$. Wave packet ($\Psi^{(a)}$) associated with each electronic state is given with a distinct set (J=$j_1 \ldots j_p$) of the single-particle function (SPF) ($\phi_{j_\kappa}^{a,\kappa}$). Hence, for each relevant state, the summation over all the possible index combinations is given by $\sum_J$. The computational costs for a multidimensional system can be significantly reduced when particle coordinates can be grouped to form a set $[q_k = Q_i, Q_j, \dots]$ with κ degrees of freedom. Such grouping is done for systems where the set contains more than five coordinates. This makes SPF a multidimensional function of 'p' number of particles and 'f' sets of system coordinates, where $p < f$. In Eq. 2.52 if we set the number of degrees of freedom or MCTDH particles to $n_1 = n_p = 1$, then we obtain the time dependent Hartree method (TDH), which is the limiting case of MCTDH.

2.8 Laser-induced alignment and orientation: the TDSE method

The calculation of the laser-induced alignment and orientation dynamics for a molecular system can be calculated by solving the time-dependent Schrödinger equation (TDSE) [67, 68]. One needs to solve the TDSE of the form

$$\mathrm{i}\hbar\partial_t|\Phi(t)\rangle = \hat{H}(t)|\Phi(t)\rangle = (\hat{H}_0 + \hat{H}_{\mathrm{ext}}(t))|\Phi(t)\rangle \quad , \tag{2.53}$$

where the $\hat{H}_0$ part is the molecular field-free Hamiltonian. This Hamiltonian is constructed under the rigid rotor approximation, i.e., no rotational-vibrational coupling terms are considered. The TDSE given in Eq. 2.53 is solved in two parts. First the solution for the trivial field-free Hamiltonian is given by

$$\hat{H}\,|\Phi_m\rangle = E_m\,|\Phi_m\rangle \quad . \tag{2.54}$$

Note that this solution is non-trivial when one considers an asymmetric top molecule. The second step involves the $\hat{H}_{\mathrm{ext}}(t)$ term in Eq. 2.53. This is the time dependent part of the Hamiltonian, where the laser-matter interactions are taken into consideration. This external interaction Hamiltonian is expanded as

$$\hat{H}_{\mathrm{ext}}(t) = \underbrace{-\mu\epsilon(t)}_{\hat{V}_{\mathrm{dip.}}(t)} - \underbrace{\frac{1}{2}\epsilon(t)(\alpha\epsilon(t))}_{\hat{V}_{\mathrm{pol.}}(t)} - \underbrace{\frac{1}{6}\epsilon(t)(\epsilon(t)\beta\epsilon(t))}_{\hat{V}_{\mathrm{hyp.}}(t)} \quad . \tag{2.55}$$

In Eq. 2.55, the three terms represent the interaction of the laser field with the permanent electric dipole moment (μ), the polarizability tensor (α) and the hyperpolarizability tensor (β). When considering the interaction with a single optical laser pulse, the first and third order terms in Eq. 2.55 can be neglected. The first term can be neglected for an optical pulse, as the period of an oscillating optical pulse is shorter in comparison to the characteristic rotational period of the molecule. Hence, the interaction with the external field can be cycle-averaged by neglecting the first term[69] and rewriting this equation yields Eq. 2.56. However, for the THz pulse this term is dominant and needs to be retained. The third term includes the interaction of molecular hyperpolarizability with the laser field, which is important when dealing with overlapping multiple pulses, such as the $(\omega, 2\omega)$ setup[70].

$$\hat{H}_{\mathrm{ext}}(t) = -\frac{1}{4}\epsilon(t)(\alpha\epsilon(t)) \tag{2.56}$$

The description of the external electric laser field is given as a linearly polarized pulse along the Z-axis in a laboratory-fixed (LF) frame. This laser pulse has a Gaussian envelope with ω as its central frequency. The z component of this laser field is given by

$$\epsilon_z(t) = \epsilon_0(t)\cos(\omega t + \xi) \quad . \tag{2.57}$$

The envelope of the laser field is given by ϵ_0(t), while the carrier frequency and carrier envelope phase (CEP) are denoted by ω and ξ, respectively.

Now we are in the position to discuss the solution of Eq. 2.53. In the second part of the solution, the rotational wavepacket is expanded in terms of the rotational eigenstates $|\Phi_m(t)\rangle$:

$$|\Phi(t)\rangle = \sum_m C_m(t) |\Phi_m\rangle \quad . \tag{2.58}$$

Using Eq. 2.54 and Eq. 2.55 we get

$$H_{mm'} = \langle\Phi_m| \hat{H} |\Phi_{m'}\rangle \quad , \tag{2.59}$$

$$= E_m\delta_{mm'} - \langle\Phi_m| \mu\epsilon(t) |\Phi_{m'}\rangle - \frac{1}{2} \langle\Phi_m| \epsilon(t)(\alpha\epsilon(t)) |\Phi'_m\rangle - \frac{1}{6} \langle\Phi_m| \epsilon(t)(\epsilon(t)\beta\epsilon(t)) |\Phi_{m'}\rangle \quad ,$$

whereas for Eq. 2.56 this will take the form

$$H_{mm'} = E_m\delta_{mm'} - \frac{1}{4} \langle\Phi_m| \epsilon(t)(\alpha\epsilon(t)) |\Phi_{m'}\rangle \quad . \tag{2.60}$$

We solve the TDSE using the LIMAO package, which calculates the temporal evolution of physical quantities at once for different times. These quantities are calculated by getting the expectation values using the rotational wavepacket[67, 68]. For computing the matrix elements in Eq. 2.59, an efficient approach is to convert the Cartesian representation for rotational parameter values calculated with the ab-initio method to the spherical-basis representation using the transformation formulae[71, 72] $\mu^{(1,0)} = \mu_3$, $\mu^{(1,\pm1)} = \frac{1}{\sqrt{2}}(\mp\mu_1 - i\mu_2)$, $\alpha^{(0,0)} = \frac{-1}{\sqrt{3}}(\alpha_{11} + \alpha_{22} + \alpha_{33}) = \frac{-1}{\sqrt{3}}Tr[\alpha]$, $\alpha^{(2,\pm2)} = \frac{1}{2}[\alpha_{11} - \alpha_{22} \pm i(\alpha_{12} + \alpha_{21}]$, $\alpha^{(2,\pm1)} = \frac{1}{2}[\mp(\alpha_{13} + \alpha_{31}) - i(\alpha_{23} + \alpha_{32})]$, and $\alpha^{(2,0)} = \frac{1}{\sqrt{6}}[2\alpha_{33} - \alpha_{22} - \alpha_{11}]$.

LIMAO allows us to set the rotational temperature and calculate the populations in the respective rotational eigenstates assuming the Boltzmann distribution. The population at the i^{th} rotational state is given by

$$P_i = \frac{e^{-\frac{E_i}{kT}}}{\sum_l e^{-\frac{E_l}{kT}}} \quad , \tag{2.61}$$

where k is the Boltzmann constant and E_i is the energy of the i^{th} rotational state. The temporal evolution of the expectation value of a physical quantity $\hat{A}$ is then expressed as

$$\langle\hat{A}\rangle(t) = \frac{1}{Q(T)} \sum_i \langle\Phi^{(i)}(t)| \hat{A} |\Phi^{(i)}(t)\rangle g_i e^{-\frac{E_i}{kT}} \tag{2.62}$$

and

$$Q(T) = \sum_i g_i e^{-\frac{E_i}{kT}} \quad , \tag{2.63}$$

where $\Phi^{(i)}$(t) is the time-dependent rotational wave packet when the initial condition is set to be the i^{th} rotational eigenstate, thus

$$\langle\Phi^{(i)}(t)| \hat{A} |\Phi^{(i)}(t)\rangle = \sum_{n,m} C_m^{(i)*}(t) C_m^{(i)}(t) \langle\Phi_m| \hat{A} |\Phi_m\rangle \quad , \tag{2.64}$$

with $C_m^{(i)}(t=0)=\delta_{im}$. $Q(T)$ is the rotational partition function and g_i stands for the nuclear spin statistical weight of the i^{th} rotational eigenstate. Nuclear spin statistical weights for the irreducible representation of D_∞[67, 68] are calculated to be A_1 (Σ^+) = A_2 (Σ^-) = 2, E_1 (Π) = E_2 (Δ) = 1 and E_3 (Φ) = 2 for the CH_3F molecule.
The time-dependent degree of alignment of a symmetric top molecule can be computed as the expectation values,

$$\left\langle \cos^2(\theta) \right\rangle (t) = \langle \Phi(t) | \cos^2(\theta) | \Phi(t) \rangle \tag{2.65}$$

The angle between the lab-fixed z-axis and the molecular symmetry axis is given by θ.

Chapter 3

Insights Into Intramolecular Charge Transfer: An Ab Initio Approach

Charge transfer and charge migration play a fundamental role in many areas of material science like photovoltaics, photoemission, photocatalysis, sensor applications etc. Recent experimental advancements to resolve even the faster temporal events ensure additional impetus. Understanding the spatial distribution of charge density in the ground, excited and cationic states is a prerequisite in predicting the photo-induced charge transfer in large π-conjugated systems. Large push-pull dye molecules are often integrated in organic or hybrid photovoltaic devices, light emitting diodes and photo-chemical cells. To model molecules with high efficiency for the application in such devices, it is essential that we understand the photo-induced intramolecular charge transfer (ICT) from donor to acceptor in these dye molecules. In this chapter I present our DFT results on the intramolecular charge transfer process in an experimentally synthesized, stable organic donor-acceptor (*D–A*) dye, ADEKA1. Furthermore, I analyze the electronic properties and structural parameters of the dye molecule in their ground, excited and cationic states; to interpret the extend of charge transfer. These states were chosen as they are present and crucial for the charge transfer and dye regeneration processes. Through the commonly used correlation between structural modification and charge redistribution in different groups of the molecule, the extent of π-conjugation and the spatial rearrangement of electron density localization along the molecular skeleton can be highlighted. Note that all the results presented and discussed in this chapter are from our own publication Ref.[73] and are reprinted with copyright permission (2022) from the American Chemical Society.

3.1 Motivation

The first Dye Sensitized Solar Cell (DSSC) was developed and reported by O'Regan and M. Grätzel in 1991, which sparked a rapid development in organic solar cell devices[74, 75]. The main underlying motivation was the potential of producing cost-efficient materials[76], the flexibility of devices[77], as well as the stability and performance under diffuse light conditions[78]. The operation of the organic solar cell device is triggered by the photo-excitation of the dye molecule (from Dye → Dye*/Dye$^+$ in *ns*). This excited electron is transferred to the conduction band of the semiconductor material with a favourable band offset in a few *ps*. This leaves the dye molecules

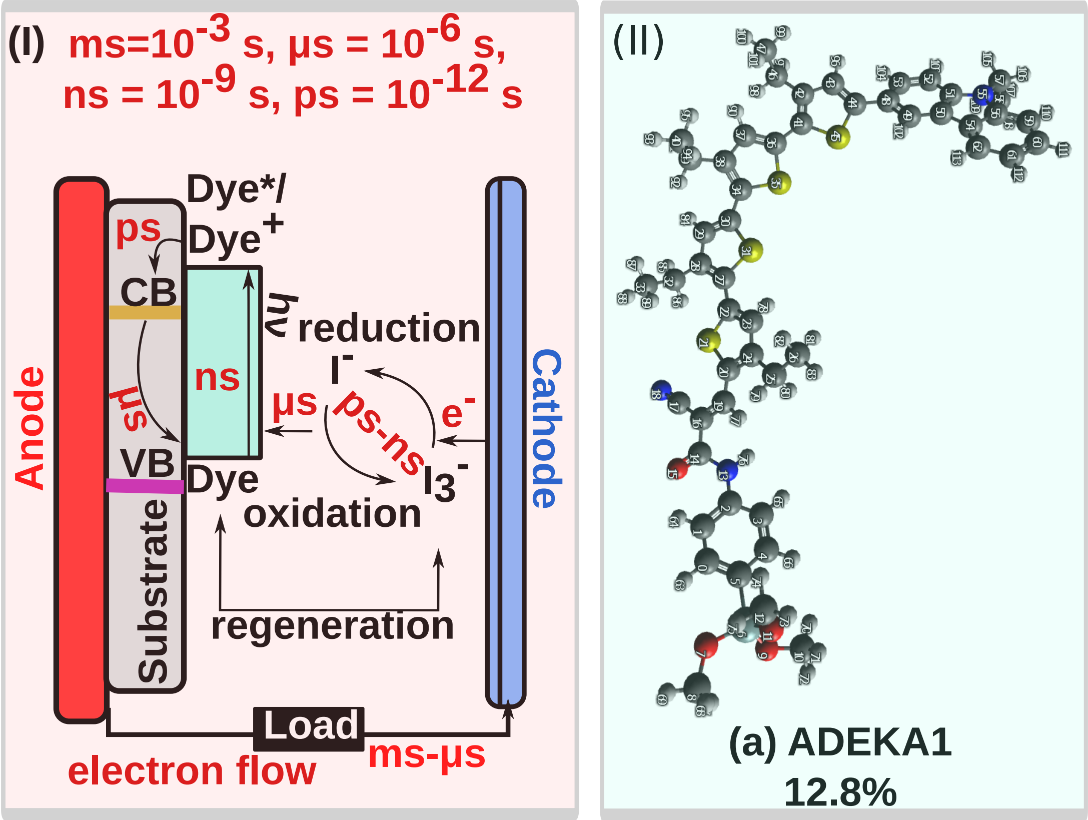

Figure 3.1: *(I) Schematics of DSSC with electron transfer processes and the associated time scales involved. (II) Structure and the experimentally reported power conversion efficiency (PCE) of dye (a) ADEKA1. Atom colours: C (dark grey), S (golden), O (red), N (blue), H (light grey).*

in its cationic (Dye^+) state[79]. The two states of the dye, excited and oxidized or cationic states are important and hence studied in this chapter. Coming back to the operation of DSSC, the photoelectrons from the anode move in 10^{-8} to 10^{-1} s through an external circuit towards the cathode[80]. The dye in its cationic state is regenerated when it receives electrons from any suitable redox mediator (for example I^-/I^{-3}) in (μs). In the *ps-ns* timescale, the oxidation of the medium takes place and the oxidized redox mediators (I^{-3}) diffuse to the counter electrode. This is where the electrons coming through the counter electrode recombine with the oxidized redox medium and regenerate it. Hence, the device components, the dye layer and the electrolyte solution regain their original state and are ready to repeat the cycle. The working schematics of the above described typical DSSC with the various processes and corresponding time scales involved in the charge transfer are given in Fig. 3.1(I). It is understood that the performance of such devices relies on various processes. However, here I focused my discussion on the highly sensitive structures, charge transfer and performance of the dye molecules[81].

Push-pull type dyes used in DSSC devices usually have donor-acceptor (D–A), donor–π-spacer–acceptor (D–π–A)[82], D–π–π–A, D–A′–π–A or D–D′–π–A structure types[83, 84, 85]. The electron donating group with highly positive mesomeric effects, synthetic availability and modularity

Dyes	fused D	fused π	fused A	λ_e	λ_h	λ	$\lambda' = \lvert\lambda_e - \lambda_h\rvert$
ADEKA1	yes	NA	no	0.4507	0.4441	0.8949	0.0066

Table 3.1: *Presence of different types of fused groups such as D, π-spacer and A group in dye, calculated values of the reorganization energy for electron (λ_e), hole (λ_h), total (λ) and difference in reorganization energy ($\lambda' = \lambda_e - \lambda_h$) in eV, for ADEKA1 ("NA" means not applicable)*

includes aromatic amines such as triphenyl amine[86], carbazole[87] and triazatruxene[88]. The linking group between donating and accepting moiety is the π-spacer group, which has to have an electron affinity greater than the donor and lower than the acceptor group[89]. Hence, during photo-conversion and transfer, the electron density of the dye molecule is rearranged and localized around the highly electronegative groups such as the π-spacer and acceptor groups[90], which facilitates the charge transfer to the semiconductor layer.

In order to design a new system with high photo-conversion efficiency, we must understand its physicochemical and photo-chemical properties. To calculate the charge transfer in the large molecules I adopted the ab-initio density functional theory (DFT) and the time-dependent density functional theory (TDDFT), which are known to provide good agreement with the experimentally reported structural and spectral properties[91, 92, 93, 94]. The absorption and fluorescence spectra calculated using the DFT methodology can help us understand the photo-induced intramolecular charge transfer (ICT) process[95]. In a large molecular system, one of the important aspects for ICT is the flow of electrons through the π-conjugation. This delocalization of charge will change the structure of the entire system. Computing the real-time change in the structure of the system after photo-excitation is not a trivial problem. However, its reverse, analyzing the extent of π-conjugation through the modification in the structural parameters after photo-excited is trivial. Hence, in this chapter I present how we can predict the extent of the π-conjugation in the system by calculating the difference in the structure of the excited and ionized systems with respect to the ground state. This study will help in the preliminary analysis of the system and how efficient it will be to transfer the charge from the donor to the acceptor group within the system. [96, 97].

ICT can be observed through the difference in structural properties, via twisting certain groups in the dye molecule, and/or prominent changes in structural parameters such as bond length, bond angle or dihedral angle[93, 94]. Many recent studies have reported the use of fused molecules as the donor, π-spacer or acceptor groups to design organic dyes. These systems have fused rings, which are known to increase the performance of the dye[98, 99, 100]. If the dye molecule has fully fused groups, it will have a planar backbone, which will mainly show the twisting of this group after ICT. However, a non-fused group manifests more structural distortions. Using the DFT method, in this chapter I analyze the structural changes and the resulting ICT after the photo-excitation in the ADEKA1 dye molecule (Dye $\rightarrow$ Dye*/Dye$^+$). In this chapter I presented the results for only the ADEKA1 dye, however in our published work [T1][73] I used the same approach to analyze five more dyes.

3.2 Computational method

A detailed description of the theory used for the calculation of the results presented in this chapter is given in Chapter 2. I briefly summarize the steps I used to determine the ICT for the ADEKA1 dye is given in the next section. I begin by optimizing the neutral ground state geometry. This structure is used to calculate the UV-Vis absorption spectra, the transition states, and the transition electron density with the TDDFT method. Then I will relax the molecule in the excited state with low energy and high transition probability. I will use the ground state structure to ionize the system by removing an electron (Dye$^+$, cationic state) and add an electron (Dye$^-$, anionic state) to relax the geometry again. Using the final energies of the ground, cationic and anionic dye molecule I calculated the reorganization energy ($\lambda_{e/h}$). The difference in the structural parameters, the bond length, bond angle and dihedral angles are then calculated for the dye in the excited and the cationic states with respect to the ground state.

All the results presented in this chapter were calculated using the DFT and TDDFT methods implemented in the ORCA 4.0 [101, 102] quantum chemistry package. The molecular parameters for the ground, excited and ionic states, as well as the excited state properties for the ADEKA1 dye were calculated using the PBE0/def2-TZVP method [103, 104, 105]. The computational costs for these calculations were reduced by replacing the large hexyl groups in ADEKA1 with ethyl groups. To simulate the excited state properties with real experimental conditions, I included the solvent effect using the conductor-like polarizable continuum model (CPCM) [106]. The energy gap was calculated by taking the difference between the highest occupied molecular orbital (HOMO) and lowest unoccupied molecular orbital (LUMO) levels ($E_g = E_{LUMO} - E_{HOMO}$). The singlet excitation state lifetime (τ) was calculated using the excitation energy (*E*) and oscillator strength (*f*), $\tau = \frac{1.499}{f*E^2}$ [107]. The term τ estimates the lifetime of an excited electron and helps in determining the injection time from the dye to the semiconductor substrate.

Marcus [108, 109, 110] developed the semi-classical theory for the charge transfer rate equation, whereas the quantum mechanical treatment was proposed by Jorther et. al. [111, 112, 113]. In the non-adiabatic regime, the electron transfer is analogous to an optical transition between electronic states within the Franck-condon approximation [114]. The probability of charge transfer from a donor to an acceptor is determined by the rate of charge transfer. Assuming a maximum transfer rate, Gibbs free energy is considered approximately equal to the reorganization energy ($\lambda = \lambda_e + \lambda_h$). In λ_i = ($E_0^{\pm}$ - $E_{\pm}$) + ($E_{\pm}^0$ - E_0), the energies of the neutral and cation or anion species are given by E_0 and $E_{\pm}$ respectively, whereas the energies of the cation and neutral species with the geometries of the neutral and cation or anion species are $E_{\pm}^0$ and $E_0^{\pm}$, respectively.

3.3 Results and discussions

I relaxed the structure of the ADEKA1 dye in the ground state and calculated the band gap of 2.73 *eV*, which is a bit overestimated compared to the experimental band gap of 1.85 *eV*. This value can be improved using a better functional group and basis set. However, since the size of ADEKA1 is computationally demanding, our interests lie in the qualitative rather than the quantitative studies. The energy of the HOMO (-5.41 *eV*) for ADEKA1 is well below the redox potential for I^-/I^{-3} electrolyte which is -4.8 *eV*[115]. The energy of LUMO is -2.68 *eV*, which is above the position of the conduction band edge in a commonly used TiO_2 semiconductor (-4.0 *eV*)[116]. This ensures that the energies of the ADEKA1 dye are in the regime that ensures charge transfer to the semiconductor, and its regeneration through an electron given by the electrolyte.

To calculate the photo-absorption spectra I used the combination of the TDDFT and CPCM methods. The solvent description used (toluene) is the same as the one reported in the experimental studies[117, 118]. The absorption peak positions, and the corresponding molecular orbital contributions are given in Table 3.2. The absorption peak with lowest energy is due to the HOMO→ LUMO transition. In order to study this further, I have used the optimized the structure of the

λ in *nm* (Excited state)	Molecular orbital contribution	OS	$\tau(ns)$
643.5 (1)	$HOMO \rightarrow LUMO(97\%)$	0.75	8.27
450.2 (2)	$HOMO-1 \rightarrow LUMO(84.39\%)$ $HOMO \rightarrow LUMO+1(11.10\%)$	0.91	3.33
419 (3)	$HOMO-2 \rightarrow LUMO(47.79\%)$ $HOMO \rightarrow LUMO+2(36.37\%)$	0.28	9.41
386.5 (4)	$HOMO \rightarrow LUMO+1(37.36\%)$ $HOMO-4 \rightarrow LUMO(29.42\%)$ $HOMO-2 \rightarrow LUMO(26.41\%)$	0.35	6.39
373.7 (6)	$HOMO-3 \rightarrow LUMO(44.57\%)$ $HOMO-4 \rightarrow LUMO(38.13\%)$	0.12	17.4

Table 3.2: *Calculated values for the absorption peaks (λ, nm), molecular orbital transitions, oscillator strength (OS) and excitation lifetime τ (ns) for ADEKA1.*

ADEKA1 dye in its first strong excited state, I will call this “excited state” in this chapter. The 2.06 *D* difference in the dipole moment between the relaxed structure in the ground and excited states suggests a possible prominent modification of charge densities. The increase in dipole moment can be attributed to the prominent separation of the two charge density clouds (hole and electron) on the donor and acceptor sites. This can be confirmed with further analysis of the difference in structural parameters[119, 120] of the excited state molecule with respect to the ground state. Another commonly studied parameter is the charge reorganization energies (λ_i with $i = e$ for electron, h for hole). The term λ_i helps in understanding the efficiency of the material for transferring respective charges ($i = e, h$) across the molecule. After calculating λ_i, a smaller difference between λ_e and λ_h implies that the dye can transport both charged particles with similar ease in addition to choosing the charge transport material[121]. The ADEKA1 dye (see Table 3.1) shows a small value for λ'. Hence, ADEKA1 is efficient in both electron and hole transfer.

The change in bond length for the excited and cationic states with respect to the ground state is given in Fig. 3.2. The bond length between two atoms (Xi and Xj) is designated as B(Xi, Xj); similarly, the bond angle between three atoms can be described as A(Xi, Xj, Xl), and the dihedral angles for four atoms as D(Xi, Xj, Xl, Xk). For the ADEKA1 dye, the atomic indices for atoms are in the following order (except for hydrogen): For the donor group, the atoms are indexed from 48 to 62, and for the acceptor group from 0 to 47. The extent of π-conjugation and charge transfer can be clearly observed through the variation in bond lengths for: the donor group B(C48,C44) and B(C50,C49), and the acceptor group B(C44,C43), B(C36,S35), B(C22,S21), B(C36,S35), B(S31,C30) and B(Si6,C5). In addition to the bond lengths I have tabulated the prominent change in bond angles and dihedral angles in the acceptor group in Table 3.3. From Fig. 3.2 and Fig. 3.3 I observe the alteration of the structural parameters over the entire system. This explains the high level of π-conjugation in both the excited and cationic states. On measuring the distance between the donor group (N atom) and the acceptor group (Si atom), I noticed an increase in distance for the excited state by 0.665 Å, and for the cationic state by 0.742 Å. In Fig. 3.3 I could see a prominent change in dihedral angle between the donor and the acceptor (first thiophene), and between the last thiophene in the acceptor and the phenyl-silyl-anchor. Major variations observed are at the atomic sites of donor which are close of the oligothiophenes in acceptor group such as, (B(C48,C44), B(C50,C49), D(C49,C48,C44,C43), D(C49,C48,C44,S45)). The minor variations in bond length or bond angles within the donor group show that the fused

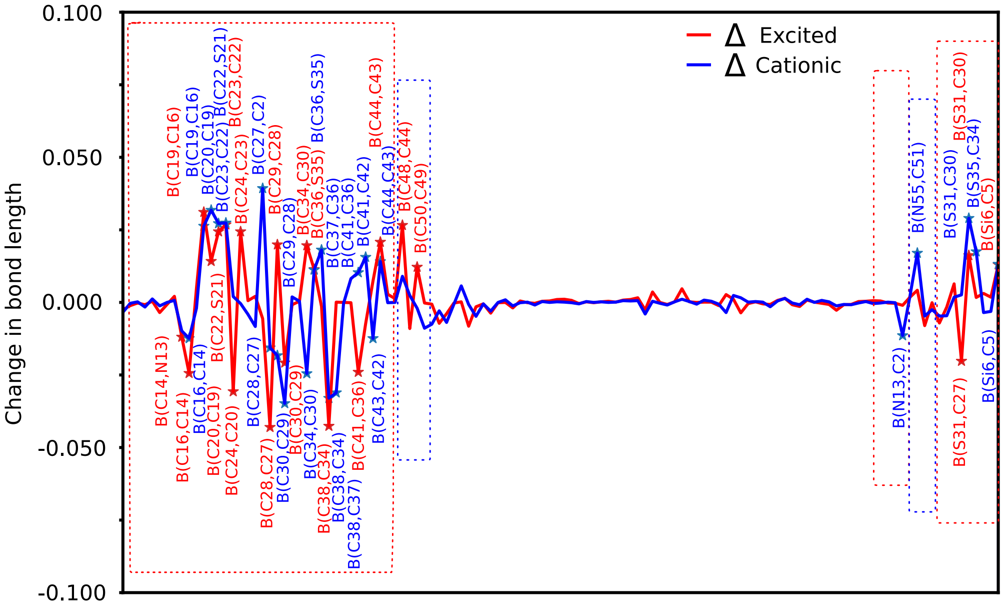

Figure 3.2: *Difference between the excited (red) and cationic state (blue) bond lengths, with respect to the ground state. The values Δ >0.01 Å are marked with "*". The boxes highlighted in red and blue indicate changes for the acceptor group and the donor groups, respectively.*

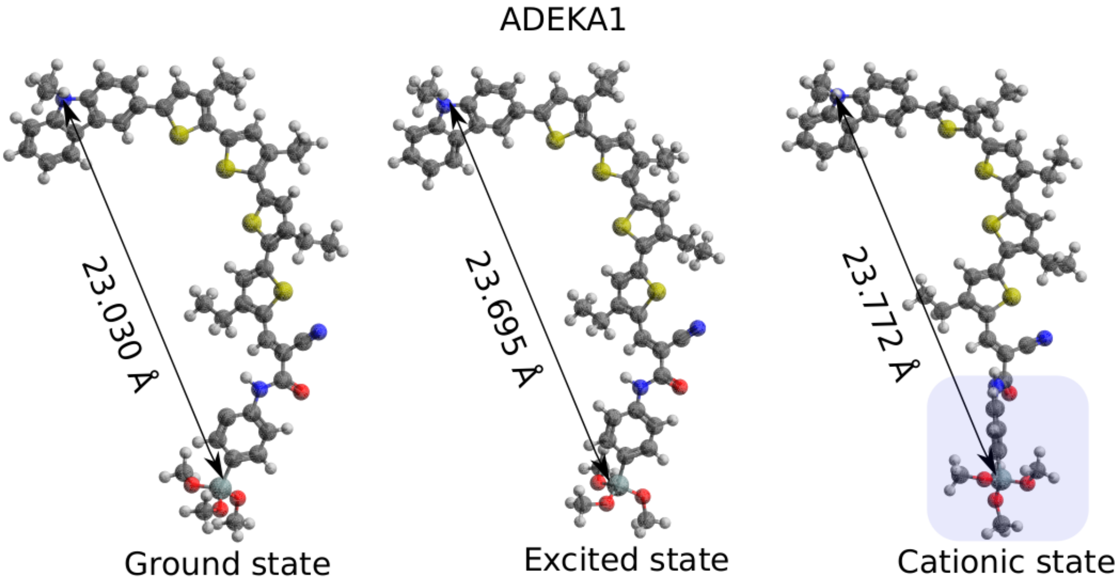
ADEKA1
23.030 Å
23.695 Å
23.772 Å
Ground state
Excited state
Cationic state

Figure 3.3: *The distance measured between the donor and acceptor group of ADEKA1 in three states: ground state, excited state and cationic state. The blue highlighted boxes show the variation in the planar acceptor anchoring site, while the red boxes show the variations for the donor group.*

Definition	ΔE	Definition	ΔC
A(C14,C16,C17)	3.19	A(C14,C16,C17)	2.76
A(C14,C16,C19)	-3.12	A(C14,C16,C19)	-3.08
A(C37,C36,C41)	-6.09	A(C34,C38,C39)	-3.34
A(C37,C38,C39)	-2.96	AI can see that t(C36,C41,S45)	3.12
A(C38,C39,C40)	-2.67	A(C37,C36,C41)	-4
A(S35,C36,C41)	-6.2	A(C37,C38,C39)	-3.12
		A(Si6,O7,C8)	-2.74
D(C8,O7,Si6,O9)	20.34	D(C12,O11,Si6,C5)	-25.41
D(C8,O7,Si6,O11)	22.14	D(C12,O11,Si6,O7)	24.85
D(C17,C16,C14,N13)	-20.39	D(C38,C34,C30,C29)	124.34
D(C26,C25,C24,C20)	92.22	D(C38,C34,C30,S31)	59.92
D(C26,C25,C24,C23)	-86.23	D(C40,C39,C38,C34)	48.74
D(C38,C34,C30,C29)	123.29	D(C40,C39,C38,C37)	-21.99
D(C40,C39,C38,C34)	50.45	D(C49,C48,C44,C43)	-93.96
D(C42,C41,C36,C37)	-12.28	D(C49,C48,C44,S45)	-62.86
		D(H79,C25,C24,C20)	-63.83
D(H68,C8,O7,Si6)	20.54	D(H91,C39,C38,C34)	36.82
D(H74,C12,O11,Si6)	-22.71	D(H91,C39,C38,C37)	-44.39
D(H75,C12,O11,Si6)	25.86	D(H92,C39,C38,C34)	-33.69
D(H79,C25,C24,C23)	97.68	D(H92,C39,C38,C37)	-38.65
D(H80,C25,C24,C20)	22.72	D(O7,Si6,C5,C0)	42.56
D(H91,C39,C38,C34)	-50.73	D(O9,Si6,C5,C0)	23.07
D(H92,C39,C38,C34)	24.38	D(O9,Si6,C5,C4)	119.53
D(H92,C39,C38,C37)	-29.29	D(O11,Si6,C5,C0)	-25.23
D(O7,Si6,C5,C4)	-30.69	D(S35,C34,C30,C29)	-12.19
D(O11,Si6,C5,C4)	-42.21	D(S35,C34,C30,S31)	29.65

Table 3.3: *Changes in the structural parameters of ADEKA1 for bond angle (A,°) and dihedral angle (D,°) in the excited state (ΔE) and the cationic state (ΔC) with respect to the ground state.*

rings are structurally stable after excitation and ionization. On the contrary, the oligothiophenes, which are separated and not fused, show major variation. This reflects the transfer of charge from one end of the dye to another. Possible transfer of charge from the dye to the semiconductor layer can be ensured through the twist of the phenyl-silyl-anchor in the cationic state (highlighted box in Fig. 3.3).[122, 123, 124]

3.4 Summary and conclusions

In summary, the geometry for ADEKA1 in the ground, excited and cationic states was optimized. The ground state geometry was used to calculate the UV-Vis spectra with the TDDFT and CPCM methods. The latter simulated the solvent effect as specified in the experimental report[117]. The transition charge density, reorganization energy, difference in dipole moment were computed to highlight that ADEKA1 shows effective charge separation and transfer from the donor to the acceptor group. The difference in the structural parameters computed for the excited and cationic states with respect to the neutral ground state guides us in establishing a more general correspondence between the structural properties and the mapping of charge transfer. The high variations in the structural parameter differences calculated and the twisting of groups in ADEKA1 support the experimentally observed efficiency of the dye in the photo-conversion process. This method was used on five more dye molecules and the analysis of those molecules can be read in the article published by K. Chordiya et al.[73]

Currently the photo-conversion efficiency of the DSSC device is $<15\%$. To design the molecular system, we need a deeper understanding of the charge migration dynamics along with the charge transfer within the different groups. In this thesis I will address charge migration in different molecular systems that can be used or modified to design efficient charge transfer molecules.

Chapter 4

Attosecond to Femtosecond Pure Charge Migration Dynamics

The intramolecular charge transfer presented and discussed using the structural variations in Chapter 3 shows that charge transfer within a large molecule depends on charge migration within the subunits of the molecule. The long-range of Coulomb interaction is responsible for the correlated motion of the charges in a molecule. Hence, if the correlation between the electrons is strong, chances are that any perturbation applied to a single electron will be experienced by the entire system. In the present study I use the sudden ionization approach to perturb the system and initiate the charge migration dynamics (CMD). Sudden ionization means that the electron is removed suddenly, creating a hole so that the time for complete ionization is extremely short and only the effects after the ionization are experienced by the system. As the hole is created, the electrons surrounding the hole require about 50 attoseconds (*as*) to realize and to start filling the vacancy[22, 26, 125]. I begin by investigating this response time of the electrons and then move on to the femtosecond CMD in closed systems. The *ab initio* multielectron wavepacket propagation method is used to show that the characteristics of charge migration (charge moving from one molecular site to another) is sensitive to factors such as: (i) the symmetry of the perturbed orbital, and (ii) the tautomeric form. A few questions discussed in this and the next two chapters are: (i) How fast can a charge density cloud respond to sudden ionization? (ii) How far and in how much time charge migrates from one site to another? (iii) How do small variations in molecular structures affect the overall CMD? (iv) How long does the pure charge migration last and when does the coupling with nuclear dynamics set in? To address the first question and the foundation for addressing the rest of the questions in the following chapters can be found here. In the next chapter, we study the effect of multiple structural variations in a hetero-cyclic system (closed molecule with different atoms in the ring) on ultrafast charge migration dynamics.

For this chapter we selected a prototype system, Uracil (**U**). **U** is one of the RNA nucleobases and can be found in several tautomeric forms[126]. **U** contains a carboxyl group, which leads to two most common tautomers: keto and enol. Y. Tsuchiya et al. reported that amongst these tautomers, the keto form is more stable until $\sim$ 200°C [127]. In 2018, Colasurdo et al. reported the coexistence of keto-enol tautomers and the interconversion between the two forms before the ionization of **U** (see Fig 1b)[128]. In 2015, K. Saiagh et al. reported that photo-tautomerism between these two structures is possible with > 200 *nm* photons [129]. Hence we choose two important tautomeric forms, 'keto-**U**' and 'enol-**U**' in the gas phase. The structure of these two tautomers can be seen in Fig.4.1(a,b) with an energy difference of 0.48 *eV*. Typically, **U** is found in its keto-**U** form, with two carboxyl groups. In keto-**U**, the tautomeric hydrogen (H9) is bonded with nitrogen (N1) between the two carboxyl groups, and the tautomeric hydrogen (H9) is bonded with oxygen (O7) in enol-**U**. The tautomeric hydrogen is referred to as (Ht) throughout this chapter. The structure of the two **U** tautomers is in C_s symmetry. Hence, the symmetric (a′) and anti-symmetric (a″) orbitals will be studied here. The detailed theory and steps used for calculating the following results are given in Chapter 2. Note that all the results presented and discussed in this chapter are from our own publication, Ref.[130] with permission from K. Chordiya et. al., Physical review A, 105, 062808, 2022, Copyright © (2022) by the American Physical Society and Ref. [131], in press with permission from the Royal Society of Chemistry, respectively.

4.1 Methods

The theory used for the calculation of the results presented in this and the next chapter is described in detail in Chapter 2. The geometry of the molecular systems used in this study were optimized with the density functional theory[132, 133, 134] and PBE0/def2-TZVP[135] basis set as implemented in the ORCA package[101, 102]. Optimization was completed with an energy convergence of 10^{-9} Hartree and a root mean square force convergence of 10^{-6} Hartree/Bohr. The cc-pVDZ basis set[136] was used to compute the Hartree-Fock (HF) orbital energies. These HF orbitals were further used to calculate the ionization spectra with the one-particle Green's function formalism, the non-Dyson algebraic diagrammatic construction (ADC) approximation in the third order[137, 138]. The cationic states in this formalism are formally represented as an expansion of a series of electronic configurations, forming an electronic wavepacket. The propagation of these cationic states was simulated through the Lanczos algorithm[139] using the ADC(3) matrix. In order to trace the charge migration and associated electron dynamics, time dependent hole density is constructed and analyzed for computational convenience. This involves building the hole density matrix $N(t)$ based on the *ab initio* method, followed by its diagonalization to provide the natural charge orbitals $\tilde{\phi}_p(\overrightarrow{r}, t)$ and the hole occupation numbers. These are used to understand the sudden ionization induced ultrafast charge migration dynamics.

4.2 Photo-ionization spectra

The ionization spectra for keto-**U** and enol-**U** plotted up to 25 *eV* are given in Fig. 4.1(a) for keto and 4.1(b) for enol. The vertical lines are the cationic states, the corresponding energy is the ionization energy. The intensity of these lines is the ionization cross-section, which is given as the sum of every one-hole (1h) configuration and the associated weight presented in the configuration-interaction expansion of the corresponding state. The 1h configurations for each single orbital are colour-coded in Fig. 4.1. The single ionization potential energy calculated with the ADC method here is 8.98 *eV* for keto and 8.52 *eV* for enol. These values are in very close agreement with the experimental (9.20 *eV*) for keto-**U** and previously reported value computed with the G4 high-level *ab initio* method (8.91 *eV*[140]) for enol-**U**. The two ionization spectra show a considerable difference for the keto and enol forms. A strong correlation effect is prominent for multi-excitation or mixing between two orbitals; this can also be identified through spectral states with a smaller ionization cross-section. This correlation effect starts in the keto-form from 12.6 *eV* and from 10.8 *eV* in enol (see Fig. 4.1 a and b, respectively). Since the correlation effect is weak below

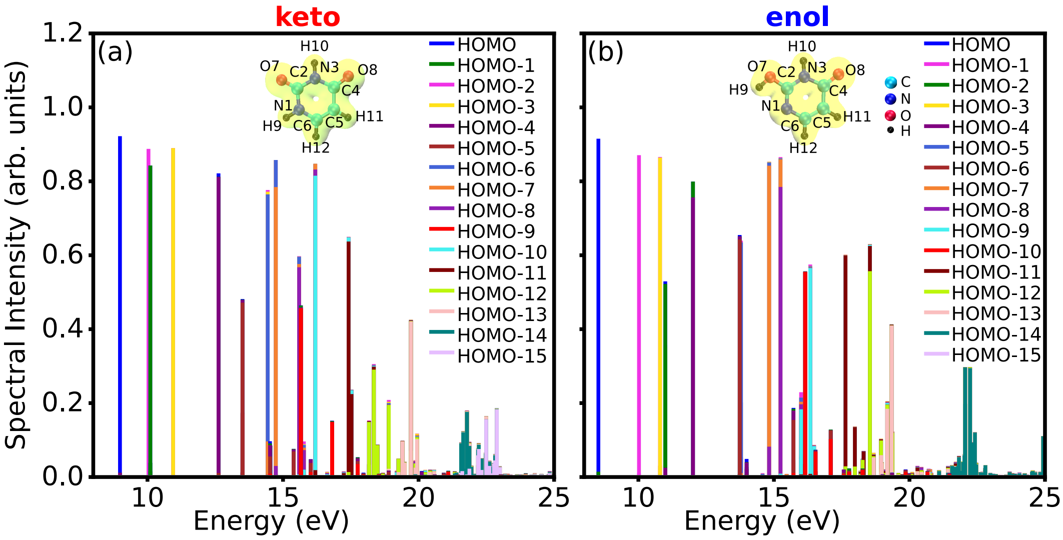

Figure 4.1: *Ionization spectra of (a) keto and (b) enol, with the corresponding molecular structures in inset.*

these energies, the molecular orbital picture is still valid. Hence, the Hartree-Fork and Koopman's theorems[43] are still justified approximations. The region from 12.6 *eV* to 19 *eV* for keto-**U** and from 10.8 *eV* to 20 *eV* for enol-**U** is described as a strong correlation regime. Here the heights of the lines decreases along with satellite states which appear as the weaker lines besides the main ones. In this regime, the states have a two-hole–one-particle (2h1p) character, which gives additional excitations on top of the ionization. At first glance, no clear distinction between the main lines can be seen beyond this region, and this is where the molecular orbital picture completely breaks. States in the latter are commonly known as shake-up states[26]. This very strong correlation enters the double-ionization continua of the molecules and is important in the study of molecular fragmentation[141, 142]. In this chapter I will discuss charge migration in regions with weak and strong electron-correlation effects.

4.3 Clocking the sudden ionization response time

I begin by examining the response of the two tautomers keto-**U** and enol-**U**, by ionizing their five highest occupied MOs. The response of the charge density to the created vacancy is addressed within a few attosecond (*as*), see Fig. 4.2. The curves given in both panels of Fig.4.2 show similar behaviour up to 60 *as*, when there is a sharp decrease in the $\tilde{n}_i(t)$ until a stationary point is reached. I marked these points as “response time”, and tabulated them in Table.4.1 for the first five molecular orbitals. After the first stationary point, the behaviour of the curves depends on the symmetry of the molecular orbitals. For all molecular orbitals with a′ symmetry, show identical temporal evolution of hole density and shortest response time. The shortest time can be explained with the nature of the a′ orbitals (see Fig.4.3). The a′ irreducible representation has a contribution from the σ orbitals of the molecular skeleton, which aids the overlap between the MOs and increases the interaction between the electrons occupying this symmetry [143]. In Fig.4.3 we can see that the charge density occupies most of the molecular structure, and hence slight charge

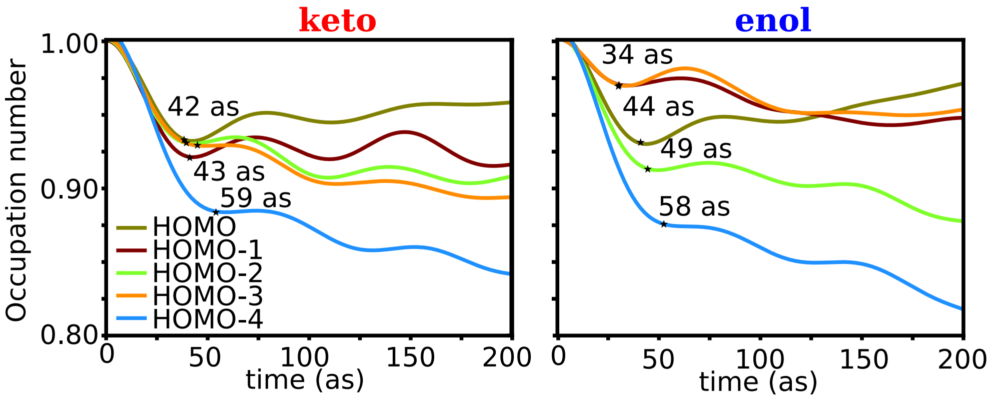

Figure 4.2: *Evolution of the hole-occupation numbers $\tilde{n}_i(t)$ for the first 200 as, after ionization of the five highest occupied molecular orbitals. The response time for each orbital is marked ("*") at the first stationary point in the corresponding $\tilde{n}_i(t)$ curve.*

delocalization is observed after ionization.

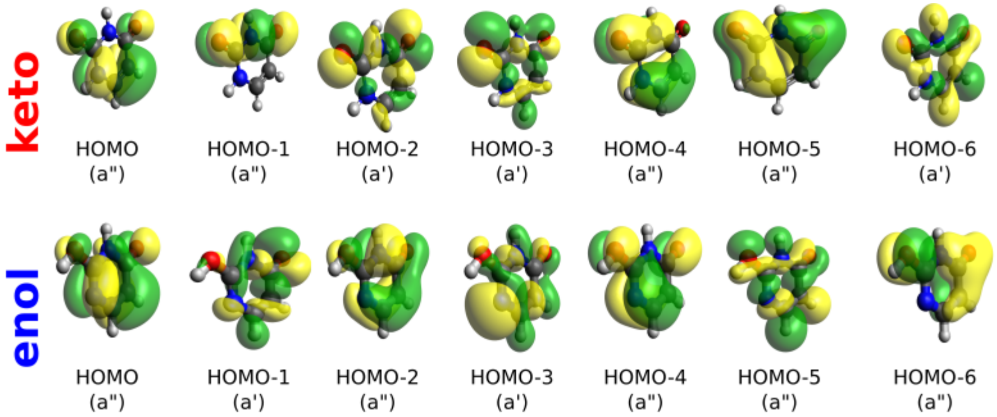

Figure 4.3: *HOMO to HOMO-6 orbitals in a$''$ and a$'$ symmetry for keto-**U** (upper row) and enol-**U** (lower row) (iso-surfaces of 0.02 e/Å^3).*

On the contrary, after the ionization of the a$''$ orbital, charge needs to be migrated from a relatively longer distance to fill in the vacancy. Another reason is the correlation effect. Electron correlation increases as one goes to deeper orbitals. The first orbitals lie in the region of weak correlation effects (see the ionization spectra in Fig4.1), whereas the last ones lie in the strong correlation regime. With stronger correlation, the response time increases from 40 to about 60 as. If we compare the overall response time of the two tautomers, we find that the response time for the a$'$ orbitals of enol-**U** is substantially shorter in (34 as) in comparison to that of keto-**U** (42 as). As the electron-correlation effect sets in, this difference in response time fades for the a$''$ orbitals of keto-**U** (HOMO, HOMO-1, and HOMO-4), and enol-**U** (HOMO, HOMO-2, and HOMO-4). A recent study on non-local electronic decays through carbon chains [144] has reported a correlation between an electronic process and the degree of electron correlation in time.

We further examine the evolution of the hole density using the snapshots of the ionized a$'$

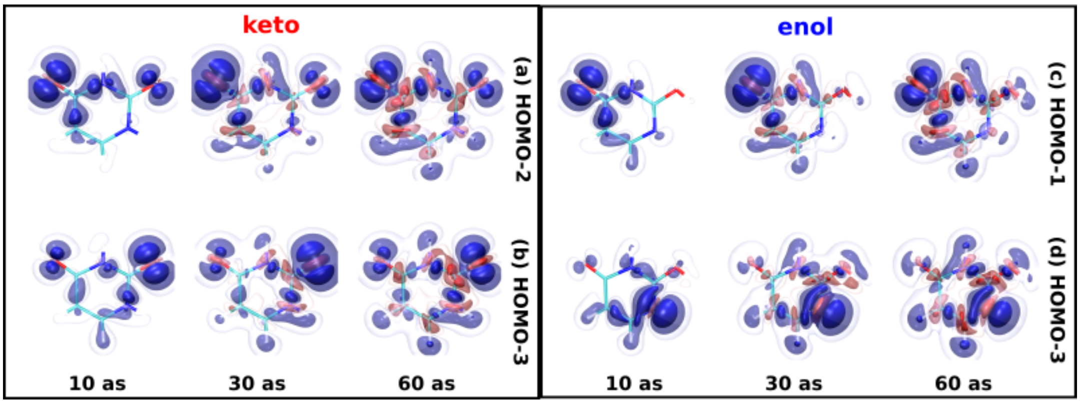

Figure 4.4: *Iso-surface of the hole density at 10 as, 30 as and 60 as after the sudden ionization of the two outermost molecular orbitals in a′ symmetry, (a, b) in keto-**U**, and (c, d) in enol-**U**. The iso-surfaces in blue and red represent hole and electron density, respectively. Decreasing opacity is used to indicate the different iso-surface values: ± 0.0128 arb. units, ± 0.0032 arb. units and ± 0.0008 arb. units.*

symmetry orbitals given in Fig. 4.4 and the temporal variation in charge density for each atomic site. The sudden ionization of the highest a′ orbitals given in Fig. 4.4 (a) and (c) for both tautomers triggers a very similar response. The hole density given by the blue iso-surface increases around all the hydrogen and the N3-C2 and C6-C5 bonds, while the electron density (red) appears around O8, C4, C5 and N3. Charge migration after the ionization of HOMO-3 demonstrates different dynamics for the two molecules. The first difference is between the localization of excess charge density on O7 for keto-**U**, and on N1 in enol-**U** (Fig. 4.4(b) and (d)). The overall dynamics in keto-**U** shows the electron transfer from C6-H12 to O7-C2. In enol-**U**, the exchange-correlation hole is occupied by electrons migrating from H10-N3 and O7-Ht. Electron density is also observed to build up around C2 and C6.

The response of a″ orbitals to sudden ionization is same for both structures. The molecular orbitals are localized either on the HOMO C5-C6-N1, on HOMO-1 or enol HOMO-2 O7-N3-O8, or HOMO-4 O7-N3 and C6-N1 segments (see Fig.4.5). Irrespective of the location of the created hole density, the migrating electrons originate from the H10 and C6-H12 sites in all three cases. The density variation in keto-**U** is found to be stronger than in enol-**U**, and except for in HOMO, Ht is the electron donating site.

If the positive charge decreases, it is assumed that electrons flow towards that site, whereas if the positive charge increases, electrons are assumed to move away from the atom. We present this using the maximum-variation time, τ, which is defined as the first minimum/maximum in $\frac{\partial Q(\vec{r},t)}{\partial t}$ (see Fig.4.6). From the maximum variation on O and N, it can be understood that this quantity (τ) is strongly dependent on the electronegativity of the atom. In Table. 4.1 we see that the maximum variation time for O is always shorter than that for N. This is just the initial response within the first 60 *as*; we discuss the evolution of charge density in the femtosecond (*fs*) timescale for the same two systems in the next section.

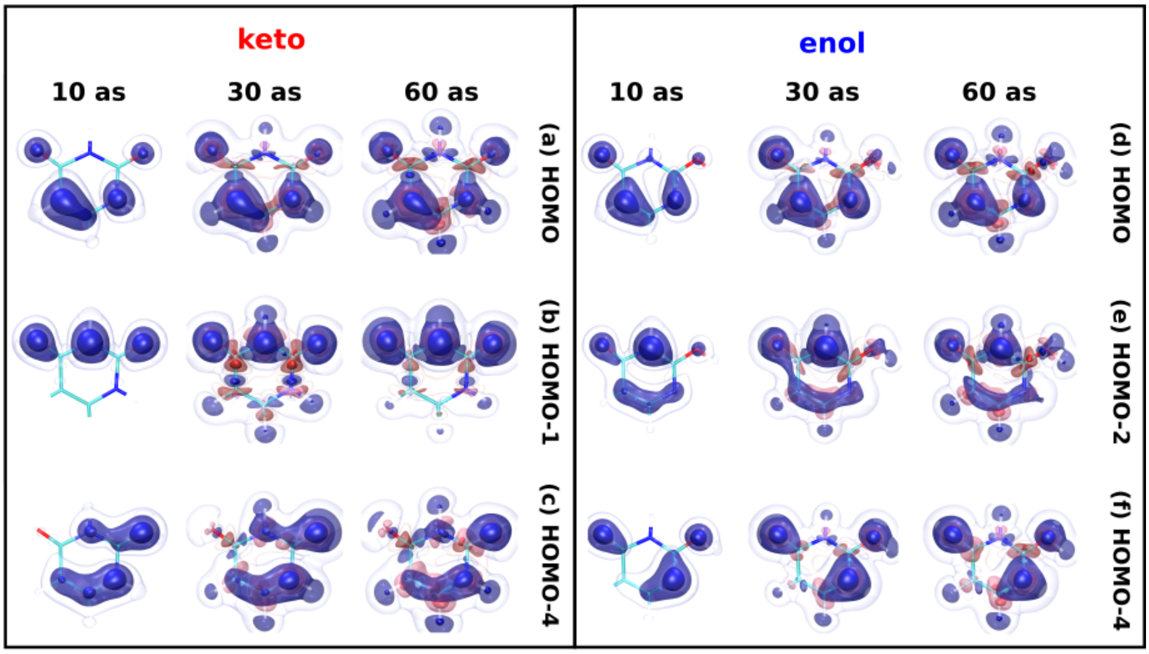

Figure 4.5: *Iso-surface of the hole density at 10 as, 30 as and 60 as after the sudden ionization of the two outermost molecular orbitals in the a″ symmetry, (a, b) in keto-**U**, and (c, d) in enol-**U**. The iso-surfaces in blue and red represent hole and electron density, respectively. Decreasing opacity is used to indicate the different iso-surface values: ± 0.0128 arb. units, ± 0.0032 arb. units and ± 0.0008 arb. units).*

Table 4.1: *The overall electronic response time to the removal of an electron from the five outermost molecular orbitals of keto-**U** and enol-**U**, and the maximum-variation time (τ) at the atomic site with the highest charge density response is given in brackets.*

tautomer	molecular orbital	symmetry	response time [*as*]	maximum-variation time [*as*] (atom)
keto-**U**	HOMO	a″	42	24 (N1)
	HOMO−1	a″	43	18 (O7)
	HOMO−2	a′	42	18 (O8)
	HOMO−3	a′	42	18 (O7)
	HOMO−4	a″	59	18 (O7)
enol-**U**	HOMO	a″	44	24 (N1)
	HOMO−1	a′	34	18 (O8)
	HOMO−2	a″	49	19 (O7)
	HOMO−3	a′	34	21 (N1)
	HOMO−4	a″	58	17 (O7)

4.4 Femtosecond charge migration dynamics

The investigation of pure correlated charge migration dynamics in the femtosecond regime is important for the development of a molecular design based on electron correlation[24, 145, 146,

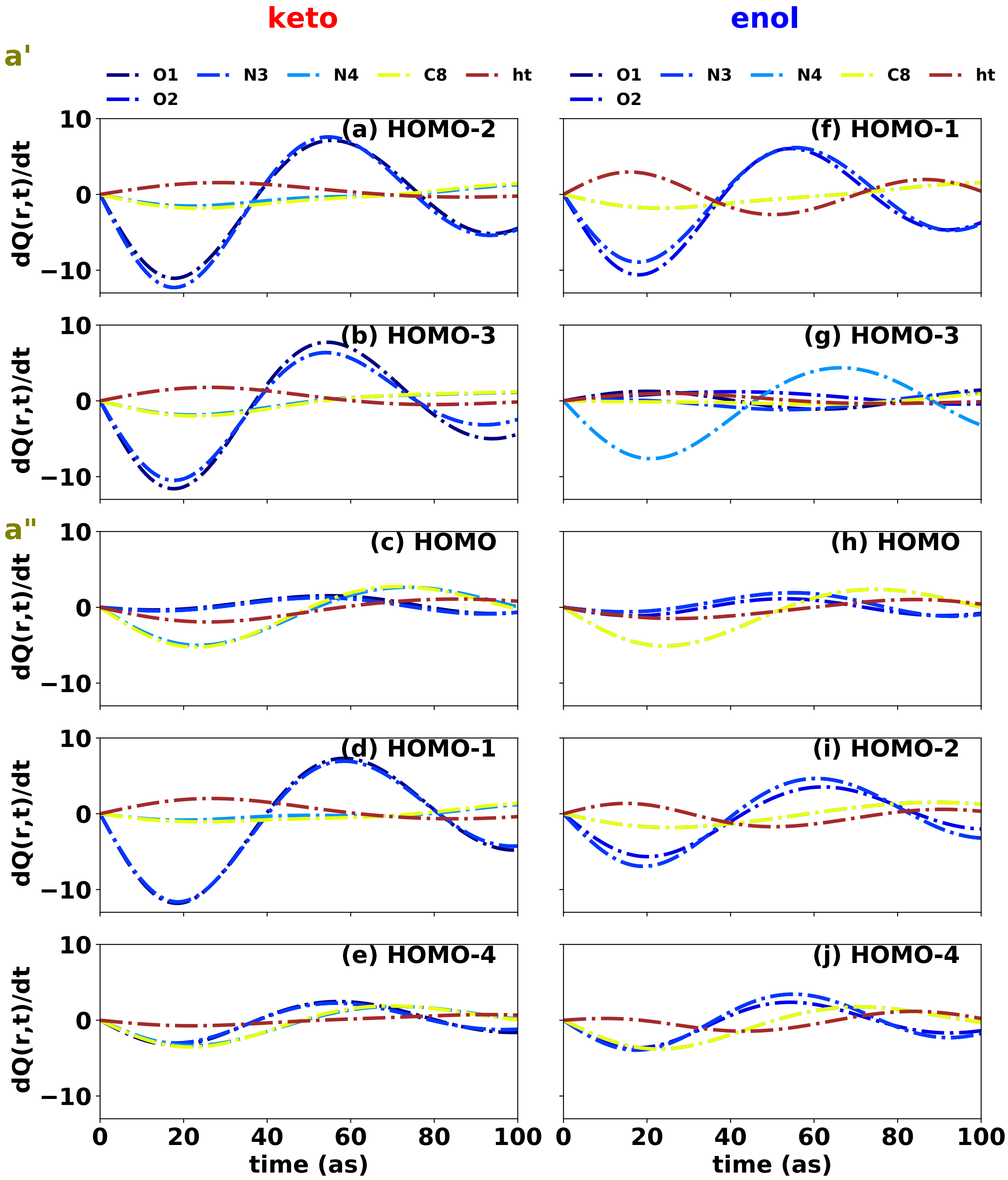

Figure 4.6: *Rate of change in hole density, $dQ(\vec{r},t)/dt$, at selected molecular sites. Blue dash-dot line for O7, light blue dotted line for N3, orange solid line for N1, purple dashed line for C5, brown dash-dot line for Ht, and light blue dashed line for O8.*

147]. This study helps us understand several photo-chemical processes, such as: prediction of photo-protection or photo-damage of RNAs, DNAs, or any bio-molecules in general [33, 34, 35].

The investigation of these processes is essential as they can lead to irreversible damage when the DNA/RNA nucleobases are modified by ring-opening, or by the fragmentation of nucleobases[36]. Photo-protective effects, such as photo-tautomerization, are reversible[38, 39]. To analyze charge migration in **U** and its tautomers, we study the global response of all the states excited by a broadband XUV pulse, which is capable of exciting all states from weak to strong electron-correlation (up to 15 *eV*). For example, in case of **U**, the broadband pulse can excite states from HOMO to HOMO-6. This type of attosecond pulse is produced using the high harmonic generation technique using rare gases. Above the selected energy (15 *eV*) a different theoretical approach needs to be considered due to the correlation band structure and associated non-adiabatic dynamics[148, 149].

To study the global response we first calculate the hole density after the ionization of each molecular orbital from HOMO to HOMO-6 using Eq. (2.29). As **U** is in C_s symmetry, we can divide the orbitals into those with a$'$ and a$''$ symmetry. Thanks to the advanced techniques available for the alignment and orientation of molecules with laser pulse, the selection of a particular MO is possible, although not yet trivial. The hole density at each time step from all orbitals was added and renormalized for each symmetry. The snapshots of such global response is presented in Fig. 4.8. Before discussing the global response we examine the dynamics for orbitals which show a strong correlation effect such as HOMO-4 and HOMO-5 of keto-**U** and HOMO-4 and HOMO-6 of enol-**U** (see Fig. 4.7). As the correlation effect is weak in the other orbitals, no prominent CMD is anticipated.

The ionization of keto-U

In Fig.4.1(a) HOMO-4 of the keto-**U** tautomer has a typical satellite structure. This satellite structure has 1h contribution from both HOMO-4 and HOMO-5. Hence, after the ionization of HOMO-4, one will coherently populate two cationic states. The energy difference (ω) between the two purple (HOMO-4 at 12.6 *eV*) and the brown (HOMO-5 at 13.5 *eV*) states in Fig.4.1(a) is 0.9 *eV*. After ionization, the hole density initially occupying the HOMO-4 orbital will oscillate in the molecule with a period of $\sim$4.6 *fs* ($t = \frac{2\pi}{\omega}$). In Fig. 4.7(a) we can see three crossings: at each crossing, the nature of the charge orbital interchanges between the two coherently excited states such as, HOMO-4 (magenta) and HOMO-5 (green). For cosmetic purposes and for obtaining a better understanding, we show the interchange between the orbitals by changing the colours assigned to HOMO-4 and HOMO-5. During charge migration, the contribution coming from the HOMO-4 or HOMO-5 orbitals are highlighted with coloured circles around the iso-surfaces. In the first 5 *fs*, the major charge oscillates between the O7 and N1 sites.

Similarly, after the ionization of HOMO-5, the main state at 13.5 *eV*, and the satellite states at 14.43 *eV* and 15.39 *eV* are excited. Again here a prominent contribution comes from the 1h configuration of HOMO-4 and HOMO-5 for a state at 13.5 *eV*. The charge migration dynamics resulting from the ionization of HOMO-5 (see Fig. 4.7(b)), is charge oscillation from O8 to N1 via the N3 atomic site. Due to the satellite states, some part of the charge is excited to LUMO.

The ionization of enol-U

Fig. 4.1(b) indicates that the ionization of enol-**U** HOMO-4 will result in a complex satellite structure and hole mixing between the HOMO-2 states at 10.99 *eV* and 12.01 *eV*. CMD shown in Fig. 4.7(c) indicates more charge delocalization from the O8 to the N1 site. This delocalization is stronger in comparison to CMD in HOMO-4 of keto-**U**, where the charge mainly oscillates between the O7 and N1 sites. Unlike the HOMO-4 of keto-**U**, the ionization of HOMO-4 of enol-**U**

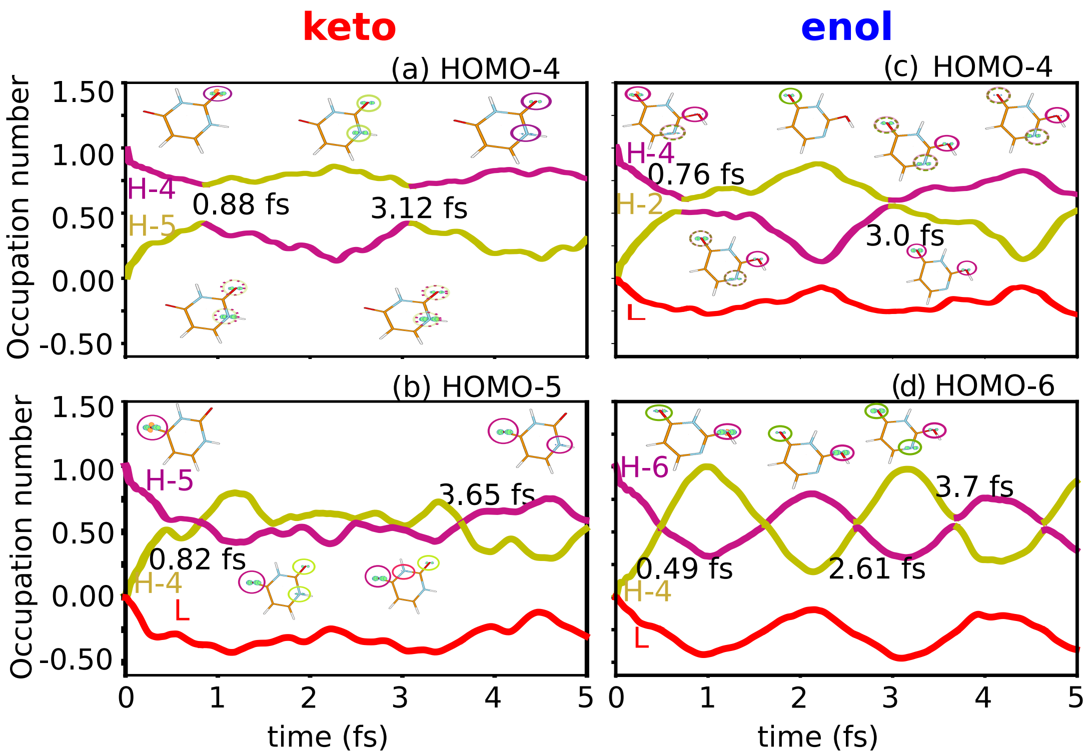

Figure 4.7: *The temporal evolution of hole density after the photo-ionization of (a) HOMO−4, (b) HOMO−5, of keto-**U** (iso-value 0.01 e/Å^3, hole density in green and electron density in orange), (c) HOMO−4, (d) HOMO−6 of enol-**U** (with an iso-value of 0.03 charge/Å^3). The coloured circles surrounding the iso-surface represent the corresponding molecular orbitals contributing during charge migration.*

excites an electrons to LUMO. Similarly, Fig. 4.1(b) shows a complex satellite structure after the ionization of HOMO−6. The main state can be seen at 13.74 *eV*, while the satellite states are found at 13.99 *eV*, 15.72 *eV* and 17.1 *eV*. Cationic states at 13.99 *eV* and 15.72 *eV* show 1h configuration from HOMO−6 and HOMO−4. CMD after the ionization of HOMO−6 of enol-**U** shows more frequent crossing between the HOMO−4 and HOMO−6 orbitals, however the initial charge response originates from the O atoms and the overall charge oscillates between O8 to N1.

In summary, photo-ionization of individual orbitals of both tautomers show different behaviour with different patterns and timescales. We can see clear charge oscillation between N1 and O7, ionization of HOMO-4, between O8 to N1 for HOMO-5 of keto-**U**. Enol-**U** orbitals in comparison to keto-**U** orbitals after the ionization, show fast and pronounced charge oscillation between O8 to N1, the HOMO-4 and HOMO-6 orbitals.

Global response

The study of the global response to photo-ionization includes the response from all excited states at once. The important question is whether the difference in the dynamics discussed above will remain or get washed out after taking the incoherent sum of the temporal hole density? As I mentioned, the average of the hole density is taken by summing the hole density on a′ within

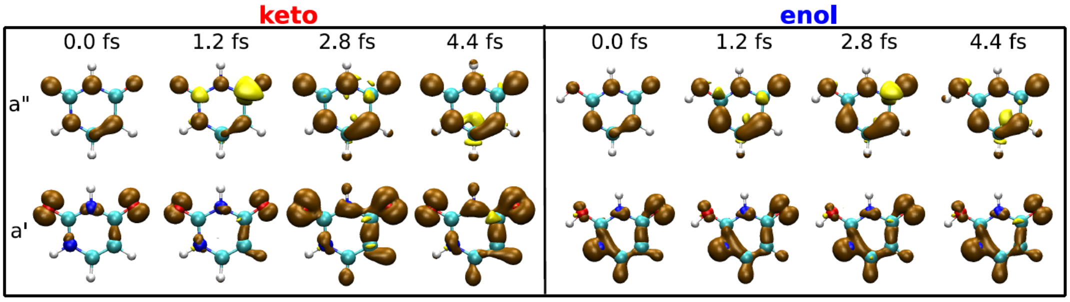

Figure 4.8: *Snapshots of the averaged temporal hole density at 0.0 fs, 1.2 fs, 2.8 fs, and 4.4 fs after the photo-ionization of orbitals in a$''$ (top row) and a$'$ (bottom row) symmetry of keto (left panel) and enol (right panel). The brown iso-surface (0.005 a.u.) and the yellow iso-surface (-1×10^{-6} a.u.) represent hole density and electron density, respectively.*

15 *eV* and renormalizing it and repeating the same for the a$''$ orbitals. The snapshots for 0.0 *fs*, 1.2 *fs*, 2.8 *fs* and 4.4 *fs* are shown in Fig.4.8.

Fig. 4.8 (upper left) shows an overall decrease in hole density on O7, O8, N3, N1, C6, and C5 and an increase in electron density on C2 and C4 at $t = 1.2\,fs$ compared to $t = 0\,fs$ after the ionization of a$''$ keto-**U** orbitals. CMD triggered by ionizing a$''$ orbitals of keto-**U** and enol-**U** shows an opposite behaviour. Fig. 4.8 (upper right panel) shows an increase in hole density on the O7, O8, N3, N1, C6, and C5 sites, and electron density increases on C2 and C4 along with the C6 and O7 sites. Keto-**U** at $t = 2.8\,fs$ shows the migration of electron density from C4 to N3 and C5, while the C5 site shows the localization of electron density for enol-**U**. At $t = 4.4\,fs$, the C6 and N1 sites of keto-**U** show localized electron density, while enol-**U** shows delocalized charge density on the O7, C6, C5, and C4 sites. Overall, in both tautomers strong charge oscillations are anticipated after the photo-ionization of a$''$ orbitals. The effect of charge migration on these sites could be reflected in the subsequent electron-nuclei coupled dynamics. Furthermore, the analysis of the averaged CMD after the ionization of a$'$ orbitals for keto-**U** shows (Fig. 4.8 left panel) an increase of hole around H11 and C5, while enol shows a decrease in hole density at C5 and H11 (Fig. 4.8 lower right row). The ionization of a$'$ orbitals results in varying charge distribution for both tautomeric forms.

Recent experimental and theoretical reports show that charge migration driven by the correlation effect can strongly impact the fragmentation pattern of a molecule through double ionization [142, 150]. The localization of hole density results in weak bonds, hence promotes fragmentation after the second ionization [142]. If one uses this interpretation then it can be presumed that keto-**U** will manifest bond-breaking along O8-C4 and H11-C5, while for enol-**U** the N1-C6 and N1-C2 bonds might break. Hence, if one compares the orbitals in different symmetry, different non-adiabatic dynamics is expected. Compared to keto-**U**, enol-**U** shows more and faster charge delocalization. This implies that when it comes down to fragmentation, the enol-**U** a$'$ orbitals will be more resistant to radiation damage.

Summary and conclusions

In summary, in this chapter I presented and discussed the ionization spectra, the differential response to sudden ionization and the subsequent femtosecond response in CMD for two tautomeric forms of **U**. This study reveals that the electronic cloud responds differently to sudden perturbation depending on factors such as: (i) electron correlation, (ii) symmetry of molecular orbital, and (iii) the tautomeric form of the molecule. The two tautomeric forms of **U** appear to be structurally and electronically similar, however the response time of the two outermost σ-electrons to sudden ionization is ~ 42 as in keto-**U** and ~ 34 as in enol-**U**. The investigation of the local variations in the electronic cloud reveals the dependence of CMD on the degree of correlation and electronegativity of atoms. The former is observed through an increase in response time on going from HOMO (weak correlation effect) to HOMO-4 (keto-**U**)/ HOMO-6 (enol-**U**) a$''$ (strong correlation effect), whereas the latter is observed through the response of the tautomeric hydrogen, which acts as an electron donor (except in case of HOMO). To investigate the sub-*fs* pure CMD we consider all outer-valence orbitals (7 in total) for both tautomers, populated by a 15 *eV* ultrashort XUV pulse. I presented the individual and the averaged orbital CMD and showed that even though most of the correlation-driven charge-migration dynamics is washed out by averaging, still both tautomers respond differently to XUV photo-ionization. For the photo-ionization of individual keto-**U** a$''$ orbitals the CMD become more delocalized as one goes toward highly correlated orbitals, or in orbitals with a$'$ symmetry. In case of enol-**U**, the charges are more delocalized and show faster charge migration dynamics compared to keto-**U**. After averaging, the pronounced difference between the two orbital symmetries and tautomeric forms still persists. Are these distinctive CMD features specific for **U** or typically holds true for other systems as well? To address this, we further study other tautomeric and isomeric forms of other nucleobases in the following chapter.

Chapter 5

The Effect of Different Molecular Structures on CMD

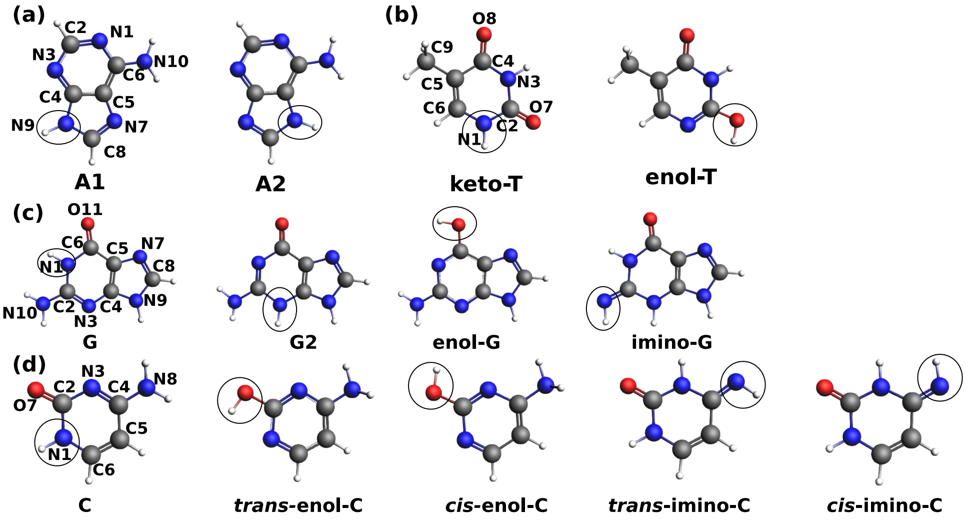
(a)
C2
N1
N3
N10
C6
C4
C5
N9
N7
C8
A1
A2
(b)
O8
C9
C4
C5
N3
C6
O7
N1
C2
keto-T
enol-T
(c)
O11
C6
C5
N7
N1
C8
N10
C2
C4
N9
N3
G
G2
enol-G
imino-G
(d)
N3
N8
C2
C4
O7
C5
N1
C6
C
trans-enol-C
cis-enol-C
trans-imino-C
cis-imino-C

Figure 5.1: *Molecular structures of different tautomers of DNA nucleobases, (a)* ***A****, (b)* ***T****, (c)* ***G****, and (d)* ***C****. The black circle highlights the position of the tautomeric hydrogen. The numbering of atoms is given for each parent nucleobase (****A, T, G, C****) and it remains the same for the corresponding tautomeric forms.*

In Chapter 4 we reported a prominent difference in charge delocalization and CMD between the keto-enol tautomers. Tautomerization from keto-**U** to enol-**U** resulted in the formation of a π-conjugate bond by the enolic carbon with the neighbouring nitrogen. The formation of the π-conjugate bond is known to be favoured by a molecule over a proton (except in nitroso-oxime systems) [151]. The study of CMD in real time helps us to visualize the difference in delocalizations of charge promoted by the two tautomeric π-conjugated systems. From the CMD discussed in Chapter 4 we concluded that highly delocalized charge migration dynamics results from the ionization of a strongly correlated molecular orbital. Here I will present the results for DNA nucleobases adenine

(**A**), thymine (**T**), guanine (**G**) and cytosine (**C**); along with their different tautomers: keto-enol amino-imino, and cis-trans isomers (see Fig. 5.1). The study of charge migration dynamics in the nucleobases is interesting due to the radiation damage in the genetic material caused by the ionization of these building blocks[152, 153, 154]. Radiation damage to the DNA can be caused directly by the ionization of nucleobases or indirectly through free radicals, low energy electrons or ions created by ionizing radiation[155]. Radiation can lead to permanent or reversible damage to the system[152]. Later I will investigate the homocyclic and heterocyclic systems to understand the role of aromaticity on CMD. Aromaticity is an important property as it gives stability to a cyclic molecule, which has π bonds in resonance and typically has a planar structure. The theoretical method and the steps to analyze CMD are described in detail in Chapter 2 (Sec. 2.3 to 2.5) and Chapter 4, respectively. For each of the systems given in Fig. 5.1, I first discussed the ionization spectra and then selected the MO, which shows a strong correlation effect, then I study the CMD for that MO.

5.1 DNA nucleobases

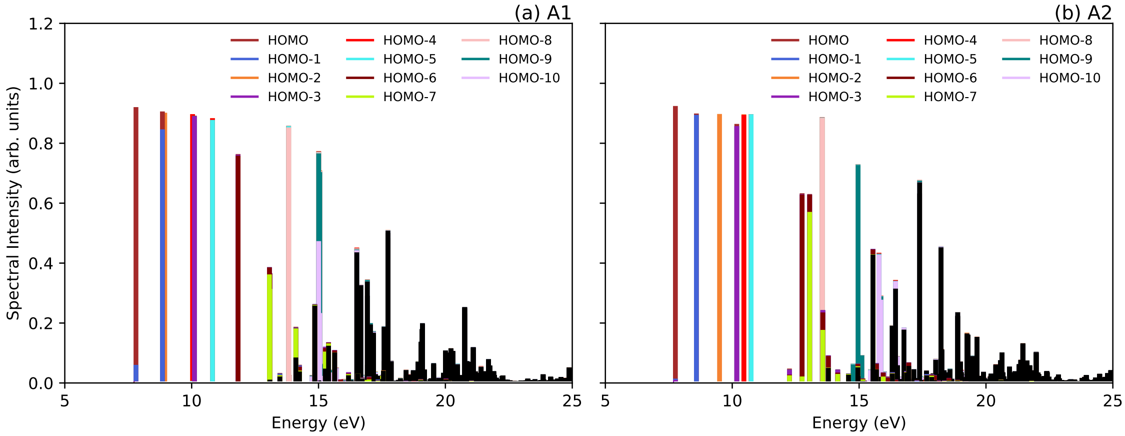

Figure 5.2: *Ionization spectra for the tautomers of adenine*

Adenine (**A**), cytosine (**C**), thymine (**T**) and guanine (**G**) are the nucleobases in the construction of DNA and RNA (except **T**). All the nucleobases are found in C_s symmetry. In RNA, the **T** unit is replaced with the **U** nucleobase. Charge migration dynamics in **U** and the subsequent non-adiabatic dynamics are discussed in Chapter 4 and Chapter 6, respectively. The nucleobases **U**, **T** and **C** are pyrimidine derivatives and are also known as pyrimidine bases. The purine derivatives, **A** and **G** have been hot molecules for the study of ultrafast dynamics. Since the late seventies, numerous experimental efforts have shown that the electron loss created in the DNA model initiated at **A** ends at the **G** site[156, 157, 158]. L. P. Candelas et al. reported the ultrafast migration of oxidative damage from adenylyl($3' \rightarrow 5'$)guanosine[158]. Erik P. Mansson et al. reported the correlation driven charge migration dynamics in **A** cation[150]. In their study, they measured an intact doubly ionized **A** molecule by delaying the NIR probe pulse with 3 *fs*. The first ionization was induced by the XUV pump pulse, while the second one was triggered by the probe pulse. In their report the intact doubly ionized **A** cation was explained by many-body excitation resulting in charge inflation mechanism[150]. Erik P. Mansson et al. also discussed the controlled multi-electronic dissociative dynamics in molecule **A** using different delayed probe pulses[141]. V. Despre et. al. reported that the intact doubly ionized **A** at a given probe delay by the above mentioned experiments could be generated due to the change in the nature of hole density from localized s-type to delocalized p-type[142]. To give an insight into the non-adiabatic dynamics and the fragmentation channel mentioned earlier, I will first present our results on CMD for **A** and identify the charge oscillation sites, which can give a preliminary insight into the subsequent fragmentation channels that are reported in the articles referred to above. To study charge migration in **A**, we selected two tautomers that differ with respect to the position of the tautomeric hydrogen, (Ht) forming N9-Ht and N7-Ht bonds in **A1** and **A2**, respectively (see Fig.5.1(a) for the position of atoms in molecule). The ionization potential calculated for **A1** and **A2** is 7.86 *eV* and 7.80 *eV*, respectively, using the cc-pVDZ basis set [136]. In the ionization spectra for **A1**, the first two cationic states have a major 1h contribution from HOMO-1 and HOMO-2, and the fourth and sixth cationic states from HOMO-4 and HOMO-5. We calculate the energy difference between the cationic states with the 1h configuration from HOMO-4 and HOMO-5 as < 0.2 *eV* (see Fig.5.2(a)). All states in the ionization spectra of **A2** are well separated (see Fig.5.2(b)). The HOMO and HOMO-1 orbitals show strong hole mixing in the ionization spectra of **A1**, but weak in **A2**. For both molecules the satellite states have major contribution from HOMO-6 and HOMO-7. For **A1** the energy difference is larger between the cationic states with major 1h contribution from HOMO-6 and HOMO-7, hence the oscillation time period is anticipated to be shorter than in **A2**. Therefore, for the charge migration analysis (CMA) I will analyze the ionized HOMO-7 orbitals for both molecules.

(a) HOMO-7 (A1)

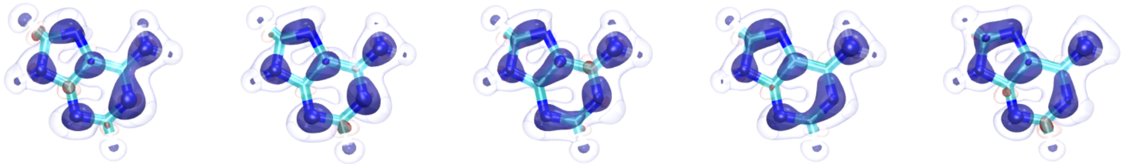

(b) HOMO-7 (A2)

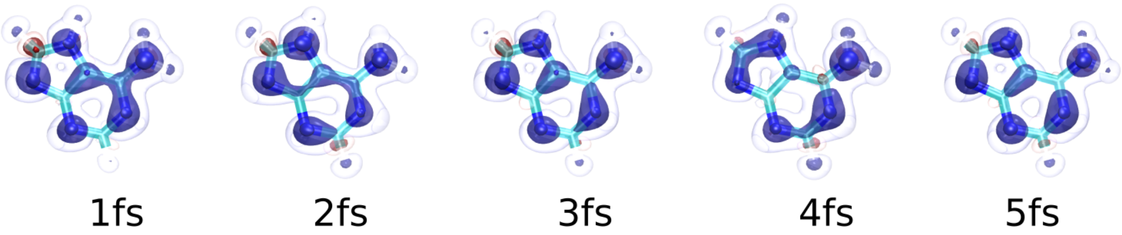

Figure 5.3: *CMD in adenine tautomers in 5 fs after the ionization of the HOMO-7 molecular orbital.*

After the sudden ionization of HOMO-7, at 1 *fs* the hole density on the amino group increases. This suggests the initial electrons are donated by the amino group to the six-member ring, for both **A1** and **A2** molecules. This hole density in **A1** appears to migrate towards the N10-C6-N1 region of the six-member ring (see hole localization at 2 *fs* in Fig. 5.3(a)). Later, charge density appears to migrate to the five-member ring in **A1**. After the ionization of the HOMO-7 molecular orbital of **A2**, I find that the hole density donated by the amino group is distributed not only along the N10-C6-N1 region, but also along N10-C6-C5 (see hole localization at 1 *fs* in Fig. 5.3(b)). After the temporal evolution of the charge density the π-electrons delocalization on the entire **A2** molecule (see 2 *fs* in Fig. 5.3(b)). This kind of delocalization in **A1** can be seen 5 *fs* after the ionization of HOMO-7. Hence, a small modification in the position of the tautomeric hydrogen is very effective in modifying charge delocalization in π-conjugated molecules. We continued to study the effect of tautomerization for other nucleobases in addition to the effect of methyl as donor in **T** and rotational isomerization (cis-trans).

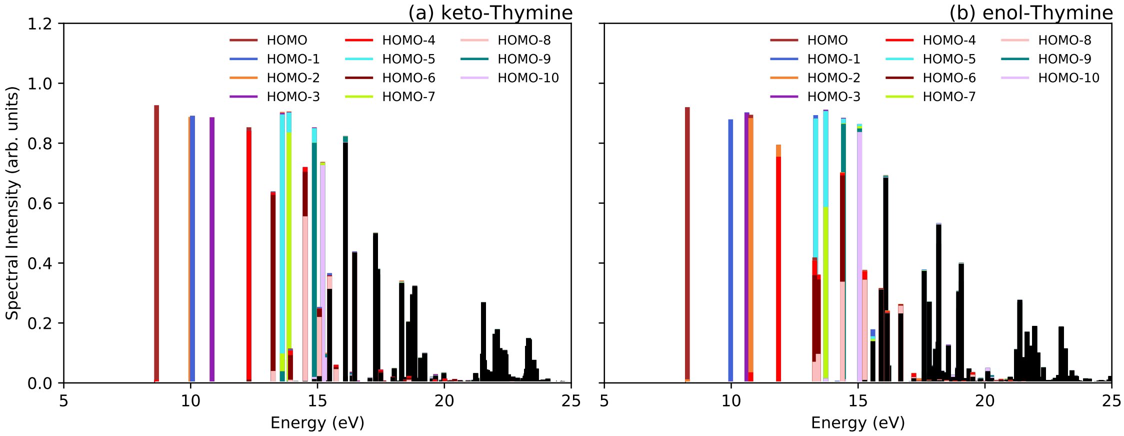

Figure 5.4: *Ionization spectra for the tautomers of thymine*

T is one of the DNA nucleobases; the difference between **U** (RNA nucleobase) and **T** is the presence of a methyl group on the C5 atomic site (see Fig.5.1(b)). S. Maclot et al. studied the dissociation pathways for a thymidine system[159]. E. P. Mansson et. al. reported that a pump-probe study on a thymine and thymidine shows ultrafast decaying between the electronic states through the non-adiabatic coupling[160]. K. W. Choi et al. were the first to report high-resolution ionization spectroscopy for **T**[161] and give the precise value of 8.9178 *eV* as the ionization potential for the ground state vibrational structure of **T**.

Next, I describe the effect of keto-enol tautomerization in the **T** molecule on ultrafast charge migration dynamics. Comparing the ionization spectra in Fig. 5.4(b) enol-**T** show a red shift in the single ionization potential by 0.38 *eV* (first cationic state) with respect to keto-**T** (see Fig.5.4(a)). Similar shift is reported in this thesis by enol-**U** (see Chapter 4). The position of the cationic states with a weak correlation effect from a′ type orbitals does not show a strong shift ($(\delta\ E) < 0.25$ *eV*). For example, see the positions of cations with contributions from a′ orbitals, HOMO-2, HOMO-3 in keto-**T** and HOMO-1 and HOMO-3 in enol-**T**. Investigating the shift for the 1h contribution from a″ type orbitals (keto-**T**: HOMO and HOMO-1, HOMO-4; enol-**T**: HOMO, HOMO-2 and HOMO-4), shows a strong red shift of $\delta\ E$ >0.35 *eV* in the ionization potential. As the correlation effect gets stronger, these shifts are no longer valid as in this energy regime we see a breakdown of the molecular-orbital picture of ionization[26]. Hole mixing between HOMO-2 and HOMO-4 is seen for enol-**T**, similarly between HOMO-4 and HOMO-6 in keto-**T**. Complex satellite states with 2h1p contribution from a′ orbitals, HOMO-5, HOMO-7 and HOMO-9 can be seen for both tautomers of **T**. Additionally, the a″ orbitals, HOMO-6, and HOMO-8 for both keto- and enol-**T** also show complex satellite states with a slight 1h contribution from HOMO-4. The HOMO-6 orbital shows a strong correlation effect in both molecules. Hence, to compare CMD I ionized the same orbital for both keto- and enol-**T** (see Fig. 5.5).

(a) HOMO-6 (keto-T)

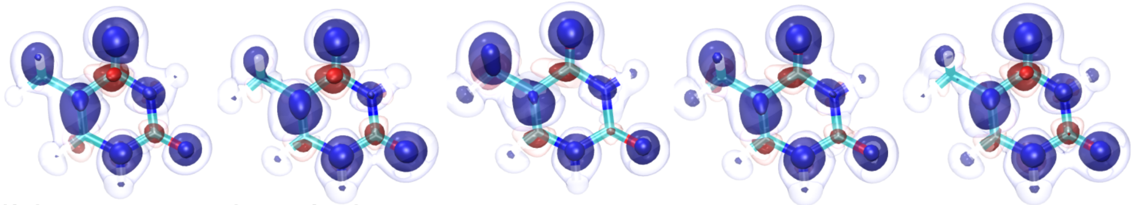

(b) HOMO-6 (enol-T)

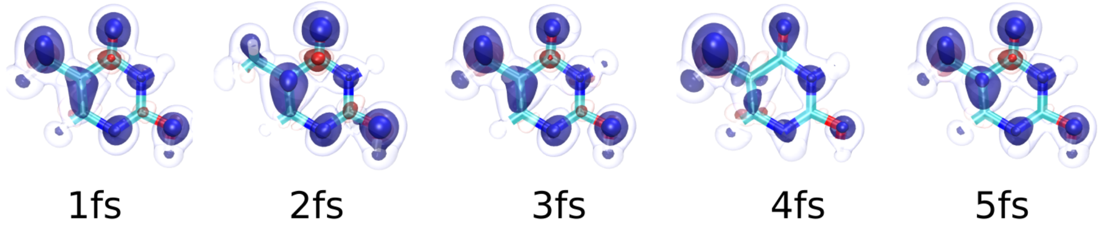

Figure 5.5: *CMD in thymine tautomers in 5 fs after the ionization of HOMO-6.*

In Fig. 5.5 I present the CMD up to 5 *fs*, triggered by the sudden ionization of the HOMO-6 orbital of keto-**T** (Fig. 5.5(a)) and enol-**T** (Fig. 5.5(b)). As CMD is triggered the methyl group donates the charge density to the six-member ring in **T**. As discussed for **U** and **A**, the sp^3 hybridized N has localized charge density. Hole density appears to be oscillating on the methyl group faster in the keto-**T** (see Fig.5.5(a) 1 *fs*, 2 *fs*, 5 *fs*) than in the enol form (see Fig.5.5(a) 1 *fs*, 2 *fs*). When comparing the iso-surface appearance the methyl group on enol-**T** has more hole density than on keto-**T**. This shows that the donated charge from enol-**T** is more delocalized in comparison to keto-**T**. The change in hole density on C9-C6-C5 region; as well as in electron density on C4 for keto-**T** indicates an oscillation of charge between these two sites. The structure of keto-**T** in Fig.5.1(b) shows that these sites are π-conjugated. However, after the tautomerization of keto-**T** to enol-**T**, this π-conjugation is extended by the presence of a double bond between N1 and C2. This extended π-conjugation leads to charge delocalization along all sites of enol-**T** except for the N3 site (see Fig.5.5 (b)).

According to the Watson-Crick arrangement, the **G-C** units are paired through hydrogen bonding. G. A. Green et al. reported a novel theoretical method to study the effective ultrafast quantum dynamics induced by the photo-excitation of the **G-C** pair[162]. They calculated that the majority of the excited state population on **G** and **C** decay to the charge transfer state within 50 *fs*[162]. The **G** nucleobase has been in the focus of research, as it is known for its lowest oxidation potential[163], and it is a well-studied fact that the **G** radical cation is capable of oxidizing one **G** or **GGG** stack. The latter has an even lower ionization potential, and has been reported as the “hole traps”[164]. These traps created by the ionization of the **GGG** stack are of massive biological importance as they might lead to drastic effects like gene mutation[165]. Hence, studying **G** and

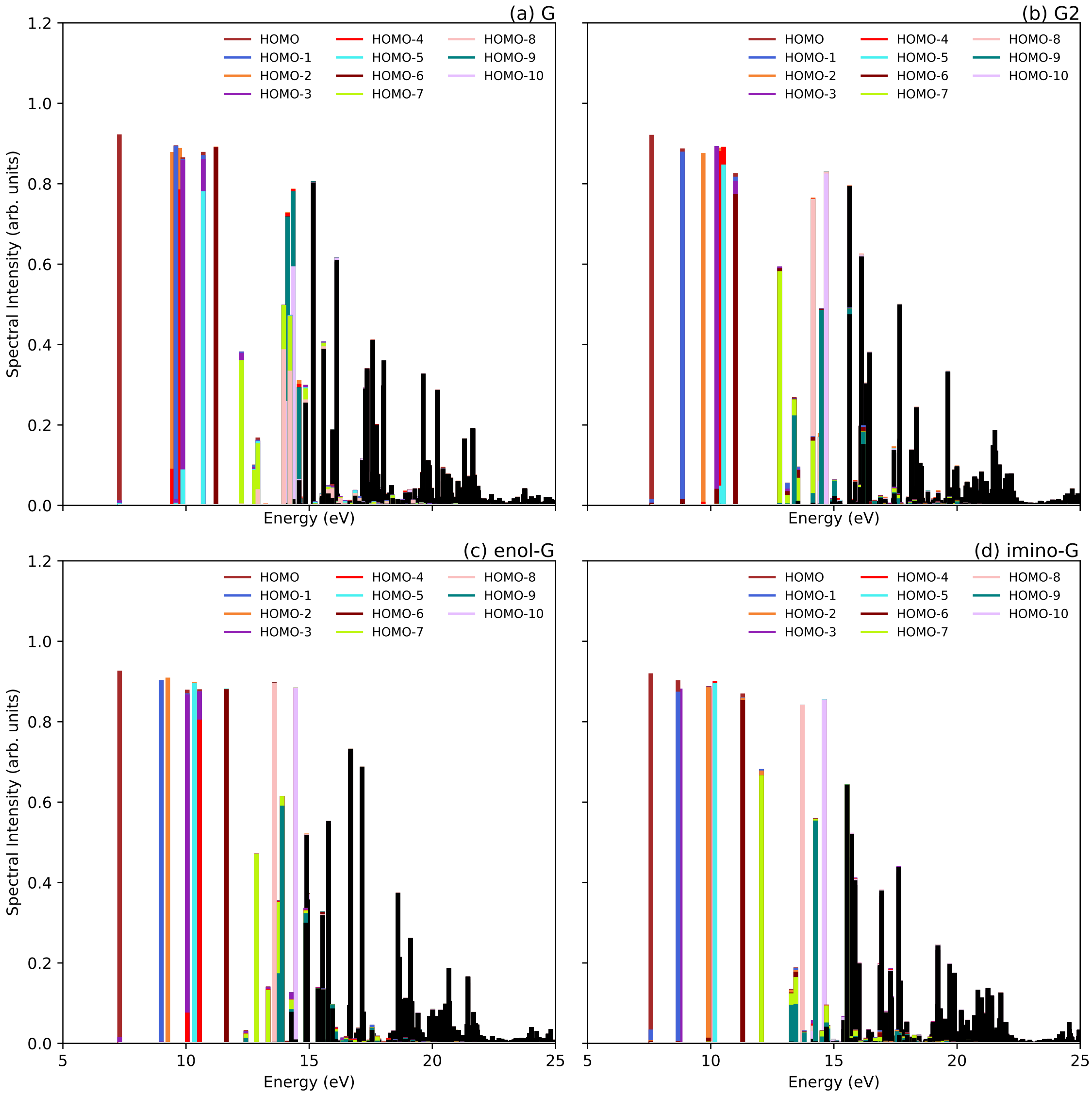

Figure 5.6: *Ionization spectra for the tautomers of guanine*

its tautomers is of great importance.

The ionization spectra for the four **G** isomers are given in Fig. 5.6, while the molecular structure of these molecules can be found in Fig. 5.1(c). The single ionization potential for **G**, **G2**, enol-**G** and imino-**G** is 7.293 *eV*, 7.568 *eV*, 7.304 *eV* and 7.602 *eV*, respectively. From the ionization spectra for **G** HOMO and HOMO-3, and HOMO-3 and HOMO-5 show 1h mixing (see Fig. 5.6(a)). In addition to that, cationic states with 2h1p configuration show hole mixing between HOMO-3, HOMO-5 and HOMO-7 around 12 *eV*. In Fig. 5.6(b) cationic states show hole mixing with major 1h contributions from HOMO and HOMO-1 (below and around 10 *eV*), and HOMO-3 and HOMO-6 (>10 *eV*) in **G2**. The cationic states with 2h1p configuration are seen with major contributions from HOMO-

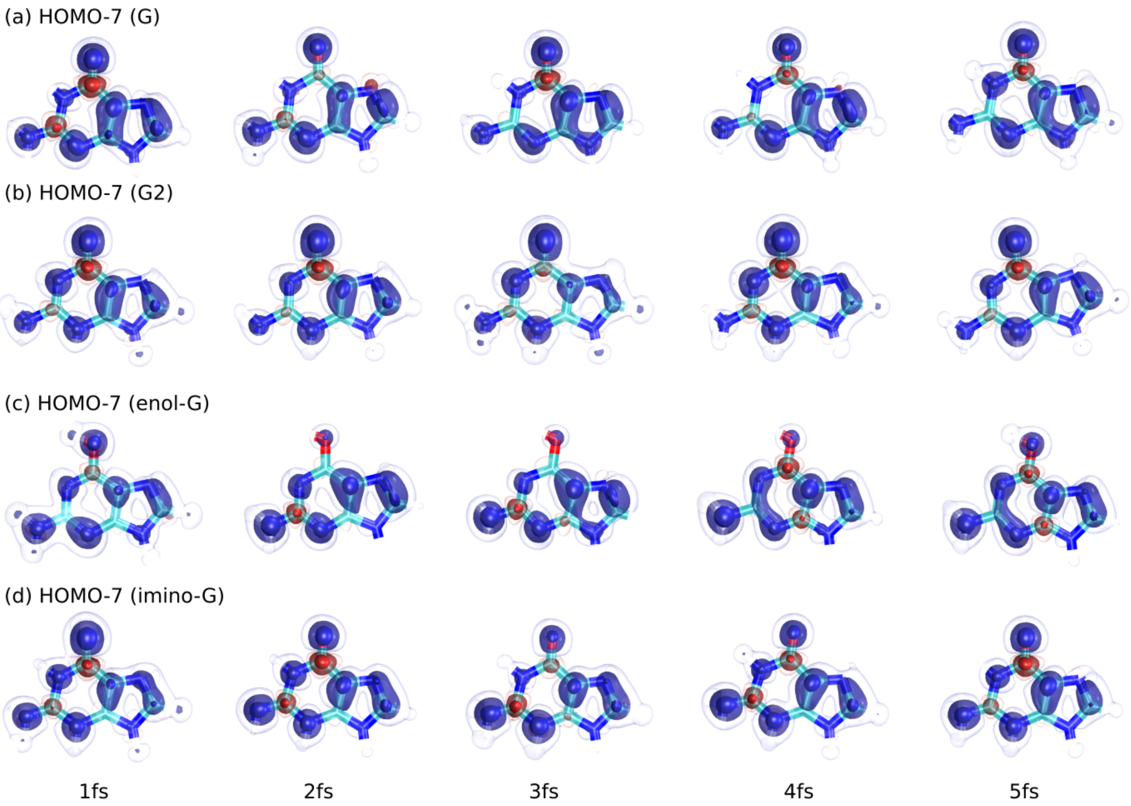

Figure 5.7: *CMD in guanine tautomers in 5 fs after the ionization of HOMO-7.*

7 and HOMO-9, and with minor contribution from HOMO-6. The ionization spectra of enol-**G** shows hole mixing between HOMO and HOMO-3; HOMO-3 and HOMO-4 with 1h configuration (see Fig. 5.6(c)). Satellite states with 2h1p configuration shows major contributions from HOMO-7 and HOMO-9. For the imino-**G** tautomer the hole mixing is seen for cationic states with 1h configuration from HOMO and HOMO-1; HOMO-2 and HOMO-6 (see Fig. 5.6(d)). Satellite states with 2h1p configuration are seen with major contributions from HOMO-7 and HOMO-9, and with minor contributions from the states mentioned above for imino-**G**. From these ionization spectra I can see strong correlation between HOMO-7 and HOMO-9 for all the isomers of **G**. Hence, the charge migration dynamics for the HOMO-7 orbital of all four isomers of **G** are presented in Fig. 5.7.

The important thing to notice for **G** and **A** is the presence of two rings with different aromaticity. The five-member ring both for **A** and **G** has higher aromaticity in comparison to their six-member ring counterpart[166]. Due to the difference in aromaticity, more charge delocalizes in the five-member ring of **A1** in Fig. 5.3(a). The tautomerization of **A1** to **A2** leads to decreased aromaticity in the five-member ring and a slight increase in the six-member ring, which leads to an increase in delocalized charge density for **A2**. The aromaticity difference and the delocalization of charge density for **G** is consistent.

After the sudden ionization of HOMO-7 in **G** (see Fig. 5.7(a)) more hole density delocalizes on the five-member ring. We witness the oscillation of electron density (red iso-surface) on the C6 and C2 sites. After tautomerization, the hydrogen moves from N1 to N3, which redistributes the charge density. In case of **G**, the hole density was localized on N10 and N3 and showed a very a slight change in the density for the 5 *fs* after ionization. After the ionization of HOMO-7 of **G2**, the hole density is distributed on N1 and N3 (see Fig. 5.7(b)). The hole density in the five-member ring appears to be less delocalized in comparison to **G**. This shows that a slight variation in the position of hydrogen can impact the delocalization of charge density, and hence the aromaticity.

After the keto-enol isomerization of **G**, see the structure of **G** and enol-**G** in Fig. 5.1(c), I witness a very prominent change in the aromaticity of the two tautomers. Interestingly the six-member ring that appeared to have a slight delocalization of hole density after the ionization of HOMO-7 of **G** and **G2** shows the opposite effect for enol-**G** (see 4 *fs* and 5 *fs* in Fig. 5.7(c)). The six-member ring is attached to the **C** ring through the hydrogen bonding on the N10 and N3 sites. This new redistribution of charge density might certainly affect the charge transfer between the **G-C** pair in DNA. When comparing enol-**G** and imino-**G** (see Fig. 5.1(c and d)), I noticed that after the ionization of HOMO-7 of imino-**G**, less prominent CMD is initiated on the five-member ring. In **G** the electron density oscillates between the C6 and C2 sites, but at a lower magnitude with respect to the iso-surface value. This low delocalization of charge density can be interpreted as localization of charge density in the molecule.

Among the five tautomers of **C** presented in Fig. 5.1(d), π-conjugation on the entire molecule of **C** is present due to the lone pair on the N1 site and alternating double bonds. Tautomerization from keto- to enol-**C** makes the ring of enol-**C** aromatic in nature, and rotational isomerization from cis- to trans- enol-**C** can help in understanding the pure hindrance in charge migration. Two enol tautomers of **C** are also reported as highly aromatic, as their rings have $(4N + 2)$ π-electron type and thereby fulfill the Hückel rule. On the other hand, the imino-**C** tautomer has alternate double and single bonds, forming π-conjugation within the N8-C4-C5-C6 region. The cis- and trans-imino-**C** tautomers have the least aromaticity in comparison to the other three **C** tautomers[166]. However, the lone pair on N3 within the ring can act as a delocalized lone pair, and extends this π-conjugation [167]. In the discussion of CMD in the tautomers of **C**, where the lone pairs are present, I will discuss if electron delocalization through them is apparent after photo-ionization. Z. Chen et al., reported the adiabatic ionization energies for the gas-phase *C* tautomers, which were produced in the molecular beam[168]. Through this experiment, the isomerization and tautomerization effect and the presence of various stable cytosine isomers were realized with experimental precision. This work also estimates varying charge redistribution with any change in the structure of cytosine.

The ionization potential calculated using the ADC method for **C** (8.255 *eV*), *cis*-enol-**C** (8.294 *eV*), *trans*-enol-**C** (8.292 *eV*), *cis*-imino-**C** (8.392 *eV*), and *trans*-imino-**C** (8.373 *eV*) shows that rotational isomerism has a less significant effect on the ionization potential than tautomerization (see Fig.5.8). The energy of the cationic states in a weak correlation regime for the a′ orbitals, HOMO-2 and HOMO-4 is close ($\delta\ E < 0.25$ *eV*) to the position of the a″ HOMO-1 and HOMO-3. However, the cationic states for **C**, and two imino-**C** show well separated cationic states in the region of the weak correlation regime. Except for **C**, no strong hole mixing is observed below 13 *eV*. For **C** cationic states separated by $\delta\ E = 0.46$ *eV* show hole mixing between HOMO-2 and HOMO-3. Beyond 13 *eV*, satellite states have 2h1p configuration from HOMO-4, HOMO-5 and slight contribution from HOMO-9 orbitals for **C** and imino-**C**, whereas for enol-**C** from HOMO-3, HOMO-5 and HOMO-8. In some cases, hole mixing between HOMO-6 and HOMO-7 is also seen. Hence, for comparison, I will study the CMD on HOMO-5 for **C** and its tautomers as it shows strong correlation effect for all structures of **C** presented here.

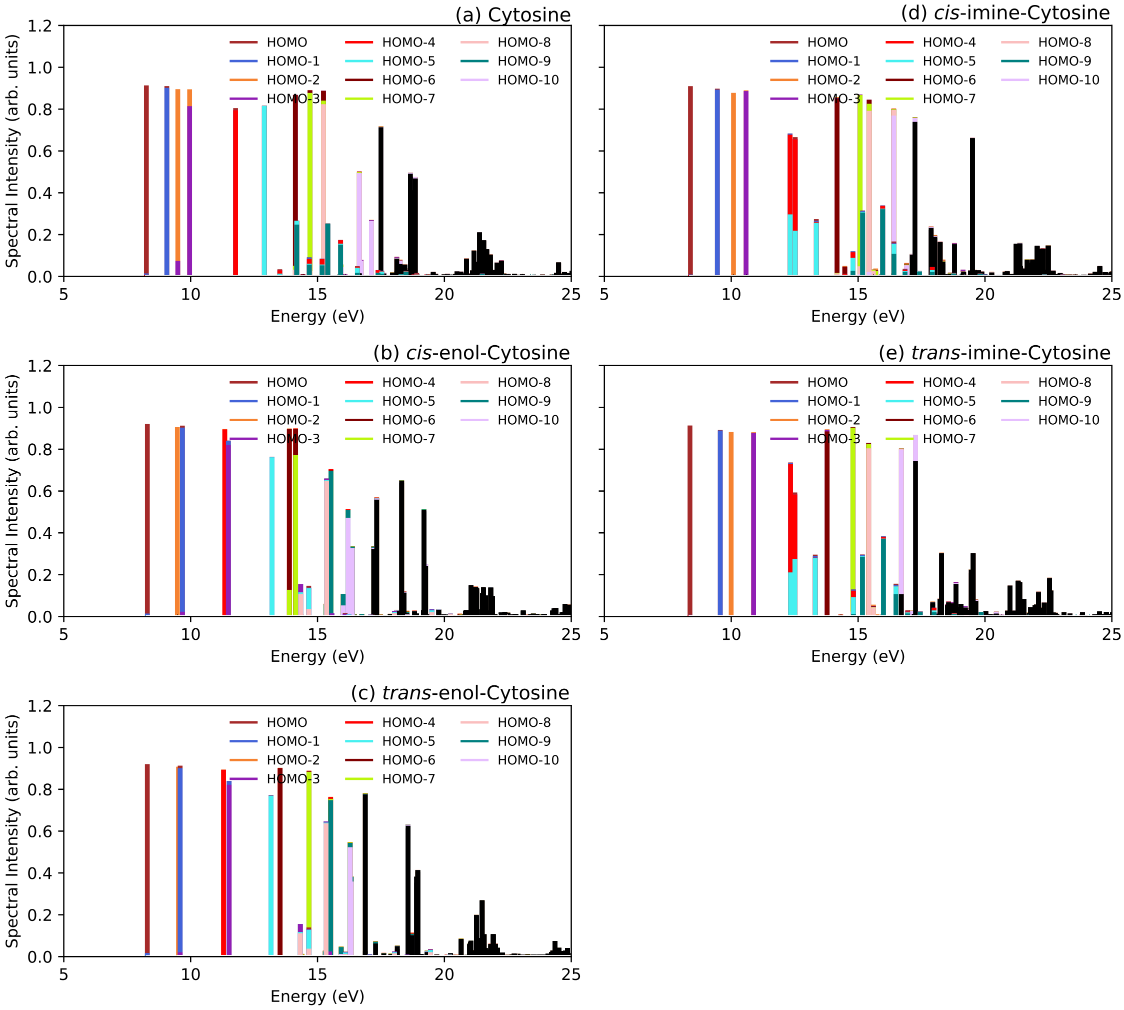

Figure 5.8: *Ionization spectra for the tautomers of cytosine*

The CMD in **C** shows a variation in electron density on the C2, C4 and C6 endocyclic atomic sites (see Fig.5.9(a)) along with the change in hole density on N3 and C5. A similar trend – but with more delocalized hole density – is observed in case of enol-**C**, irrespective of the rotational isomerism (see Fig.5.9(b,c)). As mentioned earlier, former reports[166, 169, 170] suggest that the aromaticity of an imino-**C** system is less than that of **C** or its enol-derivatives. However, in *trans*-imino-**C**, Fig.5.10(a), at 1 *fs*, charge delocalizes around the N3-C4-N8 region due to the lone pair on N3 atoms. At 4 *fs*, hole delocalizes in the N1-C6-C5 region. Such delocalization was also witnessed in *cis*-imino-**C** at 4 *fs* and 5 *fs* after the ionization of HOMO-5.

The investigation of charge migration dynamics in the different tautomers of the DNA nucleobases can be summarized as follows: Tautomerization from the keto to enol tautomer form for **T**, **G** and **C** has shown very prominent differences in charge migration dynamics. The keto-form of the molecules has been found to localize the charge density on the oxygen and the N atomic sites in the vicinity, while the enol-form tends to delocalize charge density on the major part of

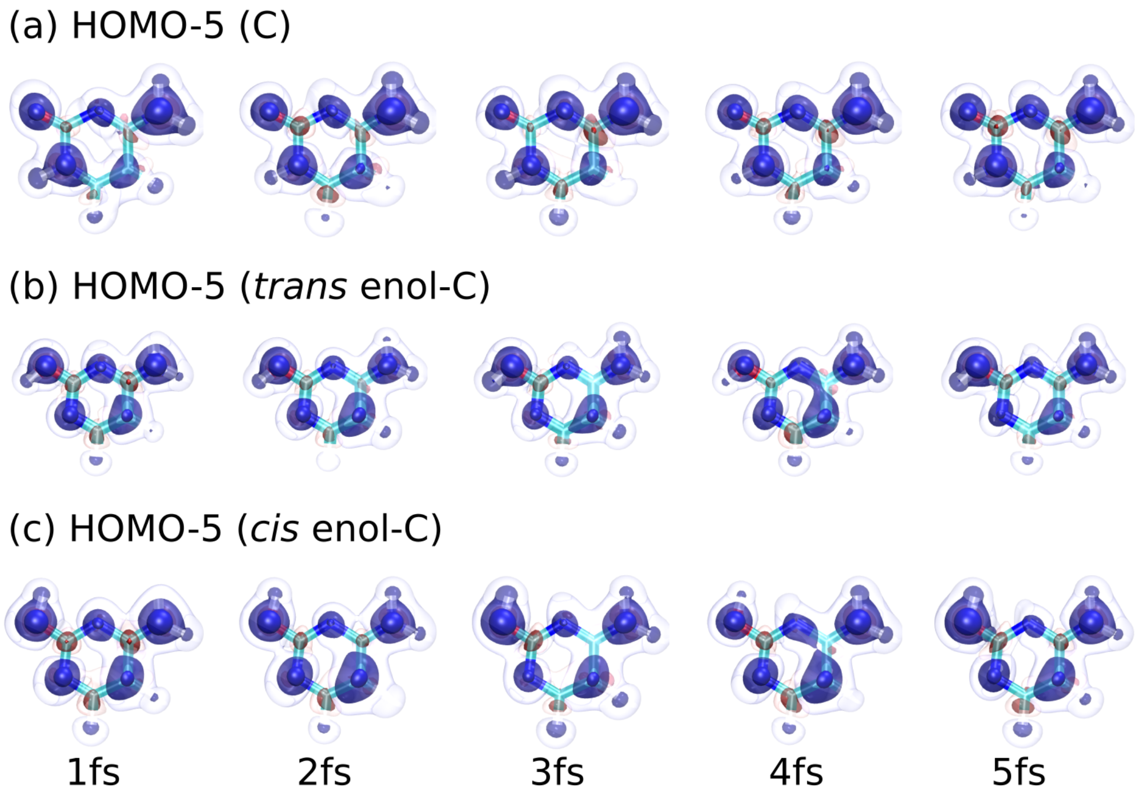

Figure 5.9: *CMD in cytosine, and the cis-trans isomers of enol-cytosine in 5 fs after the ionization of HOMO-5.*

the system. Tautomerization in **A1** and **A2** has led to the increased delocalization of hole density between five- and six-member rings. The imino-form of tautomers both in **G** and **C** has shown a less prominent delocalization of hole density in comparison to enol-forms. However, when compared to the keto-form, in imino-tautomers the charge migration is more delocalized. Hence, in case of molecular modelling for highly delocalized charge density, tautomerization from the keto- to enol-form or the keto- to imino-form is helpful.

5.2 Pi-spacers

In a large extended system π-spacer groups play an important role in charge transfer from donor to acceptor after photo-excitation or photo-ionization. Selecting an appropriate π-spacer for designing an efficient molecule is like finding a needle in a haystack. Hence, in order to select wisely we need to understanding the charge migration in these systems. To compare and understand the groups better I choose to study some well known systems, which were synthesized for the development of efficient photo-conversion devices[171, 172, 173]. The seven systems used in this study are: (i) pyrrole, (ii) cyclopentadiene, (iii) 2,1,3-benzothiadiazole, (iv) furan, (v) thiophene, (vi) 1,2,5-thiadiazole, and (vii) 1,2-thiazole (see Fig. 5.11). These are cyclic and planar molecules with five-membered ring or fused five- and six-membered ring. Amongst the seven

(a) HOMO-5 (*trans* imino-C)

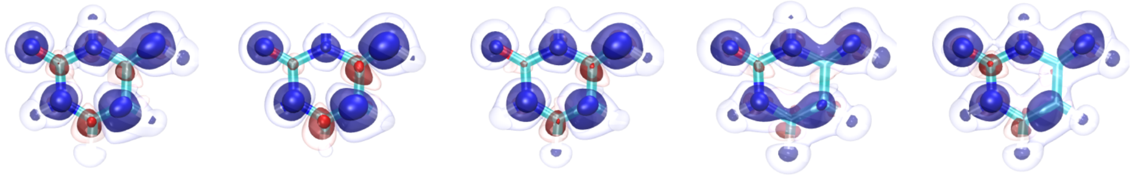

(b) HOMO-5 (*cis* imino-C)

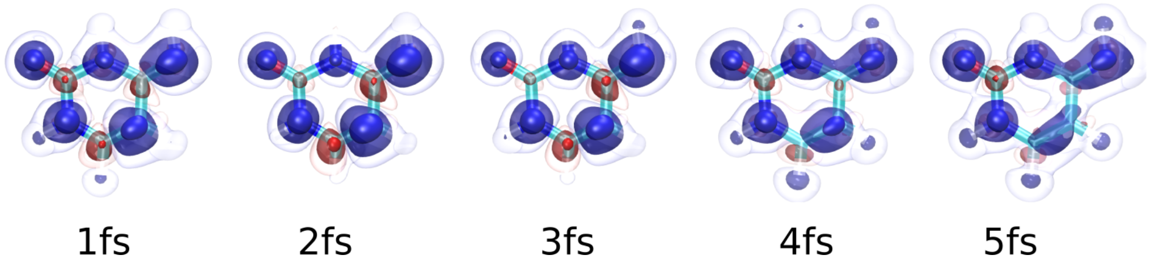
1fs
2fs
3fs
4fs
5fs

Figure 5.10: *CMD in cis-trans isomers of imino-cytosine at 1 fs to 5 fs after the ionization of HOMO-5.*

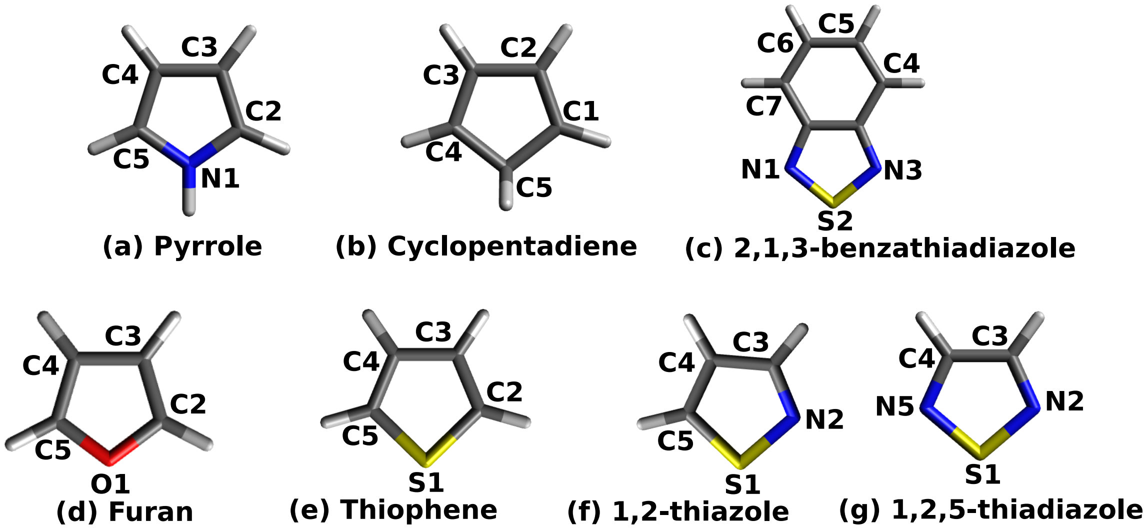
C3
C4
C2
C5
N1
C2
C3
C1
C4
C5
C5
C6
C4
C7
N1
N3
S2
C3
C4
C2
C5
O1
C3
C4
C2
C5
S1
C3
C4
N2
C5
S1
C3
C4
N5
N2
S1

(a) Pyrrole **(b) Cyclopentadiene** **(c) 2,1,3-benzathiadiazole**

(d) Furan **(e) Thiophene** **(f) 1,2-thiazole** **(g) 1,2,5-thiadiazole**

Figure 5.11: *Molecular structure for (a) pyrrole, (b) cyclopentadiene, (c) 2,1,3-benzothiadiazole, (d) furan, (e) thiophene, (f) 1,2-thiazole and (g) 1,2,5-thiadiazole.*

selected π-spacers, cyclopentadiene is homocyclic and not aromatic in nature; for the other five-member heterocycle, the order of aromaticity reported using the nucleus independent chemical shift (NICS) and the aromaticity index, is thiophene $>$ 1,2-thiazole $>$ 1,2,5-thiadiazole $>$ pyrrole $>$ furan $>$ cyclopentadiene[174, 175, 176]. The 2,1,3-benzothiodiazole system is known to be an efficient electron-acceptor system[176, 177]. The aromaticity for the benzene ring in

2,1,3-benzothiodiazole is lower than for the five-member heterocyclic ring [178, 179] Although aromaticity is used and studied extensively, measuring and predicting aromaticity for hetero-cyclic compounds is difficult[174, 177]. We cannot measure the aromaticity of the compound, however we can visualize the effect of aromaticity on CMD in these systems throughout our study.

Most of the systems studied in this section are in C_{2v} symmetry and have four irreducible representations. Hence, the region showing a weak correlation effect is broad compared to systems with C_s symmetry. Applying the same analysis used so far, I select the following orbitals for the study of CMD in pyrrole: HOMO-4, cyclopentadiene: HOMO-1, 2,1,3-benzothiadiazole: HOMO-2 and HOMO-4, furan: HOMO-2 and HOMO-3, thiophene: HOMO-3, 1,2-thiazole: HOMO-4, and 1,2,5-thiadiazole: HOMO-3 and HOMO-4 (see Fig.5.12). In the aromatic ring of pyrrole, the hole density is delocalized on the entire system. When the maximum hole density is on the adjacent C=C double bonds, the electron density is localized on the nitrogen atoms (see Fig.5.13((a) at 1 *fs*)). As the hole density moves towards the nitrogen site, the electron density is observed on all four C atoms (see Fig.5.13((a) at 3 *fs*)). As cyclopentadiene is not aromatic in nature, the π-conjugation remains mainly restricted to the alternate double bonds. The small variation in charge density on the non-conjugated C site is due to the correlation effect with the molecular orbitals (see Fig.5.13(b)). The aromaticity index for the five-member ring is reported to be higher than for the benzene ring present in 2,1,3-benzothiadiazole [178, 179]. This effect can be understood through the CMD after the ionization of both HOMO-2 and HOMO-4 (see Fig.5.13(c and d)). The charge delocalizes over the π-conjugated space and reveals the resonance structures for the five-member ring. However, on the six-member ring low hole density is seen, which supports the electron-poor character of the system. When 2,1,3-benzothiadiazole is part of a larger system, it is attached to the other neighbouring groups through the six-member ring. This ring thus acts as an electron-withdrawing group[171]. This effect is clearly observed at 5 *fs* after the ionization of HOMO-2 (see Fig.5.13(c)), whereas it appears to be stationary after the ionization of HOMO-4 (see Fig.5.13(d)). Furan is reported to be less aromatic in comparison to the other hetero-cyclic five-member systems[174, 175, 176]. The main reason behind this is that 'C' connected to electronegative heteroatoms such as 'O' are less shielded. The hole density localized on the C5-O1-C2 site in furan after the ionization of HOMO-2 is presented in Fig.5.13(e). This localized hole density is delocalized over the full furan molecule 2 *fs* after the ionization of HOMO-3 (see 2 *fs* to 5 *fs* Fig.5.13(f)). The effect on aromaticity by additions of hetero atoms to the thiophene-ring can be studied by comparing the thiophene, 1,2-thiazole and 1,2,5-thiadiazole. Due to the high aromaticity index, hole density after the ionization of HOMO-3 and HOMO-4 or thiophene and 1,2-thiazole, respectively is delocalized over the entire system (see Fig.5.13(g and h)). However, due to the presence of one more hetero atom in the ring of 1,2-thiazole, hole density is constantly localized on the S1 and C5 sites, and the electron density oscillates along the N2-C3-C4-C5 region. I found that charge density after the ionization of HOMO-4 of 1,2-thiazole is more delocalized compared to HOMO-4 of 1,2,5-thiadiazole (see Fig.5.13(j)).

5.3 Summary and conclusions

In this chapter I summarized the effects of different tautomeric forms and isomeric forms on the charge migration dynamics for the four nucleobases in DNA. Furthermore, I investigated the CMD in homocyclic and hetorcyclic systems along with the nucleobases to study the effect of aromaticity on the CMD. Aromaticity is a complex term and is not an easily measurable quantity. However, based on the natural resonance theory and nucleus independent chemical shifts, one can estimate

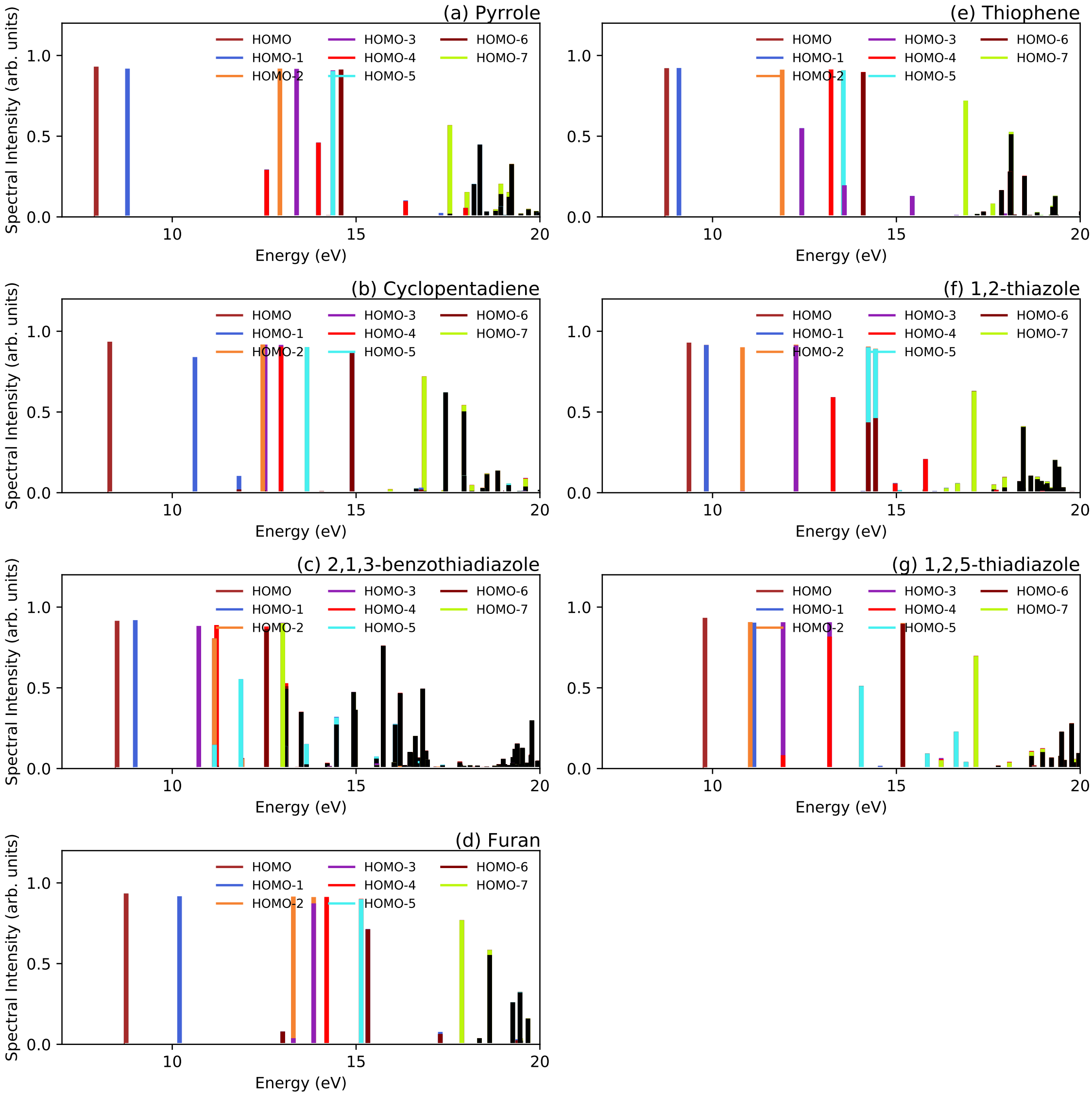

Figure 5.12: *Ionization spectra up to 25 eV for (a) pyrrole, (b) cyclopentadiene, (c) 2,1,3-benzothiadiazole, (d) furan, (e) thiophene, (f) 1,2,5-thiadiazole, (g) 1,2-thiazole. The contribution from the HOMO to HOMO-7 orbitals in the ionization spectra are represented by coloured lines, while the rest is given in black.*

the aromaticity of the system. Note that the values calculated for aromaticity using the above methods also strongly depend on the level of the applied theory. I summarize the findings from this study below: (i) I reported that increase in delocalization of the electrons results in a red shift in the ionization potential for corresponding π-type orbitals. This shift in energy is valid in the weak correlation regime. (ii) Aromaticity was found to increase with the following variations of structures, tautomerization from keto form to enol form of **U**, **T**, **C** and **G**. The charge was highly delocalized and several resonant structures were identified. (iii) Rotational isomerization did not

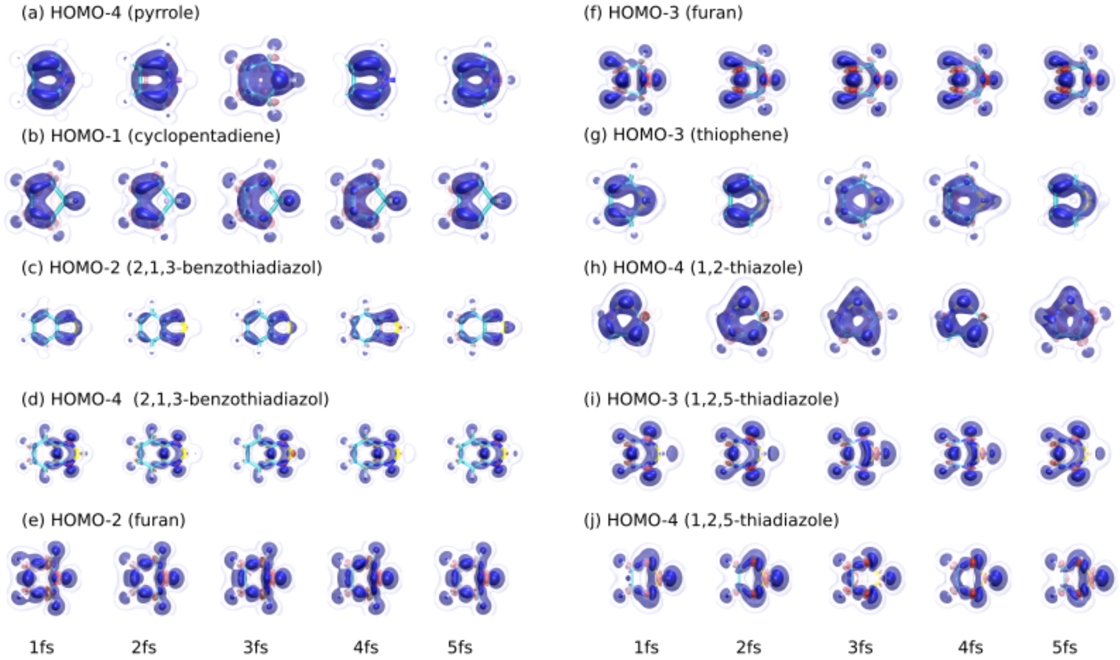
(a) HOMO-4 (pyrrole)
(b) HOMO-1 (cyclopentadiene)
(c) HOMO-2 (2,1,3-benzothiadiazol)
(d) HOMO-4 (2,1,3-benzothiadiazol)
(e) HOMO-2 (furan)
(f) HOMO-3 (furan)
(g) HOMO-3 (thiophene)
(h) HOMO-4 (1,2-thiazole)
(i) HOMO-3 (1,2,5-thiadiazole)
(j) HOMO-4 (1,2,5-thiadiazole)
1fs
2fs
3fs
4fs
5fs
1fs
2fs
3fs
4fs
5fs

Figure 5.13: *CMD in (a) HOMO-4 of pyrrole, (b) HOMO-1 of cyclopentadiene, (c-d) HOMO-2 and HOMO-4 of 2,1,3-benzothiadiazole, (e-f) HOMO-2 and HOMO-3 of furan, (g) HOMO-3 of thiophene, (h) HOMO-4 of 1,2-thiazole and (i-j) HOMO-3 and HOMO-4 of 1,2,5-thiadiazole; within 5 fs after the ionization of the corresponding molecular orbitals.*

show any strong effect on CMD for **C**. (iv) Isomerization from enol form to the imino-form, such as in case of **C** and **G**, lead to change in the delocalization of charge density, however it was less prominent in comparison to what I found after tautomerization from the keto- to enol form for **T**, **G** and **C**. (v) The charge in non-aromatic cyclopentadiene did not appear to delocalize outside the π-conjugated sites. (vi) We also propose CMD as an another method for analyzing the aromaticity for the other molecules representing π-spacers. (vii) Based on the electronegativity of the heteroatoms, difference in the connectivity between the π-electrons via double bonds and the lone pairs are explored in this chapter. (viii) The difference in the aromaticity between the two fused rings in heterocyclic molecules is also studied in this chapter. After investigating charge migration dynamics in the different tautomers and isomers of DNA nucleobases and in several cyclic molecules, it is striking to see that small variations in structure can lead to prominent differences in the response of a molecule to sudden ionization.

We hope that these results will motivate further studies based on more refined analytic tools, for example, Bader/QTAIM analysis [180] or Mulliken charges [181]. The study of charge migration dynamics can be another tool in addition to the one mentioned above to correlate charge density and the aromaticity of the molecules. This will provide significant help in molecular designing, as the selection of the groups to construct a large, extended system will be not based on trial and error, but rather on the electronegativity and aromaticity of the groups. Hence, I hope this work will come in handy for chemists and biologists in designing and remodelling the existing molecular systems.

Repeated oscillation of charge ("charge migration") in the molecule will result in electron-nuclei coupling and start the non-adiabatic dynamics beyond a few *fs*. In the next chapter, I investigated how this dynamics will vary with the number of vibrational modes involved in the coupled dynamics and how long the adiabatic dynamics will last.

Chapter 6

Non-adiabatic Dynamics

Charge migration dynamics presented in Chapter 4 and Chapter 5 is in between the *as* timescale and 10 *fs* range, and does not include the non-adiabatic effects. According to the famous Born-Oppenheimer approximation, the large mass of nucleus and slow motion compared to that for the electrons allows one to separate the motion of the electrons and nuclei. On the *as* to the *sub-fs* timescales, the adiabatic approximation is reasonable, as the created electron coherence lasts long enough[145]. Hence, the adiabatic approximation is accurate until one encounters a situation where the so-called conical intersection between the electronic energies exists. These intersections appear when the electron-nuclei dynamics couple and contribute to overall charge dynamics. For a polyatomic molecule with dense electronic states and several nuclear degrees of freedom, such intersections are rather usual. V. Despre et. al. studied the strong correlation-driven charge migration, and showed that coherence can last longer than 10 *fs* [145, 146]. On the contrary, if the system has only weak correlation effects, then the decoherence of the electronic wave packet created by the ionization of two or more MOs is observed within a few *fs*[182, 183]. The non-adiabatic dynamics for the uracil cation was studied by M. Assmann et. al. with the EOM-IP-CCSD and MCTDH methods[184]. They reported that a fast relaxation process is triggered after the excitation of the third or the fourth ionic states. In this chapter, I perform a similar study for the **U** cation, however I use the strongly correlated cationic states.

In this chapter I wanted to study the electron-nuclei coupling between the electronic and vibronic states that can possibly be excited when measuring charge migration dynamics experimentally. I studied the non-adiabatic dynamics by coupling the first twelve electronic states with the first ten vibrational modes of **U**. These states can be excited when a sub-*fs* or short pulse interacts with the molecule. Beyond the adiabatic approximation, the vibronic coupling phenomenon can be analyzed via diabatic electronic representation[185, 186, 187]. Within this representation, the diagonal terms are the vertical ionization energies for the electronic states, details are given in Sec. 6.2 below. The diabatic and adiabatic electronic states coincide at the Franck-Condon zone Q=0. From the potential energy surface I extracted the off-diagonal matrix elements, which represent the coupling between the different electronic states. Generally, the diabatic electronic functions are given in terms of nuclear coordinates and the matrix elements can be expanded into a Taylor series. Depending on the number of terms retained from the Taylor series expansion, first or second order terms, linear or quadratic vibronic coupling approaches are used[18, 188, 189]. With the help of the coupling parameters, the vibronic coupling Hamiltonian (VCH) is constructed and used to propagate the nuclear wave packet on the coupled manifold of the electronic states using the multiconfiguration time-dependent Hartree (MCTDH) method. Details for the modelling and construction of the vibronic coupling Hamiltonian along with the multiconfiguration time-dependent Hartree method are given in Chapter. 2.

6.1 Electronic structure calculations

In its ground state, the **U** molecule has C_s symmetry, and the electronic configuration is: (core)
$\times(9a')^2(10a')^2(11a')^2(12a')^2(13a')^2(14a')^2(15a')^2(16a')^2(17a')^2(18a')^2(19a')^2$
$\times(1a'')^2(20a')^2(21a')^2(22a')^2(2a'')^2(3a'')^2(23a')^2(24a')^2(4a'')^2(5a'')^2$.
The normal modes were calculated using the Møller-Plesset second order perturbation theory (MP2)[190] with the LANL2DZ[191] basis set[192].

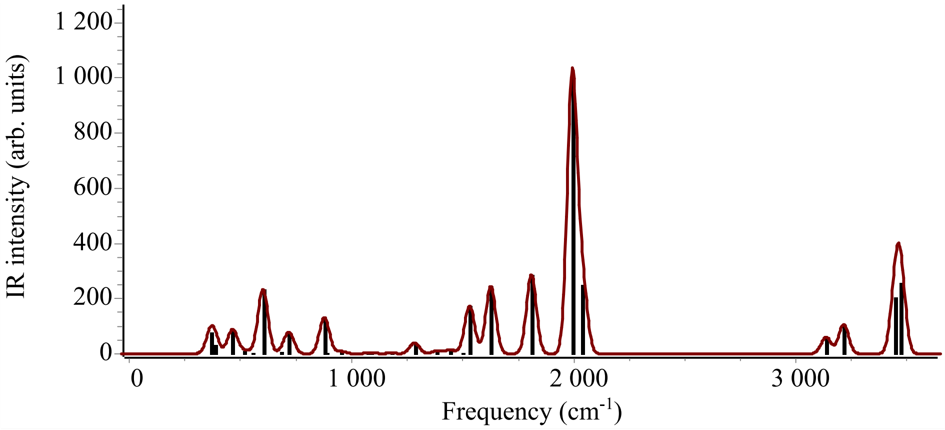

Figure 6.1: *Vibration spectra for the uracil molecule calculated with the MP2/LANL2DZ method.*

The vibrational spectra given in Fig. 6.1 show moderate vibrations between the 1^{st} and 10^{th} modes, while strong vibrations are observed between the 20^{th} and 26^{th} modes. The strength of the vibrational modes is determined by the intensity of the corresponding peaks in Fig. 6.1. As **U** has twelve atoms, in total it has thirty nuclear internal degrees of freedom. Twenty modes are in planar 10 represent out-of-plane motion (see Table.6.1). The symmetry and the energy of the vibrational modes is tabulated in Tab.6.1.

6.2 VCH and MCTDH

In the construction of the VCH we included the first twelve cationic states. These states can be easily ionized by a broadband ultrashort laser pulse. For each mode we generate dimensionless coordinates associated to the normal mode i, up to $2.5Q_i$ with a step of $0.5Q_i$. Potential energy surfaces (PES) are generated using the ionization potentials from the values extracted from the non-Dyson ADC(3) method and the cc-pVDZ basis set[136, 191] for each Q_i (see Fig. 6.2). The potential energy curves obtained from the ADC calculations and VCH are in good agreement with each other. All the coupling parameters used for the construction of VCH were extracted using the least-square fitting procedure. There is an intersection between the second and third PES, and the

Mode	Symmetry	Frequency (cm^{-1})	Mode	Symmetry	Frequency (cm^{-1})
1	a''	143.944	16	a''	1087.9227
2	a''	150.8083	17	a'	1178.1645
3	a''	367.6298	18	a'	1283.0161
4	a''	383.8389	19	a'	1381.9592
5	a'	463.7716	20	a'	1443.6986
6	a''	515.9806	21	a'	1500.9128
7	a'	552.7441	22	a'	1531.0245
8	a'	601.2941	23	a'	1625.9219
9	a'	603.2687	24	a'	1809.0531
10	a'	683.6006	25	a'	1992.5471
11	a''	718.3619	26	a'	2038.4801
12	a''	877.3214	27	a'	3134.889
13	a''	887.75	28	a'	3213.916
14	a'	953.8082	29	a'	3446.378
15	a'	1071.7987	30	a'	3470.4107

Table 6.1: *Frequency and symmetry for the normal modes of the* ***U*** *molecule.*

seventh and eighth PES. I used the MCTDH method to propagate the wave packet. All the details for the construction of the VCH, extraction of coupling parameters and the MCTDH method are given in Chapter 2.

I calculated and analyzed the PES for the twelve cationic states in the first 26 modes, from amongst which we present the PES along the following modes: ν_1, ν_5, ν_7, ν_9, ν_{13}, ν_{14}, ν_{15}, ν_{17}, ν_{18}, ν_{19}, ν_{20}, ν_{21} in Fig.6.2. The conical intersections between states 2 and 3; as well as between states 7 and 8 can be seen for most of the modes given in Fig.6.2. The single particle function (SPF) and primitive basis for the ten modes used to calculated the adiabatic population dynamics (see Fig.6.3) is given in Table.6.2.

Normal modes	SPF basis	Primitive basis
(ν_1,ν_2)	[6,6,6,6,6,6,6,6,6,6,6,6]	21,21
(ν_3,ν_4)	[6,6,6,6,6,6,6,6,6,6,6,6]	21,21
(ν_5,ν_6)	[6,6,6,6,6,6,6,6,6,6,6,6]	21,21
(ν_7, ν_8)	[6,6,6,6,6,6,6,6,6,6,6,6]	21,21
(ν_9, ν_{10})	[6,6,6,6,6,6,6,6,6,6,6,6]	21,21

Table 6.2: *Single-particle functions (SPF) and the number of primitive basis functions for modes 1 to 10 for the uracil cation.*

In our calculations we represented the selected nuclear degrees of freedom in the primitive basis of harmonic oscillator function. We choose the discrete variable representation (DVR) so that maximal population below 10^{-4} is ensured for the last grid point. The number of SPF is selected so that the maximum population of the highest natural orbital is lower than 10^{-3}. We used the neutral ground state for the creation of the initial wave packet of **U** with the first ten nuclear degrees of freedom. For the initial wave packet the normalized population (peak intensity) for the first twelve states is adapted from the calculated ionization spectra of keto-**U** (see Fig. 4.1(a)). In Fig.6.3(a-d) I present the results for the evolution of the wave packet created for the single modes

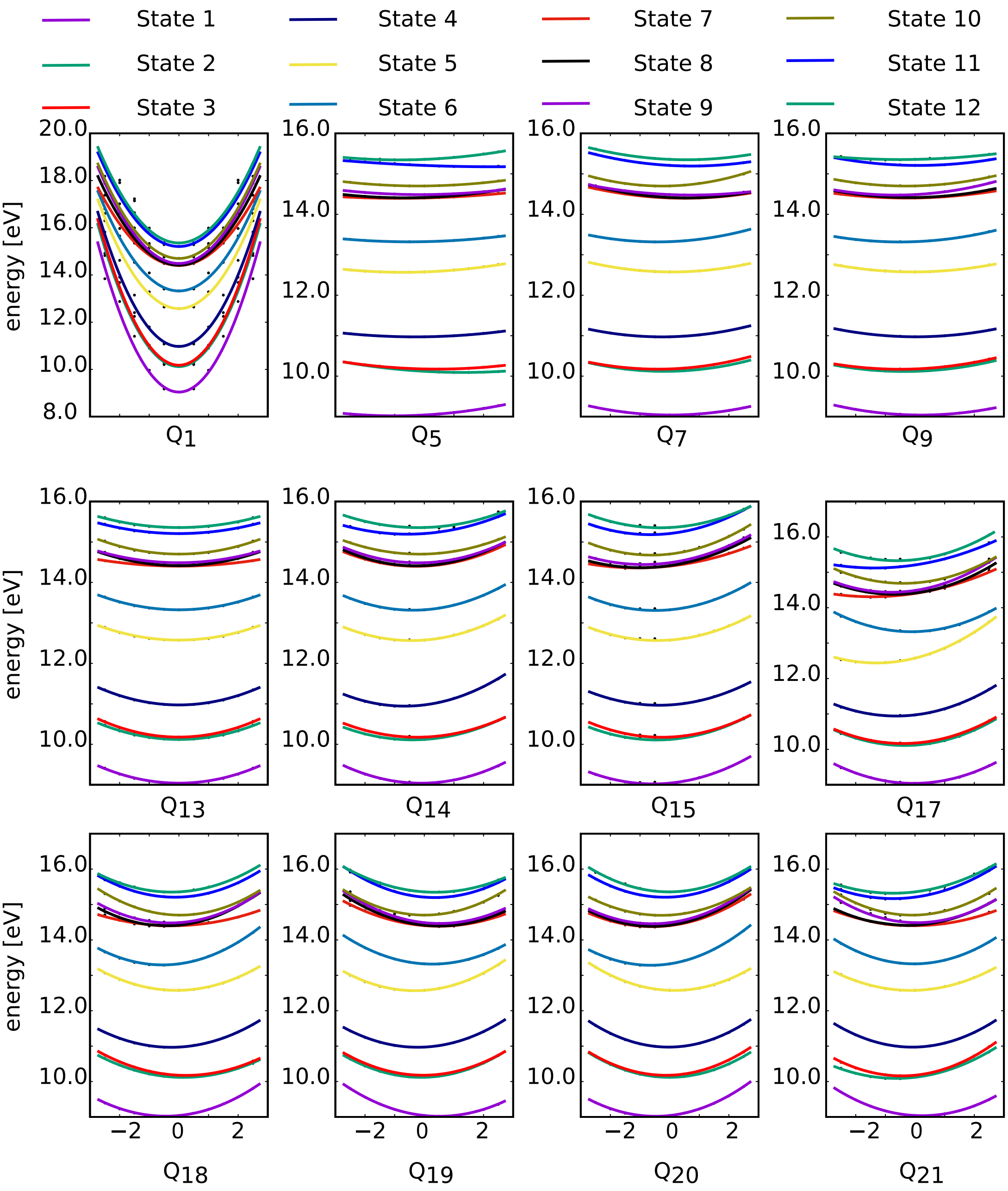

Figure 6.2: *Comparison of the individual single-point energy (dots: non-Dyson ADC(3) method) and potentials energy curves fitted with the adiabatic model (lines) for the normal coordinates of the selected vibrational modes.*

ν_1, ν_5, ν_7 and ν_9. Amongst these four modes, only ν_1 (a'') vibrates out of plane, while the rest shows vibrational motion in plane as they have a' symmetry. The non-adiabatic dynamics for electronic states coupled with the ν_1 shows dynamics and crossing between states 1 and 3. However, minimal population transfer is observed after $>$15 *fs* (see Fig.6.3(a)). The non-adiabatic dynamics

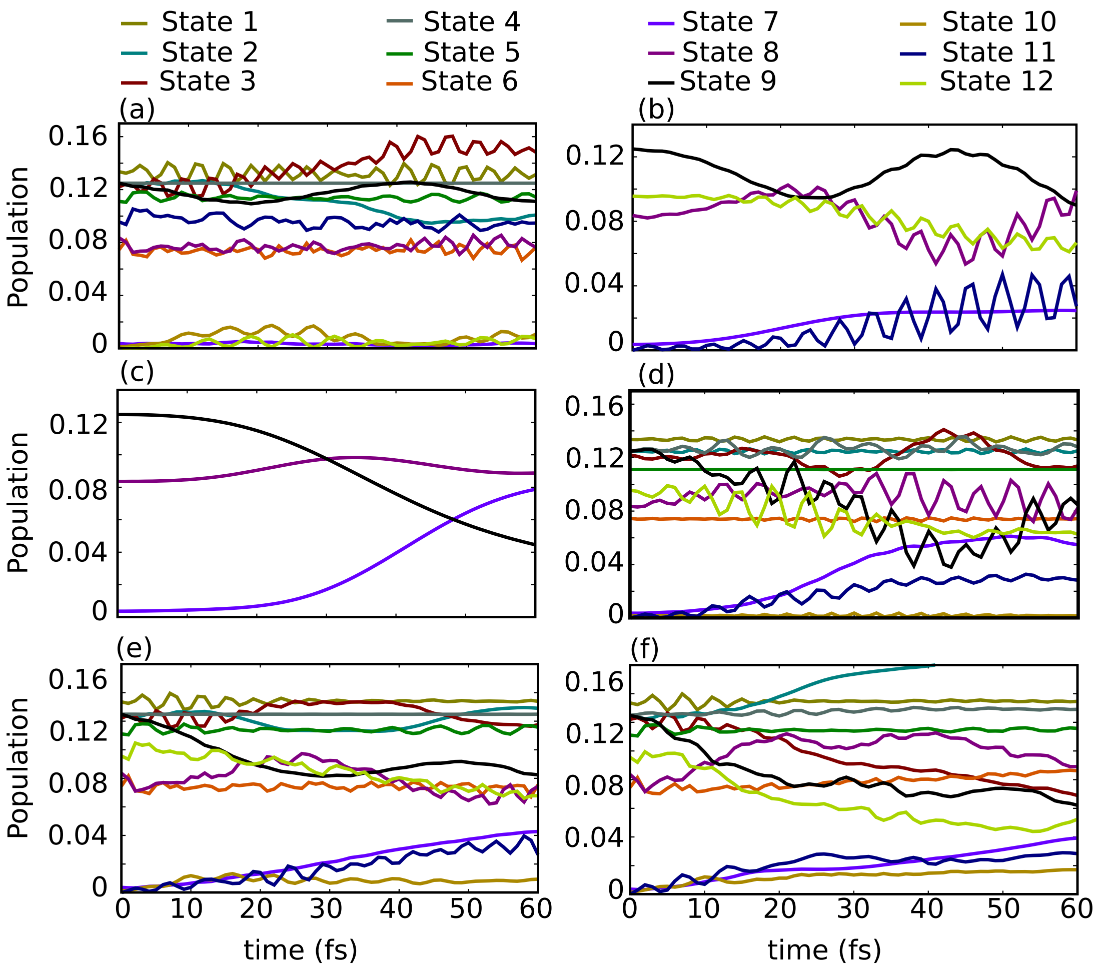

Figure 6.3: *The non-adiabatic state population dynamics for all twelve states of U^+. The first four panels show the population transfer in modes (a) ν_1, (b) ν_5, (c) ν_7 and (d) ν_9. (e) The dynamics with the combination of the ν_1, ν_5, and ν_7 modes. (f) The dynamics for the combination of ν_1 to ν_{10} modes.*

for the symmetric vibrational modes (ν_5, ν_7 and ν_9) show a large population transfer between the higher states (see Fig.6.3 (b-d)). For ν_5 and ν_7, the crossings between the states higher than state 6 is evident after $>$15 *fs*, while for ν_9 the crossings are seen after $>$15 *fs*. This implies that the when the twelve electronic states are coupled only with specific vibrational mode, the non-adiabatic dynamics started after 15 *fs*.

We further coupled three (ν_1, ν_5, and ν_7) and then ten (ν_1 to ν_{10}) vibrational modes, to observe the full non-adiabatic dynamics. Fig.6.3(e) presents the results for non-adiabatic dynamics for three coupled modes ν_1, ν_5, and ν_7 (3-dimensional, 3D), while in Fig.6.3 (f) the results for the ten modes from ν_1 to ν_{10} (10-dimensional, 10D). In the 3D picture we see the oscillation and decoherence of the population between states 2 and 3; and states higher than state 7. The population decreases in state 12 and increases in state 7 (see Fig.6.3 (e)), while the crossing between the state is observed after 10 *fs*. When we coupled the first ten modes, the population decreased for states

3, 9 and 12, and increased for states 2, 7, 8, and 11 during the first 60 *fs*. This shows strongly coupled non-adiabatic dynamics for the 10D system, which leads to crossing between the states after 10 *fs* (see Fig.6.3 (f)). This implies that when the twelve cationic states couple with more and more vibrational modes are involved in the dynamics, they become faster and many states couple for population transfer between states.

Summary and conclusions

In this chapter I studied the vibrational spectra of the uracil molecule in its ground state to identify the symmetry and strength of the vibrational modes. I found that amongst the 30 vibrational modes (30 = 3N-6, with N = 12 atoms), 20 show in-plane motion and 10 show out-of-plane motion based on symmetry of modes. Based on the peak intensity, the first ten vibrational modes show moderate vibrational strength, whereas the vibrational modes 20^{th} and beyond show stronger vibrational strength. To the construct the vibronic coupled Hamiltonian I used the energy for the first twelve cationic states and first ten vibrational modes. Additionally, I fitted the potential energy surfaces for the first 26 vibrational modes using the least square fitting method, and extracted the coupling constants up to quadratic order. I then used the MCTDH method to propagate the electron-nuclei coupled system for the first 10 modes; I presented and investigated the results for mode 1, mode 5, mode 7 and mode 9 separately. Furthermore, I constructed the 3D and 10D modelled systems with mode 1, mode 5, and mode 7; and the first ten modes, respectively. Through these calculations I found the onset of non-adiabatic dynamics for the 1D system (electron-nuclei coupling with single mode) is after 15 *fs* and typically electronic states higher than state 6 contributed in population transfer. For the 3D and 10D model case the population transfer takes place after 10 *fs* and even lower states are involved in prominent population transfer. Furthermore I report that the decoherence between the cationic states for the 10D modelled system is faster in comparison to the 3D modelled system. Hence, from this study I conclude that when more vibrational modes are involved the electron-nuclei coupling is stronger and the population transfer between the electronic states is faster. To successfully capture the charge migration dynamics and/or the non-adiabatic dynamics experimentally the signal to noise ratio has to be high. This can be achieved using laser-induced alignment of molecules. In the next chapter I present the results for such dynamics with varying experimentally feasible laser parameters.

Chapter 7

Laser-Induced Alignment Dynamics

Up to this point in the thesis I have presented the results for photo-induced charge transfer and charge migration dynamics. It is not trivial to measure such dynamics through experimental studies. These experiments need considerable theoretical backing to choose the laser parameters, to align the system, to initial the charge dynamics and to capture such dynamics. The output of such experiments is usually lost in noise, and the key to get a better signal to noise ratio is the alignment of the molecules with respect to the laser field[147, 193]. Although the study of molecular alignment and orientation is important here, it is not limited to the study of charge migration dynamics. Such investigation can also be helpful in the several areas of ultrafast science, high harmonic generation[194, 195], photo-chemical reactions, strong-field physics[196], molecular imaging[197], attosecond pulse shaping[198], to name a few[199].

Several earlier studies reported laser-induced alignment and orientation[200, 201, 202]. They investigated how to understand and control the alignment dynamics of a molecule by varying the pulse parameters such as, pulse duration[193, 203, 204], intensity[205, 206], carrier envelope phase, and frequency for a single and two-colour pulses[207]. However, to the best of our knowledge, alignment studied on varying pulse parameters and identifying two different behaviours in alignment dynamics has not been reported. For this study we choose the CH_3F molecule. Due to its size and symmetric top structure (C_{3v}), the system has been considered for several theoretical and experimental benchmark studies [208, 209]. Through the alignment dynamics in CH_3F we identify the two different types of behaviours and understand the connection between revivals and the excitation pattern of the rotational states. This study includes experimentally feasible pulse and temperature parameters. The type of laser pulse used for this study belongs to the optical [210, 211] regime. For these studies I have used the tuning parameters available at ELI ALPS laser user facility (summarized in Table. 7.1). Note that all figures, results and discussions presented in this chapter are adapted with permission from Ref.[212], Copyright © (2022), Kalyani Chordiya et al.

Parameters at the laser output	Tuning range[210, 211]
Peak power (800 *nm*)	0.1 - 100 TW/cm^2
Full width half maxima (800 *nm*)	12 - 200 *fs*

Table 7.1: *The tunable range of the experimentally feasible pulse parameters for 800 nm*

.

7.1 Computational method

For CH_3F, the molecular parameters were calculated with high level coupled cluster theory, where we considered single, double, and perturbative triple excitations CCSD(T)[213, 214, 215] and the aug-cc-pVDZ basis set[136]. These quantum chemistry calculations were performed using the ORCA 4.1 package[101, 102]. The alignment dynamics for CH_3F under the influence of an 800 *nm* pulse were calculated using the LIMAO package[67], which solves the time-dependent Schrödinger equation under rigid rotor approximation. In these calculations we neglect the vibrational and electronic excitations and special precautions are taken when assigning the laser intensity to keep it below the ionization threshold. In this chapter I will discuss the pure rotational dynamics and how it can be tunes with varying laser pulse parameters.

7.2 Results and discussions

The detailed theoretical description and simulation method used for these calculations are given in Chapter 2. CH_3F has rotational constants: $B_z(A) > B_y(B) = B_x(C)$, therefore it is a prolate symmetric top molecule. The calculated values for (experimental) the rotational constants are B_x = B_y = 0.829 cm^{-1} (0.852 cm^{-1}[216]) and B_z = 5.089 cm^{-1} (5.182 cm^{-1}[216]), polarizability are $\alpha_{\|}$ = 2.524 Å^3 and $\alpha_{\perp}$ = 2.296 Å^3, and dipole moment (μ_z) = 1.894 D (1.850 D[217]). The rotational eigenfunctions for this molecule transform as the irreducible representations (irreps) of D_{∞}. [68]. For each of the irreps, the calculated nuclear spin statistical weights [68] (NSSW) are as follows: NSSW$^{\Sigma^+}$ = 2, NSSW$^{\Sigma^-}$ = 2, NSSW^{E_1} = 1, NSSW^{E_2} = 1, and NSSW^{E_3} = 2. I studied the temperature dependence of the alignment dynamics, followed by the dependence on the varying optical pulse parameters such as pulse duration and intensity.

Figure 7.1	FWHM (*fs*)	Intensity (TW/cm^2)	Temperature (*K*)
(a,d) Temperature	100	100	0 to 300*
(b,e) FWHM	10 to 700*	100	2
(c,f) Intensity	100	1 to 100*	2

Table 7.2: *The alignment dynamics presented in Fig. 7.1 with varying ("*") 800 nm pulse parameters. Here we vary the marked parameter keeping the others fixed during the simulations.*

During the alignment dynamics, gas molecules are assumed to be in a thermal ensemble at a rotational temperature T. Using the nuclear spin statistical weight and the Boltzmann distribution, I calculated the initial distribution of the rotational levels[68]. When such an ensemble interacts with a laser pulse, the temporal rotational evolution can be explained as the weighted averaged of the initial rotational states for the rotational wave packets. Hence, as the temperature increases (for the T range see Table 7.2), more rotational states are excited and the maximum degree of alignment ($\langle\cos^2(\theta)\rangle$) decreases as given in Fig. 7.1(a). At a lower T, the contribution from the higher energy rotational states is negligible and therefore, the highest degree of alignment could be achieved at 0 *K*.

The variations in the rotational revivals with temperature are presented in Fig. 7.1(a) with the corresponding maximal $\langle\cos^2(\theta)\rangle$ in Fig. 7.1(d). As the pulse hits the molecules, the rotational revivals are observed at every half and full revival period (τ_{rev}). The value for tau can be calculated

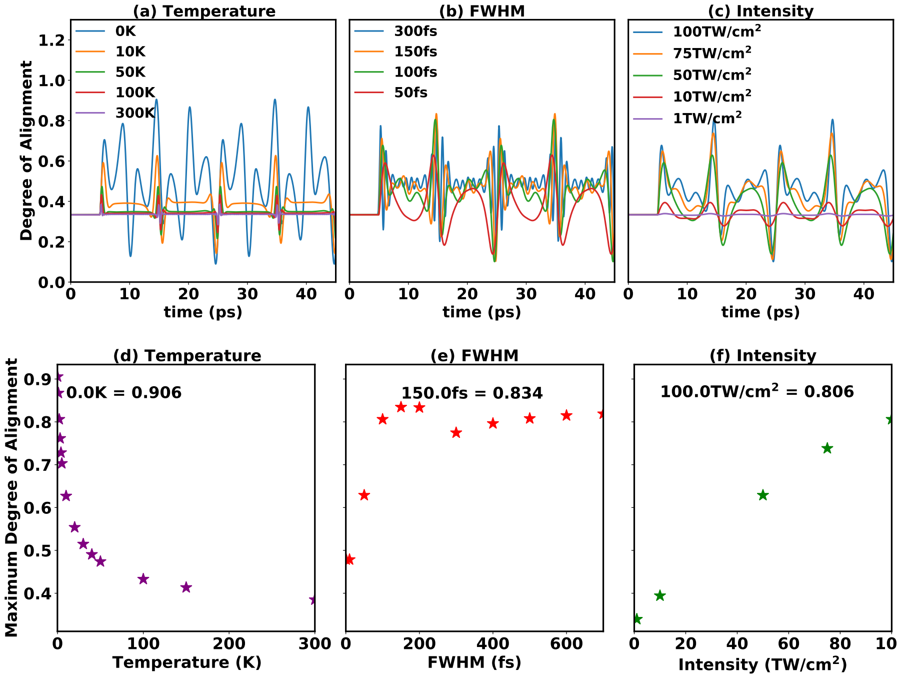

Figure 7.1: *Alignment dynamics with varying (a) Temperature, (b) FWHM and (c) Intensity. The maximum value for alignment during each variation is given in: (d) Temperature, (e) FWHM and (f) The range of the varying parameters for an 800 nm pulse are given in Table. 7.2 and the laser pulse is at 5 ps.*

using the rotational constants for the symmetric top molecules, $\tau_{\text{rev}} = 1/(2B_x c) = 1/(2B_y c) = 20\,ps$ (c is the speed of light). As mentioned earlier, the maximum alignment will be at $0\ K$ with $\langle\cos^2(\theta)\rangle$ = 0.906 and it will keep decreasing with $T = 2\,K$ $\langle\cos^2(\theta)\rangle$ = 0.8, $T = 20\,K$ $\langle\cos^2(\theta)\rangle \simeq$ (Fig. 7.1(a and d)). From the population distribution heatmap summed over K, for $T = 0\ K$ only even J states are excited and $|2, K, 0\rangle$ is the highest populated state. As T increases, higher rotational J, M states are excited. The highest populated state at 10 K is $|J = 2, K, M = 0\rangle$ = 0.051, while for $100\ K$ it is $|J = 3, K, M = 0\rangle$ = 0.008. The rotational revivals for all the temperatures show that distinct revivals are well separated by plateaus; we call this behaviour of the revival curve as "conventional revival" in this thesis. With the current advancements in experimental techniques for the cryogenic cooling of the systems, temperatures as low as $1\ K$ have been reported [218, 219]. Hence, with the experimentally feasible parameters I present the results for the rest of the varying parameters keeping the temperature at $2\ K$.

I vary the pulse duration by changing the value of full width at half maximum (FWHM) for an 800 *nm* laser pulse from 10 *fs* to 700 *fs*. We observe conventional revivals for FWHM = 50 *fs* and the excitation of a few states through the population distribution in the heatmaps (see Fig. 7.1(b) and Fig. 7.2). As we increase the pulse duration, quarter revivals (revival at $\tau_{1/4}$) are observed. This behaviour of the rotational revivals is observed for 100 *fs* and 150 *fs* pulse durations. However, after further increasing the pulse duration (FWHM>300 *fs*), the alignment revivals manifest unconventional or anomalous behaviour. In the unconventional behaviour the oscillations are observed in the plateau regions (see Fig. 7.1(b)). The maximum alignment increases with the FWHM

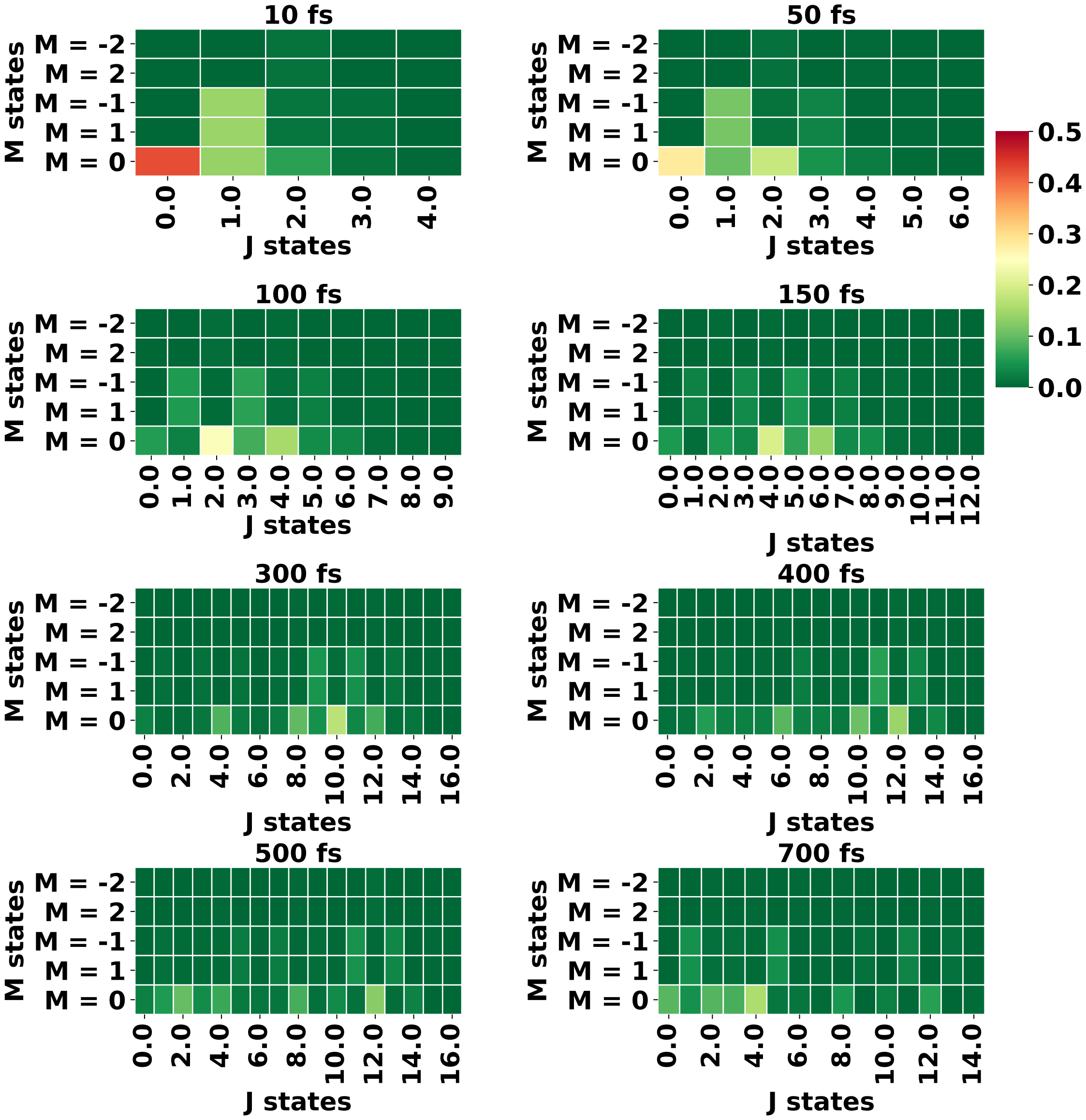

Figure 7.2: *Rotational states excited after varying the pulse duration for an 800 nm pulse. Other pulse parameters are given in Table. 7.2*

(see Fig. 7.1(e)) from FWHM=10 *fs* to FWHM= 150 *fs* with the highest $\langle\cos^2(\theta)\rangle = 0.834$ for FWHM=150 *fs*. A slight decrease in the maximum degree of alignment ($\langle\cos^2(\theta)\rangle_{max}$) is observed for 300 *fs*, and a further increase in FWHM shows an increase in $\langle\cos^2(\theta)\rangle_{max}$. The population distribution and the time-dependent population analysis shows that more J states are populated due to longer pulse durations. However, these pulse durations also favour the de-excitation process and results in the broad distribution of the J states for a given wave packet. The change in excitation and de-excitation also supports the drop in $\langle\cos^2(\theta)\rangle_{max}$.

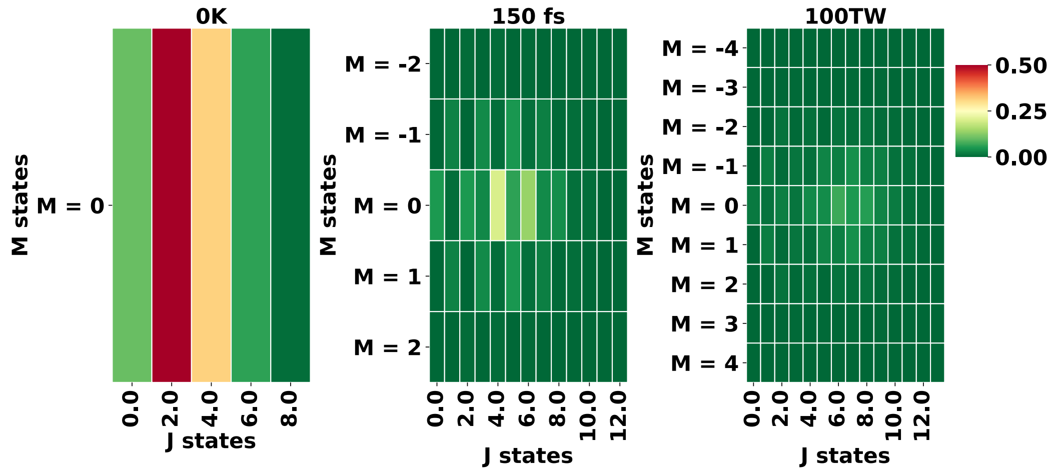

Figure 7.3: *For the highest achieved alignment presented in Fig. 7.1 the population of the rotational states* $|J, M\rangle$ *are given: (a) temperature of 0 K (b) 150 fs FWHM and (c) Intensity of 100* TW/cm^2.

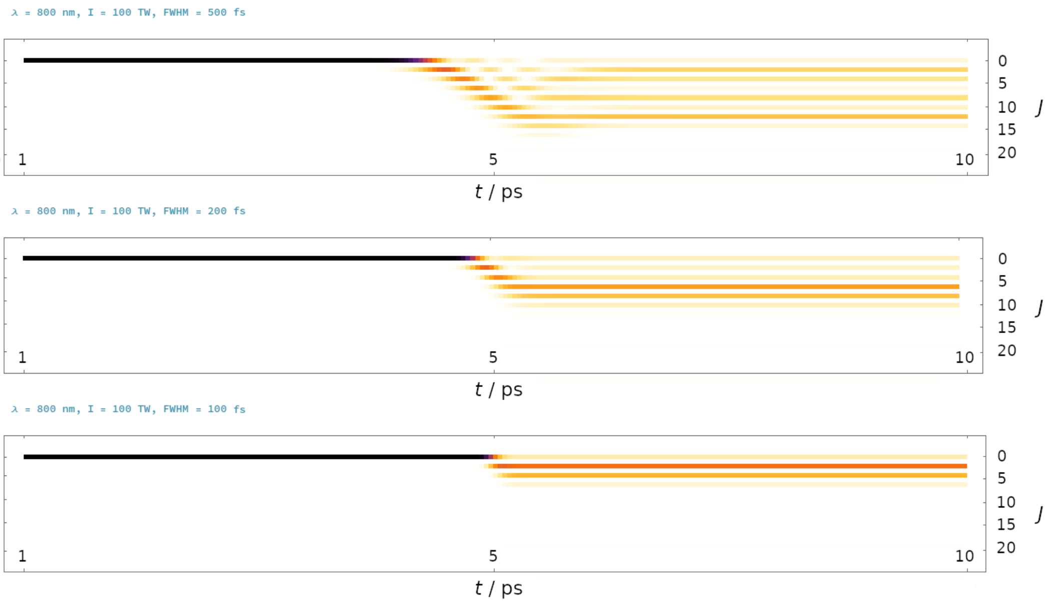

Figure 7.4: *Temporal population distribution for different* J *states* ($\sum_K |C_{J,K,M=0}(t)|^2$) *for FWHM = 500 fs, 200 fs and 100 fs (going from top to bottom). The centre of the pulse is at 5 ps.*

Advanced laser technology offers a wide range of intensity. If the alignment molecules are used to further strong-field physics or photo-chemical interaction studies, then it might be helpful to keep the intensity of the alignment laser below the ionization threshold. This can be determined by calculating the Keldysh parameter (γ) [220]. Depending on the value of γ, the ionization regime will be classified. The relation between γ and the ionization potential (I_p =12.5eV) [221] is $\gamma = \sqrt{\frac{I_p}{2\times U_p}}, U_p = 9.337 \times 10^{-5} \times I \times \lambda^2$. The term U_p in the above relation is the pondermotive energy of the laser field[221]. For an 800 *nm* pulse with an intensity of 100 TW/cm^2, the Keldysh parameter is calculated as 1.023, which lies in the transition regime [222]. Increasing I beyond 100 TW/cm^2 will give γ <1, leading to tunnel ionization. Hence, for the alignment dependence on intensity I use the maximum value of I =100 TW/cm^2 [147].

I present the results for alignment dependence on laser intensity in Fig. 7.1(c and f). Here $\langle\cos^2(\theta)\rangle_{max}$ increases linearly with the value of I. Using a similar analysis as presented earlier for varying FWHM, I can see a similar increase in the number of excited rotational states with the value of I. On increasing the I from 1 TW/cm^2 to 10 TW/cm^2, the revival pattern remains normal and so does the number of rotational states excited(see Fig. 7.1(c and f)). However, the $\langle\cos^2(\theta)\rangle_{max}$ for 10 TW/cm^2 is higher than for 1 TW/cm^2 and the same trend is also reflected in the population of the states excited in the two case. The population density of the states excited with 10 TW/cm^2 is higher than for 1 TW/cm^2. We observe abnormal behaviour in the revival curves with increase in I from 10 TW/cm^2 to 50 TW/cm^2, and the excited states show population of higher J states. After a further increase in I from 75 TW/cm^2 to 100 TW/cm^2 the population of the lower excited J states (<4) transfers to higher J states (J = [4 to 7]). Such a transition results in the abnormal behaviour of the alignment curve. For a single 800 *nm* (optical pulse) the molecular rotational period is longer than the field oscillation period. Due to this, the interaction term with the dipole moment vanishes from the Hamiltonian in the TDSE. Hence, using a single optical pulse one can achieve only molecular alignment, but not the orientation. Using a single THz pulse or a two-colour pulse, one can study laser induced orientation dynamics[223]. This is possible as these pulses can trigger light-matter interaction with the permanent dipole and/or hyperpolarizability of molecules.[223]. We have presented our results on the use of THz pulse to study alignment and orientation dynamics in the CH_3X molecule in the Ref.[212, 224].

7.3 Summary and conclusions

In this chapter I presented the results for the laser-induced alignment dynamics of the CH_3F molecule using a non-resonant 800 *nm* pulse. I presented a detailed study on the relation between the laser pulse parameters and the excited rotational states. Such an interplay lets us observe two different types of alignment curve behaviours. When the alignment curve manifested normal behaviour, the population distribution was over a few rotational states. In case of anomalous behaviour, several oscillations appeared between half and full revivals. The reason behind the anomaly was the distribution of the excited states either over a large number of J states or their localization to a few higher states (large M value). I report the maximum alignment of $\langle\cos^2(\theta)\rangle_{max}$=0.834, when an 800 *nm* pulse with FWHM = 150 *fs* and I= 100 TW/cm^2 is used. The information presented in this chapter can be used by experimentalists to study strong field physics for CH_3F using the alignment pulse parameters given here and in our published works[212, 224]. This study can also be used for complicated heteronuclear molecules. Furthermore this can help us understand role of rotational states in laser-matter interactions and may facilitate the advancement of ultrafast reaction dynamics or high harmonic generation.

Chapter 8

Summary and Outlook

Recently organic structures have started to be used in several highly efficient and flexible opto-electronic solar cell and sensors devices, and they have also found application in tumour detection and radiation therapy. The organic compounds mainly play a role in charge and energy transfer in these devices. These molecules are typically large extended systems with a push-pull structure, where the photo-induced charge is transferred from the donor group to the acceptor group. For the efficient modelling of these large molecules it is crucial to understand charge dynamics in small groups used in molecular design. This understanding will aid in selecting, or modifying the groups, and in finding efficient ways to assemble different groups for effective charge transfer. In this thesis I have tried to answer the following questions to help molecular modelling: How can linear response calculations be used to study the charge transfer process in large molecules? Does the correlation effect play an important role in charge migration dynamics (CMD)? How long does a molecule take to respond to the triggered dynamics and can this be tuned by the tautomerism or isomerization of molecules? Does the incoherent CMD mask the dynamics in different tautomers? How long is it before the non-adiabatic dynamic processes start and can they vary with the vibrational degrees of freedom involved in electron-nuclei coupling? What are the important things to consider before measuring these dynamics experimentally? I summarize below the key points of this thesis answering the above questions.

1. Typically, in a large extended molecule the charge transfer process occurs through the π-conjugated structure. When designing these molecules, it is important to make sure that the charge is indeed transferred from the donor to the acceptor group and is not trapped by a π-spacer. It can be computationally and experimentally expensive to determine such a charge transfer. Hence, I proposed a novel way to analyze the charge transfer efficiency using static linear response method. I interpreted the charge transfer in the molecule by studying the modification in a molecular structure after photo-excitation and ionization to the cationic state, with respect to its ground state. This method is useful to perform cost-effective calculations for analyzing the molecules before their experimental synthesis. The use of structural modifications has been reported in literature to interpret the charge transfer in molecules, however only in one of the above mentioned states. I studied the modified structure for a molecule in both states. This approach was reported for the first time (to the best of our knowledge) in the paper we published in [T1][73] and Chapter 3 of this thesis.

2. As mentioned earlier, the above method facilitates our understanding of the push-pull systems already used for photovoltaic or optoelectronic applications. However, studying the charge migration dynamics in the building blocks will help extensively in designing molecules. In Chapter 4 I studied the charge migration dynamics triggered by the sudden ionization of molecules like uracil. The response of the different molecular orbitals to such ionization is evaluated and investigated with the correlation effect. For a molecule with C_s symmetry, I found that the symmetric orbitals have similar response times, while the asymmetric molecular orbitals take longer to respond to sudden ionization. The response time of the asymmetric orbitals increases with the strength of the correlation effect. The response times by different orbitals in keto-uracil can be reduced by conversion to the enol-form via tautomerization. In enol-uracil the reduced response time is related to the greater delocalization of charge over the entire system in comparison to the keto-uracil molecule. In an experimental scenario a short attosecond pulse can ionize a broadband of cationic states. Hence, we developed a method with which we can study incoherent charge migration dynamics. During this investigation, we concluded that the difference in charge migration between the keto-enol tautomers of uracil remains even after incoherent ionization. The results for *as* and sub-*fs* charge migration dynamics were reported in [T2 and T3][130, 131], respectively and summarized in Chapter 4.

3. The visualization of charge migration dynamics will help massively not only in molecular modelling, but also in understanding the radiation damage in biological systems. I studied several different systems such as thymine, cytosine, and guanine to confirm our observations for the role of tautomeric hydrogen and molecular symmetries in charge migration dynamics in keto-enol tautomers from the above aspects. Apart from keto-enol tautomerization, bio-relevant molecules undergo enol-imino tautomerization, e.g. in case of guanine and cytosine; and rotational isomerization to produce cis-trans forms. Hence, by studying these variations and their effect on charge migration dynamics we can provide more support to chemists and biologists attempting to explain many unknown aspects in a larger system. Based on our analysis we conclude, that transformation from the keto to the enol-form or the enol- to the imino-form, leads to more charge delocalization, while cis- to trans- isomerization has a less prominent effect on charge migration dynamics.

CMD carry the imprints of aromaticity, electronegativity, electron-affinity, stereo-selectivity, etc. and therefore it can be suitably utilized to model an efficient push-pull system. Hence, we carefully scrutinized the CMD in the π-spacer groups used in designing push-pull systems. By visualizing the hole density on these groups we were are able to shed some light on the old but still not completely understood topic of aromaticity. For a molecule with a single ring, aromaticity is not that difficult to evaluate. However, things get complicated when a molecule has two or more fused rings, as in case of adenine, guanine or 2,1,3-benzothiadiazole. The difference in CMD can be correlated with the aromaticity of the single ring or the fused ring molecules. We conclude, that through CMD one can identify the sites where the charge oscillates, as well as electron-withdrawing and donating properties; this can aid in shortlisting the groups and order them for an effective charge transfer. The results from this study are summarized in Chapter 5.

4. After photo-ionization, the sub-*fs* charge oscillation between the atomic sites in the molecule leads to electron-nuclei coupled non-adiabatic dynamics. When studying this non-adiabatic dynamics in keto-uracil, the electronic states and the vibrational modes of the molecule are taken into account. During experiments, an ultrashort pulse can excite cationic states below 15 eV and

several low level vibrational modes. To study this situation theoretically I modelled the vibronic coupling Hamiltonian by coupling the vibrational mode 1 (ν_1) to mode 10 (ν_{10}) with the first 12 cationic states from ionization spectra. I plotted the potential energy surface cuts for all modes with weak to strong vibrations and fitted them to extract the non-adiabatic coupling constants required for constructing the vibronic coupling Hamiltonian. To get a preliminary understanding of the onset of non-adiabatic dynamics, I propagated the excited wavepacket using the multiconfiguration time-dependent Hartree (MCTDH) method. I report that the non-adiabatic dynamics for the first twelve states coupled with only one vibrational mode starts after 15 *fs*, while when coupled with more vibrational modes, the electron-nuclei coupling becomes stronger and more electronic states participate in population transfer. Furthermore, this results in faster non-adiabatic dynamics. The results for the non-adiabatic dynamics in uracil cation are given in Chapter 6 in this thesis.

5. The study of charge migration dynamics using advanced experimental methods requires highly aligned molecules. To study and control the alignment of the molecules under a laser field we need to understand the role of the rotational states in laser-induced molecular alignment and orientation dynamics. In Chapter 7, using a prototype system, CH_3F, I studied the population variation of the rotational states by tuning experimentally feasible laser pulse parameters. In this work I observed two different types of alignment behaviours which were termed as conventional and unconventional revivals. These two types of behaviour are correlated with the nature of the rotational states excited by the selected laser parameters. Hence, I reported the importance and ways to tune the rotational states to enhance the laser-induced alignment of the molecules in our published article [T4][212] and Chapter 7.

The main emphasis of this doctoral thesis is to gain atomistic level understanding of the photo-induced charge migration and charge transfer processes in extended molecular systems. Such ultrafast responses govern the photophysical and photochemical processes of the molecules and solid-state materials. Hence, the overall results of this thesis can be used by chemists in molecular designing, and by biologists in understanding the effect of radiation therapy on the nucleobases. Several interesting works have already been published in related topics, however there still remain a few gaps that need to be addressed. Using suitable and optimized computation and analysis methods presented in this thesis, it is possible to explain charge hopping, isomerization or fragmentation of nucleobases in DNA by comparing pre- and post-ionization conditions, or why and how the efficiency of the dye molecules vary upon shuffling the position of the π-spacer group[225]. I explain how the microscopic features obtained by the atomic-level simulations can be correlated to the macroscopic level responses of the molecules captured experimentally. The calculation of the exact time and direction of charge migration as presented in this thesis can be used to tailor and design extended molecules with improved and desired features. One can further utilize this study for evaluating the molecules to increase the interfacial charge dynamics, stability, efficiency and lifetime of perovskite materials[226, 227, 228]. This study can be extended to understand the influence of solvent or intermolecular interactions[229, 230] on the charge migration dynamics and the nonlinear optical properties such as high harmonic spectra[231]. Hence, we hope our results will encourage and inspire further research in the direction of molecular modelling.

Chapter 9

Magyar nyelvű összefoglaló

Az utóbbi időkben szerves molekulák felhasználásával nagy hatásfokú és flexibilis optoelektronikai napelem cellák és szenzorok váltak elérhetővé. Ilyen molekulák a tumordetektáláshoz és sugárkezeléshez használt eszközökben is alkalmazhatók, ahol leginkább a töltés- és energiaátadásban játszanak szerepet. E molekulák általában nagyméretű, push-pull szerkezettel rendelkező rendszerek, ahol a foton által előidézett töltés a donor csoportról az akceptor (fogadó) csoportra adódik át. Hatékony modellezésük érdekében elengedhetetlen a töltésdinamika megértése a molekulák tervezése során használt kisebb csoportoknál. E tulajdonságok ismerete segít a csoportok kiválasztásában, módosításában, és a legjobb töltésátadást biztosító csoportok hatékony kialakításában. Disszertációmban igyekszem választ adni a molekulamodellezésnél felmerülő számos kérdésre: Hogyan lehet statikus számításokkal tanulmányozni a töltésátadási folyamatot nagy molekulákban? Fontos szerepet játszik-e a töltésmigrációs dinamikában (CMD) a korrelációs effektus? Mennyi időt vesz igénybe a molekula válasza egy kiváltó folyamatra és lehet-e ezt tautomériával vagy izomériával hangolni? Elfedi-e ez az inkoherens CMD a különböző tautomerek dinamikáját? Mennyi időbe telik a nem-adiabatikus dinamikai folyamat elindulása, és befolyásolható-e ez az idő az elektron-atommag csatolásban részt vevő rezgési szabadsági fokokkal? E dinamikai folyamatok kísérleti mérése előtt mely fontos paramétereket szükséges figyelembe venni? A kérdések megválaszolásához doktori munkámat az alábbi pontokban foglaltam össze:

1. A kiterjedt nagy molekulákban a töltésátadási folyamat általában a π-konjugált struktúrán keresztül játszódik le. Ilyen molekulák tervezése esetén fontos megbizonyosodni arról, hogy a töltés valóban a donortól az akceptor csoportba adódik át, és nem csapdázódik egy π-távolságtartó (spacer) csoportban. E töltésátadási folyamat megállapítása mind kísérleti, mind szimulációs úton rendkívül erőforrásigényes feladat. A molekulán belüli töltésátadás értelmezéséhez foton által gerjesztett és kationos állapotba helyezett molekulaszerkezet változását tanulmányoztam az alapállapothoz viszonyítva. E módszer alkalmas a kevésbé erőforrásigényes számítások elvégzésére, így a molekulák kísérleti szintetizálás előtti elemzéséhez. A molekulákban történő töltésátadás értelmezése céljából előidézett, molekulaszintű strukturális változásokról már több cikk is megjelent, de a korábbi közlemények csak az egyik fent említett állapotra koncentráltak. Dolgozatomban mindkét állapotban tanulmányoztam a molekulaszerkezetet. Ez a megközelítés (legjobb tudomásunk szerint) először került közlésre cikkünkben[T1] és e dolgozat 3. fejezetében.

2. Ahogyan már korábban említettem, a fenti módszer megkönnyíti a fotovoltaikus és op-

toelektronikus területeken már alkalmazott push-pull rendszerek megértését, ám a rendszertervezés során különösen fontos a részegységek töltésmigrációs dinamikájának tanulmányozása. A 4. fejezetben az azonnali ionizáció által kiváltott töltésmigrációs dinamikát vizsgáltam molekulákban, például uracilban. Az ilyen ionizációs folyamatra a különböző molekulapályák által adott válasz elemzése és vizsgálata korrelációs effektus segítségével történik. A C_s szimmetriával rendelkező molekulákra azt állapítottam meg, hogy a szimmetrikus molekulapályák hasonló válaszidővel rendelkeznek, de az aszimmetrikus pályák esetén az azonnali ionizációra adott válasz hosszabb időt vesz igénybe. Az aszimmetrikus pályák esetén a válaszidő a korrelációs effektus erősségével nő. A válaszidők csökkenthetők a keto-uracil molekula enol-uracil molekulává való módosításával tautomerizációs folyamaton keresztül. Enol-uracil esetén a válaszidő rövidebb, hiszen a töltés nagyobb delokalizációval rendelkezik az ionizációt követően. Az attoszekundumos időtartamú válasszal kapcsolatos eredmények a [T2 és T3][130, 131]-ben kerültek közlésre valamint valamint a dolgozat 4. fejezetében is megtalálhatók.

3. A töltésmigráció dinamikájának vizualizációja nemcsak a molekulatervezést, hanem biológiai rendszerek sugárzás okozta károsodásainak megértését is segíti. Különböző molekulákat (timint, citozint és guanint) tanulmányoztam annak tisztázására, hogy milyen szerepet játszik a tautomerizációs folyamatban részt vevő hidrogén a töltésmigráció dinamikájában. A keto-enol formán kívül a biológiai alkalmazásokban jelenlévő molekulák enol-imino (például guanin és citozin) valamint cisz és transz formában is léteznek. Így e tautomerek és a töltésmigrációs dinamikára való hatásuk tanulmányozása a vegyészeket és biológusokat is segítheti a nagyobb molekulák tulajdonságainak megértésében. Vizsgálataink azt mutatják, hogy a keto és enol forma vagy az enol és imno forma közötti transzformáció több, míg a ciszről a transz izomerizációra való átalakulás kevesebb töltés-delokalizációhoz vezet. A töltésmigrációs dinamikában megjelennek olyan tulajdonságok, mint aromaticitás, elektronegativitás, elektronaffinitás, sztereokiválasztás stb. Ezáltal a töltésmigrációs dinamika kifejezetten alkalmas hatékony push-pull rendszerek modellezésére. Egy aromás gyűrűvel rendelkező molekulák esetén az aromaticitás vizsgálata nem túl bonyolult, de a két vagy több aromás gyűrűből álló molekuláknál (pl. adenin, guanin vagy a 2,1,3-benzotiadiazol) a vizsgálat jelentősen megnehezül. A töltésmigrációs dinamikában lévő különbség az egy és több gyűrűből álló molekulák aromaticitásával függ össze. Ezen eredmények a 5. fejezetben találhatók.

4. Fotoionizáció után a töltés szub-femtoszekundomos oszcillációja a molekulát alkotó atomok pozíciói között elektron-atommag csatolt nemadiabatikus folyamathoz vezet. E folyamat keto-uracilban való tanulmányozása során a molekula energiaszintjeit és rezgési állapotait is figyelembe vesszük. Kísérletekben az ultrarövid fényimpulzusok 15 eV alatt ionizálják a kationos állapotokat és számos alacsony rendű rezgési módust. E körülmények elméleti modellezéséhez olyan Hamilton-operátort választottam, amelynél a rezgési módusok 1(ν_1)-től 10 (ν_{10})-ig vannak csatolva az ionizációs spektrum első 12 kationos állapotához. A potenciálenergia-felület metszeteket mindegyik módusra ábrázoltam, a gyengétől az erős rezgési állapotig, majd illesztéssel határoztam meg a nemadiabatikus csatolási állandókat. A nemadiabatikus dinamika tanulmányozásához propagáltattam a gerjesztett állapot hullámcsomagját a multikonfigurációs időfüggő Hartree-módszert (MCTDH) alkalmazva. Bemutattam, hogy az első 12 állapot egyetlen rezgési módussal való csatolásakor a nemadiabatikus dinamikai folyamat az ionizációt követő 15. femtoszekundumnál kezdődik. Több rezgési módussal való csatolás esetén az elektron-atommag csatolás erősebb lesz, így több energiaállapot vesz részt a populációs transzferben és ez gyorsabb nemadiabatikus dinamikát eredményez. A kation uracil nemadiabatikus dinamikájára vonatkozó eredmények a disszertáció 6

fejezetében találhatók.

5. A töltésmigráció összetett kísérleti módszerekkel való tanulmányozásához elengedhetetlen a molekulák irányítottságának nagyfokú beállítása. Molekula lézertér általi irányítottságának tanulmányozása és szabályozása érdekében nélkülözhetetlen a folyamat és a molekuláris forgási állapotok közötti összefüggés megértése. A 7. fejezetben prototípus rendszeren (CH_3F) tanulmányoztam a forgási állapotok populációjának változását a lézer paramétereinek kísérleti változtatása nyomán. Kétféle molekulabeállítási viselkedést, úgy nevezett konvencionális és nemkonvencionális revivalt figyeltem meg. E két viselkedés összefüggésben áll a kiválasztott lézerparaméterekkel történő gerjesztés nyomán kialakuló forgási állapotokkal. Tudományos publikációban [T4][212] ismertettük a forgási állapotok finomhangolásának szükségességét a lézertér által előidézett molekula-irányítottság javítása érdekében. Az eredmények összefoglalva a 7. fejezetben találhatók.

Doktori értekezésem fő célja a nagy molekulákban foton által kiváltott töltésmigrációs és töltésátadásos folyamatok atomi szintű megértése. Ezek az ultragyors válaszidők befolyásolják a molekulákban és szilárd anyagokban lejátszódó fotofizikai és fotokémiai folyamatokat. Így a jelen dolgozatban bemutatott eredmények főként a molekulatervezéssel foglalkozó vegyészeknek lehetnek hasznosak, valamint segíthetnek a biológusoknak megérteni, hogyan hat a sugárterápia a nukleobázisokra. A témában már több érdekes folyóiratcikk is megjelent, de még vannak tisztázandó kérdések. A disszertációmban bemutatott optimalizált szimulációs módszerek és elemzések felhasználásával megérthetjük a töltésugrást, az izomerizációt vagy a nukleobázisok fragmentációját a DNS-ben az ionizáció előtti és utáni állapotok összehasonlításával, valamint azt, hogy miért és hogyan változik a festékmolekulák fotonkonverziós hatásfoka a π-távolságtartó (spacer) csoport áthelyezése miatt. Ismertetem, hogy az atomi szintű szimulációval kapott mikroszkopikus tulajdonságok milyen összefüggésben állnak a makroszkopikus szintű, kísérletileg is mérhető molekuláris válaszokkal. Ahogy a dolgozatban kifejtem, a töltésmigráció pontos idő- és iránybeli függésének kiszámítása felhasználható arra, hogy a molekulatervezés során fokozottan előtérbe kerüljenek a nagy molekulák kívánatos tulajdonságai. A tanulmány segítségével értékelhetők a molekulák annak érdekében, hogy növeljük a perovszkit anyagok határfelületi töltésdinamikáját, stabilitását, hatásfokát és élettartamát [226, 227, 228]. A dolgozat tovább bővíthető, hogy megértsük a különböző közegek vagy molekulák közötti kölcsönhatások hatását a töltésmigrációs dinamikára[229, 230] és olyan nemlineáris optikai tulajdonságokra, mint a magasharmonikus-keltés spektruma.[231] Reméljük, hogy az eredményeink további kutatásokra ösztönöznek és újabb utakat nyitnak a molekulamodellezés irányában.

Publications

Journal publications

IF: Impact factor
[T1] **Kalyani Chordiya**, Ehesan Ali, Mousumi Upadhyay Kahaly Photoexcited Intramolecular Charge Transfer in Dye Sensitizers: Predictive In Silico Screening for Dye-Sensitized Solar Cell Devices. *ACS Omega*, **7**, 13465-13474, 2022. (IF: 4.132)

[T2] **Kalyani Chordiya**, Victor Despré, Mousumi Upadhyay Kahaly, and Alexander I. Kuleff Distinctive onset of electron correlation in molecular tautomers. *Physical Review A*, **105**, 062808, 2022 (IF: 2.971).

[T3] **Kalyani Chordiya**, Victor Despré, Balázs Nagyillés, Felix Zeller, Zsolt Divéki, Alexander I. Kuleff, and Mousumi Upadhyay Kahaly Photo-ionization Initiated Differential Ultrafast Charge Migration: Impact of Molecular Symmetries and Tautomeric Forms. *Physical Chemistry Chemical Physics, in press*, 2022 (IF: 3.945).

[T4] **Kalyani Chordiya**, Irén Simkó, Tamás Szidarovszky, Mousumi Upadhyay Kahaly Achieving high molecular alignment and orientation for CH3F through manipulation of rotational states with varying optical and THz laser pulse parameters. *Scientific Reports*, **12**, 1-10, 2022 (IF: 4.996).

Further related publications

[O1] Yanyan Duan, **Kalyani Chordiya**, Mousumi Upadhyay Kahaly, Freddy E Oropeza, Víctor A de la Peña O'Shea, De-Yi Wang, Ruben D Costa Rational Amphiphilic Ligand Engineering Enables Enhanced Stability and Efficiency of CsPbBr3 Nanocrystals Based Light Emitting Diodes. *Advanced Optical Materials*, 2201176, 2022 (IF: 10.05).

[O2] He Zhao, **Kalyani Chordiya**, Petri Leukkunen, Alexey Popov, Mousumi Upadhyay Kahaly, Krisztian Kordas, Satu Ojala Dimethylammonium iodide stabilized bismuth halide perovskite photocatalyst for hydrogen evolution. *Nano Research*, **14**, 1116-1125, 2020 (IF: 9.240).

[O3] **Kalyani Chordiya**, Gergely Norbert Nagy, Mousumi Upadhyay Kahaly Synthesis Techniques for Low Dimensional Magnets. *CRC Press, Fundamentals of Low Dimensional Magnets*, Chapter 4, 2022.

[O4] Irén Simkó, **Kalyani Chordiya** Attila Csaszar, G, Mousumi Kahaly, Upadhyay, Tamás Szidarovszky A quantum-chemical perspective on the laser-induced alignment and orientation dynamics of the CH3X (X = F, Cl, Br, I) molecules. *Journal of Computational Chemistry*, **43**, 519-538, 2022 (IF: 3.672).

[O5] Swathi Erekath, **Kalyani Chordiya**, K V Vidhya, Mousumi Upadhyay Kahaly and Sreeram K Kalpathy Self-aggregation, H-bonding, and Photoresponse in Film and Solution States of Azobenzene Containing Polyurea. *Physical Chemistry Chemical Physics*, **24**, 23447 - 23459, 2022 (IF: 3.945).
Cumulative impact factor: 42.951
MTMT number: 10081219

Acknowledgments

During doctoral studies, the most important thing is to receive all the support needed to overcome all the ups and downs we encounter on the way. I would like to thank my supervisor, Dr. Mousumi Upadhyay Kahaly, from the bottom of my heart for directing my PhD studies and for supporting me during the entire journey. Although this is not her main area of research, her extensive motivation and support have helped me complete my doctoral thesis and pursue my research in the field of ultrafast charge migration in molecules. She has always supported me in all possible ways during the entire time. I have very much enjoyed working with Dr. Mousumi; her enthusiasm and positive attitude have always helped me cross most of the hurdles. She has always been open to new collaboration and research ideas, which has helped us publish together many of our works in a short period of time. I would like to thank Dr. Subhendu Kahaly, Prof. Katalin Varjú, Prof. Dimitris Charalambidis, Prof. Sándor Varró, Prof. Zoltán Keresztes, Dr. Zsolt Divéki, Dr. Attila Zoltán Czirják, Dr. Péter Dombi, Prof. József Fülöp, Dr. Ashutosh Sharma, Zsolt Szabó and Dr. Vineet Gupta from ELI ALPS their constant support. I would like to thank Judit Zelena for proofreading my thesis and giving her valuable suggestions.

I would like to thank Prof. Alexander I. Kuleff and Dr. Victor Despré from the University of Heidelberg, who helped me learn the ADC code and the MCTDH program, as well as analyze and understand the results for charge migration and non-adiabatic dynamics. Without their support this thesis would have not been completed. Dr. Victor Despré was very supportive and prompt in answering the emails, whenever I had doubts regarding the calculations or understanding a concept or analysis of the results. With his help, manuscript writing and publishing went very smoothly. He also always guided me towards the right references and helped me find the literature that had most of the answers. This has helped me become independent in finding helpful references and learning collaborative skills. The open and broad way thinking of both Prof. Alexander and Dr. Victor gave me courage to express my thoughts and ideas, which were then refined in a manner that motivated me to investigate them further scientifically.

During my two short visits over the last three years I could learn from the greatest minds at the PCI Department of the University of Heidelberg. I am grateful for the opportunity I was given by ELI ALPS and by the group at Heidelberg to connect with this dynamic theoretical group. During this time, I could not only interact but also observe how Prof. Lorenz Cederbaum, Prof. Horst Köppel, Prof. Hans-Dieter Meyer, Prof. Jochen Schirmer and Prof. Alexander Kuleff spend their time during research and during the breaks. It was a very positive research environment where the people were not only professionally brilliant and successful, but also kind and ground to earth during their interactions. It was a pleasure for me to have discussions with Dr. Markus Schröder, Jacqueline Fedyk, Johana A. Gomez, Daniel Bultrini, Dr. David Mendive Tapia, Dr. Krishna R.

Nandipati, Annette Braun and Marion Rudtk; they were all very kind and supportive during my time in Heidelberg.

I would like to acknowledge Irén Simkó and Dr. Tamás Szidarovszky from the Institute of Chemistry, ELTE Eötvös Loránd University and ELKH-ELTE Complex Chemical Systems Research Group for their support and collaboration on the project on laser induced alignment and orientation dynamics in molecular systems. I would like to thank Irén Simkó for being part of this project and helping me in understanding the LIMAO code, running the calculations and the analysis of the results. I would like to thank Dr. Tamás Szidarovszky for his great help in drafting the manuscript and running the calculations. Although we never met in person, the work went very smoothly and I am grateful for the healthy and strong collaborative efforts from Irén Simkó and Dr. Tamás Szidarovszky.

During my PhD programme, I was fortunate to gain many experimental collaborators, some of whom were my colleagues from the past, and I am very grateful for their trust in me and my work. I would like to thank my previous supervisor Prof. Krisztian Kordas, Topias Jarvinen, Dr. Seyed Hosseini Shokouh, He Zhao, and Dr. Satu Ojala from the University of Oulu, Finland. I would like to thank Prof. Sreeram K. Kalpathy, Dr. Swathi Erekath, K V Vidhya from the Indian Institute of Technology (IIT) Madras, India. I would like to thank Dr. Sachin Rondiya from the Indian Institute of Sciences, India; and Yanyan Duan and Prof. Ruben D Cost from IMDEA Materials Institute, Spain.

It has been a long journey from my bachelor's studies to the final stage of my PhD. I had a great passion towards understanding and designing molecules since the beginning of my university studies. The constant question for me has been how they can be designed to be efficient in the charge transfer process. I would like to thank all my teachers and professors throughout my studies in helping me reach this point in life and pursue my passion. I would like to thank Mrs. Jatinder Kaur, and Dr. Parbati Bandyopadhyay from Fergusson College, Pune. They guided me to do research and encouraged me to work with Prof. Sangeeta Kale and Dr. Rohini Kitture from DIAT, Pune. I am grateful to Prof. Amitava Das and Dr. Tanmay Banerjee from the National Chemical Laboratory, Pune for the amazing two-month experience on the synthesis of organic molecules for solar cell applications, as well as to Prof. Ehesan Ali, who strongly supported me during the preparation of my master's thesis. I would also like to thank Prof. Shashank Bhatnagar, Dr. Sanjeev Kumar, Dr. Suneel Kumar, Prof. Rajesh Sharma, Dr. Shaveen Garg and Dr. Ajay Srivastava. I would like to express my gratitude to my friends and colleagues Sayali Woo, Ankita Katkar, Gurpartap Singh, Dr. Ashish Bhatt, Dr. Prabhleen Kaur, Dr. Munish Sharma, Ashima Bajaj, Shikha Sharma, Abhishek Gupta, Dr. Shivani Choudhary, Saibabu Madas, Gergely Nagy, Dr. Lénárd Gulyás, Dr. Ujwala Pawar, Rasika Shiledar, Abhishek Lulhe, Prasad Adhav, Shreya Srivastava and Sameer Gupta.

There are several moments that can make you give up and take the easy road. During this time all one needs is support from family who can help you get past those moments. I would like to thank my mother Kalpana Chordiya, father Vijay Chordiya, siblings Dr. Rashmi Chordiya, Shradha Chordiya and Hrishikesh Chordiya for always being there for me. I would like to thank my friend, colleague and husband Balázs Nagyillés, who has been very supportive and who has helped me throughout my PhD. I would like to thank my in-laws László Nagyillés, Katalin Nagyillés, Bálint Nagyillés, Anikó Nagyillés Glässerné and Norbert Glässer for their love and support.

I could not have conducted my research without the grant provided by the European Union and co-financed by the European Regional Development Fund (GINOP-2.3.6- 15-2015-00001). Our project no. 2019-2.1.13-TÉT-IN-2020-00059 has been implemented with the support from the National Research, Development and Innovation Fund of Hungary, and has been financed under the 2019-2.1.13-TÉT-IN funding scheme. And last but not least, I would like to acknowledge funding from the PaNOSC European project through the European Union's Horizon 2020 research and innovation programme under grant agreement No 823852. I would also like to acknowledge the ITC Conference Grant for attending schools and conference by COST (European Cooperation on Science and Technology) CA18222 - Attosecond Chemistry (AttoChem), and CA17126 - Toward Understanding and Modelling Intense Electronic Excitation (TUMIEE). This work benefited from networking activities carried out within the EU funded COST Action AttoChem (CA18222) and TUMIEE (CA17126) and represents a contribution to it. I would to acknowledge the computational resources provided by ELI ALPS, The University of Heidelberg and KIFÜ for awarding us access to resources based in Hungary. The support of Dr. Attila Fekete from KIFÜ, and the IT team of ELI ALPS, Hungary for the technical work is gratefully acknowledged.

Bibliography

[1] Weiran Cao, Jian Li, Hongzheng Chen, and Jiangeng Xue. Transparent electrodes for organic optoelectronic devices: a review. *Journal of Photonics for energy*, 4(1):040990, 2014.

[2] Cong Wang, Xiaotao Zhang, and Wenping Hu. Organic photodiodes and phototransistors toward infrared detection: materials, devices, and applications. *Chemical Society Reviews*, 49(3):653–670, 2020.

[3] Deping Qian, Zilong Zheng, Huifeng Yao, Wolfgang Tress, Thomas R Hopper, Shula Chen, Sunsun Li, Jing Liu, Shangshang Chen, Jiangbin Zhang, et al. Design rules for minimizing voltage losses in high-efficiency organic solar cells. *Nature materials*, 17(8):703–709, 2018.

[4] Yinfeng Zhang, Fang Fang, Li Li, and Jinfeng Zhang. Self-assembled organic nanomaterials for drug delivery, bioimaging, and cancer therapy. *ACS Biomaterials Science & Engineering*, 6(9):4816–4833, 2020.

[5] Ncediwe Tsolekile, Simphiwe Nelana, and Oluwatobi Samuel Oluwafemi. Porphyrin as diagnostic and therapeutic agent. *Molecules*, 24(14):2669, 2019.

[6] N. V. Golubev and A. I. Kuleff. Control of charge migration in molecules by ultrashort laser pulses. *Physical Review A*, 91(5):051401, 2015.

[7] Chuncheng Wang, Max DJ Waters, Pengju Zhang, Jiří Suchan, Vít Svoboda, Tran Trung Luu, Conaill Perry, Zhong Yin, Petr Slavíček, and Hans Jakob Wörner. Different timescales during ultrafast stilbene isomerization in the gas and liquid phases revealed using time-resolved photoelectron spectroscopy. *Nature Chemistry*, pages 1–7, 2022.

[8] R Weinkauf, EW Schlag, TJ Martinez, and RD Levine. Nonstationary electronic states and site-selective reactivity. *The Journal of Physical Chemistry A*, 101(42):7702–7710, 1997.

[9] Louise Belshaw, Francesca Calegari, Martin J. Duffy, Andrea Trabattoni, Luca Poletto, Mauro Nisoli, and Jason B. Greenwood. Observation of Ultrafast Charge Migration in an Amino Acid. *The Journal of Physical Chemistry Letters*, 3(24):3751–3754, December 2012.

[10] F. Calegari, D. Ayuso, A. Trabattoni, L. Belshaw, S. De Camillis, S. Anumula, F. Frassetto, L. Poletto, A. Palacios, P. Decleva, J. B. Greenwood, F. Martin, and M. Nisoli. Ultrafast electron dynamics in phenylalanine initiated by attosecond pulses. *Science*, 346(6207): 336–339, October 2014.

[11] Olga Smirnova, Yann Mairesse, Serguei Patchkovskii, Nirit Dudovich, David Villeneuve, Paul Corkum, and Misha Yu. Ivanov. High harmonic interferometry of multi-electron dynamics in molecules. *Nature*, 460(7258):972–977, August 2009.

[12] Peter M Kraus, Benoît Mignolet, Denitsa Baykusheva, Alisa Rupenyan, Lubos Hornỳ, Emmanuel F Penka, Guido Grassi, Oleg I Tolstikhin, Johannes Schneider, Frank Jensen, et al. Measurement and laser control of attosecond charge migration in ionized iodoacetylene. *Science*, 350(6262):790–795, 2015.

[13] PM Kraus, Oleg I Tolstikhin, Denitsa Baykusheva, Alisa Rupenyan, Johannes Schneider, Christer Z Bisgaard, Toru Morishita, Frank Jensen, Lars Bojer Madsen, and Hans Jakob Wörner. Observation of laser-induced electronic structure in oriented polyatomic molecules. *Nature Communications*, 6(1):1–8, 2015.

[14] Peng Peng, Claude Marceau, Marius Hervé, PB Corkum, A Yu Naumov, and DM Villeneuve. Symmetry of molecular rydberg states revealed by XUV transient absorption spectroscopy. *TiO2 Communications*, 10(1):1–8, 2019.

[15] Eva Lindroth, Francesca Calegari, Linda Young, Marion Harmand, Nirit Dudovich, Nora Berrah, and Olga Smirnova. Challenges and opportunities in attosecond and XFEL science. *Nature Reviews Physics*, 1(2):107–111, 2019.

[16] Hugh T Philipp, Lucas J Koerner, Marianne S Hromalik, Mark W Tate, and Sol M Gruner. Femtosecond radiation experiment detector for x-ray free-electron laser (XFEL) coherent x-ray imaging. *IEEE Transactions on Nuclear Science*, 57(6):3795–3799, 2010.

[17] Michael A Robb, Marco Garavelli, Massimo Olivucci, and Fernando Bernardi. A computational strategy for organic photochemistry. *Reviews in computational chemistry*, 15:87–146, 2000.

[18] Wolfgang Domcke, David Yarkony, and Horst Köppel. *Conical intersections: electronic structure, dynamics & spectroscopy*, volume 15. World Scientific, 2004.

[19] Yaping Wen, Lulu Fu, Gongqiang Li, Jing Ma, and Haibo Ma. Accelerated discovery of potential organic dyes for dye-sensitized solar cells by interpretable machine learning models and virtual screening. *Solar RRL*, 4(6):2000110, 2020.

[20] Viktor V Brus, Jaewon Lee, Benjamin R Luginbuhl, Seo-Jin Ko, Guillermo C Bazan, and Thuc-Quyen Nguyen. Solution-processed semitransparent organic photovoltaics: from molecular design to device performance. *Advanced Materials*, 31(30):1900904, 2019.

[21] Kyungdoc Kim, Seokho Kang, Jiho Yoo, Youngchun Kwon, Youngmin Nam, Dongseon Lee, Inkoo Kim, Youn-Suk Choi, Yongsik Jung, Sangmo Kim, et al. Deep-learning-based inverse design model for intelligent discovery of organic molecules. *npj Computational Materials*, 4 (1):1–7, 2018.

[22] L.S. Cederbaum and J. Zobeley. Ultrafast charge migration by electron correlation. *Chemical Physics Letters*, 307(3):205 – 210, 1999.

[23] A Marciniak, V Despré, Vincent Loriot, G Karras, M Hervé, L Quintard, F Catoire, C Joblin, Eric Constant, AI Kuleff, and F Lépine. Electron correlation driven non-adiabatic relaxation in molecules excited by an ultrashort extreme ultraviolet pulse. *Nature Communications*, 10 (1):1–8, 2019.

[24] V. Despré and A. I. Kuleff. Size effects in charge migration in alkyne chains. *Theoretical Chemistry Accounts*, 138(9):110, 2019.

[25] Aaron Temkin and Anand Bhatia. Autoionization. In Gordon Drake, editor, *Springer Handbook of Atomic, Molecular, and Optical Physics*, chapter 25, pages 391–399. Springer, New York, NY, 2006.

[26] L. S. Cederbaum, W. Domcke, J. Schirmer, and W. von Niessen. Correlation effects in the ionization of molecules: Breakdown of the molecular orbital picture. *Advances in Chemical Physics*, pages 115–159, 1986.

[27] Gregory D. Scholes. Long-range resonance energy transfer in molecular systems. *Annual Review of Physical Chemistry*, 54(1):57–87, 2003.

[28] Till Jahnke, Uwe Hergenhahn, Bernd Winter, Reinhard Dörner, Ulrike Frühling, Philipp V. Demekhin, Kirill Gokhberg, Lorenz S. Cederbaum, Arno Ehresmann, André Knie, and Andreas Dreuw. Interatomic and intermolecular coulombic decay. *Chemical Reviews*, 120(20): 11295–11369, 2020.

[29] Alexander I. Kuleff. *Ultrafast Electron Dynamics as a Route to Explore Chemical Processes*. The Royal Society of Chemistry, 2018. ISBN 978-1-78262-995-5.

[30] J Breidbach and LS Cederbaum. Universal attosecond response to the removal of an electron. *Physical Review Letters*, 94(3):033901, 2005.

[31] Alexander I. Kuleff and Lorenz S. Cederbaum. Tracing ultrafast interatomic electronic decay processes in real time and space. *Physical Review Letters*, 98:083201, Feb 2007.

[32] A. I Kuleff and L. S. Cederbaum. Ultrafast correlation-driven electron dynamics. *Journal of Physics B: Atomic, Molecular and Optical Physics*, 47(12):124002, 2014.

[33] Dmitri Lapotko, Ekaterina Lukianova, Michail Potapnev, Olga Aleinikova, and Alexander Oraevsky. Method of laser activated nano-thermolysis for elimination of tumor cells. *Cancer Letters*, 239(1):36 – 45, 2006.

[34] Ivan H. El-Sayed, Xiaohua Huang, and Mostafa A. El-Sayed. Selective laser photo-thermal therapy of epithelial carcinoma using anti-egfr antibody conjugated gold nanoparticles. *Cancer Letters*, 239(1):129 – 135, 2006.

[35] Stanley B Brown, Elizabeth A Brown, and Ian Walker. The present and future role of photodynamic therapy in cancer treatment. *The Lancet Oncology*, 5(8):497 – 508, 2004.

[36] Spiridoula Matsika, Michael Spanner, Marija Kotur, and Thomas C. Weinacht. Ultrafast relaxation dynamics of uracil probed via strong field dissociative ionization. *The Journal of Physical Chemistry A*, 117(48):12796–12801, 2013.

[37] N.R. Jena and P.C. Mishra. Formation of ring-opened and rearranged products of guanine: Mechanisms and biological significance. *Free Radical Biology and Medicine*, 53(1):81 – 94, 2012.

[38] M. K. Shukla and Jerzy Leszczynski. Phototautomerism in uracil: A quantum chemical investigation. *The Journal of Physical Chemistry A*, 106(37):8642–8650, 2002.

[39] Dana Nachtigallová, Adélia J. A. Aquino, Jaroslaw J. Szymczak, Mario Barbatti, Pavel Hobza, and Hans Lischka. Nonadiabatic dynamics of uracil: Population split among different decay mechanisms. *The Journal of Physical Chemistry A*, 115(21):5247–5255, 2011.

[40] CJ Ballhausen and Aage E Hansen. Electronic spectra. *Annual Review of Physical Chemistry*, 23(1):15–38, 1972.

[41] I Waller. Dynamical theory of crystal lattices by m. born and k. huang. *Acta Crystallographica*, 9(10):837–838, 1956.

[42] Max Born and W Heisenberg. Zur quantentheorie der molekeln. In *Original Scientific Papers Wissenschaftliche Originalarbeiten*, pages 216–246. Springer, 1985.

[43] Attila Bangha Szabo and Neil S. Ostlund. *Modern Quantum Chemistry: Introduction to Advanced Electronic Structure Theory*. Courier Corporation, 1989.

[44] Max Born, Kun Huang, and M Lax. Dynamical theory of crystal lattices. *American Journal of Physics*, 23(7):474–474, 1955.

[45] István Mayer. *Simple theorems, proofs, and derivations in quantum chemistry*. Springer Science & Business Media, 2003.

[46] Robert K Nesbet. *Variational principles and methods in theoretical physics and chemistry*. Cambridge University Press, 2002.

[47] Pierre Hohenberg and Walter Kohn. Inhomogeneous electron gas. *Physical review*, 136(3B): B864, 1964.

[48] Walter Kohn and Lu Jeu Sham. Self-consistent equations including exchange and correlation effects. *Physical review*, 140(4A):A1133, 1965.

[49] David S Sholl and Janice A Steckel. *Density functional theory: a practical introduction*. John Wiley & Sons, 2011.

[50] Erich Runge and Eberhard KU Gross. Density-functional theory for time-dependent systems. *Physical Review Letters*, 52(12):997, 1984.

[51] LS Cederbaum and W Domcke. Theoretical aspects of ionization potentials and photoelectron spectroscopy: A Green's function approach. *Advances in Chemical Physics*, 36:205–344, 2007.

[52] J Schirmer, LS Cederbaum, and O Walter. New approach to the one-particle Green's function for finite Fermi systems. *Physical Review A*, 28(3):1237, 1983.

[53] Jochen Schirmer. Beyond the random-phase approximation: A new approximation scheme for the polarization propagator. *Physical Review A*, 26(5):2395, 1982.

[54] F. Mertins and J. Schirmer. Algebraic propagator approaches and intermediate-state representations. i. the biorthogonal and unitary coupled-cluster methods. *Physical Review A*, 53: 2140–2152, 1996.

[55] Jochen Schirmer. Closed-form intermediate representations of many-body propagators and resolvent matrices. *Physical Review A*, 43:4647–4659, 1991.

[56] J. Breidbach and L. S. Cederbaum. Migration of holes: Formalism, mechanisms, and illustrative applications. *The Journal of Chemical Physics*, 118(9):3983–3996, 2003.

[57] Holger Hennig, Jörg Breidbach, and Lorenz S. Cederbaum. Charge transfer driven by electron correlation: A non-Dyson propagator approach. *The Journal of Chemical Physics*, 122 (13):134104, 2005.

[58] Holger Hennig, Jörg Breidbach, and Lorenz S. Cederbaum. Electron correlation as the driving force for charge transfer: Charge migration following ionization in n-methyl acetamide. *The Journal of Physical Chemistry A*, 109(3):409–414, 2005.

[59] Alexander I. Kuleff, Siegfried Lünnemann, and Lorenz S. Cederbaum. Ultrafast reorganization of the hole charge created upon outer-valence ionization of porphyrins. *Chemical Physics*, 399:245 – 251, 2012.

[60] J. Breidbach and L. S. Cederbaum. Migration of holes: Numerical algorithms and implementation. *The Journal of Chemical Physics*, 126(3):034101, 2007.

[61] GA Worth, HD Meyer, LS Cederbaum, W Domcke, D Yarkony, and H Köppel. *Multidimensional dynamics involving a conical intersection: Wavepacket calculations using the MCTDH method*, volume 15. World Scientific: Singapore, 2004.

[62] Chr Cattarius, Graham A Worth, H-D Meyer, and LS Cederbaum. All mode dynamics at the conical intersection of an octa-atomic molecule: Multi-configuration time-dependent hartree (MCTDH) investigation on the butatriene cation. *The Journal of Chemical Physics*, 115(5):2088–2100, 2001.

[63] A Raab, Graham A Worth, H-D Meyer, and LS Cederbaum. Molecular dynamics of pyrazine after excitation to the s 2 electronic state using a realistic 24-mode model hamiltonian. *The Journal of Chemical Physics*, 110(2):936–946, 1999.

[64] H-D Meyer, Uwe Manthe, and Lorenz S Cederbaum. The multi-configurational time-dependent hartree approach. *Chemical Physics Letters*, 165(1):73–78, 1990.

[65] Michael H Beck, Andreas Jäckle, Graham A Worth, and H-D Meyer. The multiconfiguration time-dependent hartree (MCTDH) method: a highly efficient algorithm for propagating wavepackets. *Physics Reports*, 324(1):1–105, 2000.

[66] Hans-Dieter Meyer, Fabien Gatti, and Graham A Worth. *Multidimensional quantum dynamics: MCTDH theory and applications*. John Wiley & Sons, 2009.

[67] Tamás Szidarovszky, Maho Jono, and Kaoru Yamanouchi. LIMAO: Cross-platform software for simulating laser-induced alignment and orientation dynamics of linear-, symmetric-and asymmetric tops. *Computer Physics Communications*, 228:219–228, 2018.

[68] Philip R Bunker and Per Jensen. *Molecular symmetry and spectroscopy*. NRC Research Press, 2006.

[69] Kaoru Yamanouchi, Dimitrios Charalambidis, and Didier Normand. *Progress in Ultrafast Intense Laser Science XIII*. Springer, 2015.

[70] Michael Spanner, Serguei Patchkovskii, Eugene Frumker, and Paul Corkum. Mechanisms of two-color laser-induced field-free molecular orientation. *Physical Review Letters*, 109(11): 113001, 2012.

[71] Richard N Zare. *Angular momentum*, volume 33. Wiley, New York, 1988.

[72] Daeyul Baek, Hirokazu Hasegawa, and Yasuhiro Ohshima. Unveiling the nonadiabatic rotational excitation process in a symmetric-top molecule induced by two intense laser pulses. *The Journal of Chemical Physics*, 134(22):224302, 2011.

[73] Kalyani Chordiya, Md Ehesan Ali, and Mousumi U Kahaly. Photoexcited intramolecular charge transfer in dye sensitizers: Predictive in silico screening for dye-sensitized solar cell devices. *ACS omega*, 7(16):13465–13474, 2022.

[74] Brian O'regan and Michael Grätzel. A low-cost, high-efficiency solar cell based on dye-sensitized colloidal TiO2 films. *Nature*, 353(6346):737–740, 1991.

[75] Meidan Ye, Xiaoru Wen, Mengye Wang, James Iocozzia, Nan Zhang, Changjian Lin, and Zhiqun Lin. Recent advances in dye-sensitized solar cells: from photoanodes, sensitizers and electrolytes to counter electrodes. *Materials Today*, 18(3):155–162, 2015.

[76] Sam-Shajing Sun. Design of a block copolymer solar cell. *Solar energy materials and solar cells*, 79(2):257–264, 2003.

[77] Federico Bella and Claudio Gerbaldi. Natural polymers for dye-sensitized solar cells: Electrolytes and electrodes. *Encyclopedia of Polymer Science and Technology*, pages 1–17, 2002.

[78] Marina Freitag and Gerrit Boschloo. The revival of dye-sensitized solar cells. *Current Opinion in Electrochemistry*, 2(1):111–119, 2017.

[79] Kenji Kakiage, Yohei Aoyama, Toru Yano, Keiji Oya, Jun-ichi Fujisawa, and Minoru Hanaya. Highly-efficient dye-sensitized solar cells with collaborative sensitization by silyl-anchor and carboxy-anchor dyes. *Chemical Communications*, 51(88):15894–15897, 2015.

[80] Stefano Caramori, Vito Cristino, Rita Boaretto, Roberto Argazzi, Carlo Alberto Bignozzi, and Aldo Di Carlo. New components for dye-sensitized solar cells. *International Journal of Photoenergy*, 2010, 2010.

[81] John N Clifford, Eugenia Martínez-Ferrero, Aurélien Viterisi, and Emilio Palomares. Sensitizer molecular structure-device efficiency relationship in dye sensitized solar cells. *Chemical Society Reviews*, 40(3):1635–1646, 2011.

[82] S Shalini, R Balasundaraprabhu, T Satish Kumar, N Prabavathy, S Senthilarasu, and S Prasanna. Status and outlook of sensitizers/dyes used in dye sensitized solar cells (DSSC): a review. *International Journal of Energy Research*, 40(10):1303–1320, 2016.

[83] Zhijie Xu, Shaolei Gao, Xiaoqing Lu, Yuanyuan Li, Yameng Li, and Shuxian Wei. Theoretical analysis of the absorption spectrum, electronic structure, excitation, and intramolecular electron transfer of D-A'-π-A porphyrin dyes for dye-sensitized solar cells. *Physical Chemistry Chemical Physics*, 22(26):14846–14856, 2020.

[84] Shaorui Chen, Zhihan Pang, and Wenjun Wu. Electronic anti-injection effect for carbonyl in anchor group based on diphenylacetylene D2-π-A sensitizer in dye-sensitized solar cells. *International Journal of Energy Research*, 2020.

[85] Nuha Wazzan and Ahmad Irfan. Promising architectures modifying the D-π-A architecture of 2, 3-dipentyldithieno [3, 2-f: 2', 3'-h] quinoxaline-based dye as efficient sensitizers in dye-sensitized solar cells: A DFT study. *Materials Science in Semiconductor Processing*, 120: 105260, 2020.

[86] Rajneesh Misra, Ramesh Maragani, Deepali Arora, Abhishek Sharma, and Ganesh D Sharma. Positional isomers of pyridine linked triphenylamine-based donor-acceptor organic dyes for efficient dye-sensitized solar cells. *Dyes and Pigments*, 126:38–45, 2016.

[87] Yueqiang Wang, Bin Chen, Wenjun Wu, Xin Li, Weihong Zhu, He Tian, and Yongshu Xie. Efficient solar cells sensitized by porphyrins with an extended conjugation framework and a carbazole donor: from molecular design to cosensitization. *Angewandte Chemie*, 126(40): 10955–10959, 2014.

[88] Li Zhang, Xichuan Yang, Weihan Wang, Gagik G Gurzadyan, Jiajia Li, Xiaoxin Li, Jincheng An, Ze Yu, Haoxin Wang, Bin Cai, et al. 13.6% efficient organic dye-sensitized solar cells by minimizing energy losses of the excited state. *ACS Energy Letters*, 4(4):943–951, 2019.

[89] Yu Gao, Wei Guan, and Likai Yan. The effect of dyes with different π-linkers on the overall performance of p-DSSCs: Lessons from theory. *The Journal of Physical Chemistry A*, 122 (37):7491–7496, 2018.

[90] Chirawat Chitpakdee, Supawadee Namuangruk, Khomson Suttisintong, Siriporn Jungsuttiwong, Tinnagon Keawin, Taweesak Sudyoadsuk, Kanokkorn Sirithip, Vinich Promarak, and Nawee Kungwan. Effects of π-linker, anchoring group and capped carbazole at meso-substituted zinc-porphyrins on conversion efficiency of DSSCs. *Dyes and Pigments*, 118: 64–75, 2015.

[91] Denis Jacquemin, Valérie Wathelet, Eric A Perpete, and Carlo Adamo. Extensive TD-DFT benchmark: singlet-excited states of organic molecules. *Journal of Chemical Theory and Computation*, 5(9):2420–2435, 2009.

[92] Natalia Martsinovich and Alessandro Troisi. High-throughput computational screening of chromophores for dye-sensitized solar cells. *The Journal of Physical Chemistry C*, 115(23): 11781–11792, 2011.

[93] Zbigniew R Grabowski and Jacek Dobkowski. Twisted intramolecular charge transfer (TICT) excited states: energy and molecular structure. *Pure and Applied Chemistry*, 55(2):245–252, 1983.

[94] Jinxia Liang, Chun Zhu, and Zexing Cao. Electronic and optical properties of the triphenylamine-based organic dye sensitized TiO2 semiconductor: insight from first principles calculations. *Physical Chemistry Chemical Physics*, 15(33):13844–13851, 2013.

[95] Florian Schiffmann, Joost VandeVondele, Jürg Hutter, Ronny Wirz, Atsushi Urakawa, and Alfons Baiker. Protonation-dependent binding of ruthenium bipyridyl complexes to the anatase (101) surface. *The Journal of Physical Chemistry C*, 114(18):8398–8404, 2010.

[96] Yujing Jin, Jing-Ai Qiao, Chang Liu, Ling Luo, Xin Chi, Yuexing Zhang, and Ming-Hua Zeng. Charge transfer and delocalization in ladder-type fused bithiophene imide oligomers. *The Journal of Physical Chemistry C*, 123(33):20093–20104, 2019.

[97] Zbigniew R Grabowski, Krystyna Rotkiewicz, and Wolfgang Rettig. Structural changes accompanying intramolecular electron transfer: focus on twisted intramolecular charge-transfer states and structures. *Chemical reviews*, 103(10):3899–4032, 2003.

[98] Xiu Jiang, Jiacheng Wang, Wei Wang, Yang Yang, Xiaowei Zhan, and Xingguo Chen. Impact of an electron withdrawing group on the thiophene-fused benzotriazole unit on the photovoltaic performance of the derived polymer solar cells. *Dyes and Pigments*, 166:381–389, 2019.

[99] Chunyang Jia, Shi-Xia Liu, Christian Tanner, Claudia Leiggener, Antonia Neels, Lionel Sanguinet, Eric Levillain, Samuel Leutwyler, Andreas Hauser, and Silvio Decurtins. An experimental and computational study on intramolecular charge transfer: A tetrathiafulvalene-fused dipyridophenazine molecule. *Chemistry–A European Journal*, 13(13):3804–3812, 2007.

[100] Chad M Amb, Song Chen, Kenneth R Graham, Jegadesan Subbiah, Cephas E Small, Franky So, and John R Reynolds. Dithienogermole as a fused electron donor in bulk heterojunction solar cells. *Journal of the American Chemical Society*, 133(26):10062–10065, 2011.

[101] Frank Neese. The ORCA program system. *Wiley Interdisciplinary Reviews: Computational Molecular Science*, 2(1):73–78, 2012.

[102] Frank Neese. Software update: the ORCA program system, version 4.0. *Wiley Interdisciplinary Reviews: Computational Molecular Science*, 8(1):e1327, 2018.

[103] MA Robb, JR Cheeseman, and G Scalmani. Gaussian, inc., wallingford ct, 2009.(b) adamo, c.; barone v. *Journal of Chemical Physics*, 110:6158–6170, 1999.

[104] Florian Weigend and Reinhart Ahlrichs. Balanced basis sets of split valence, triple zeta valence and quadruple zeta valence quality for H to Rn: Design and assessment of accuracy. *Physical Chemistry Chemical Physics*, 7(18):3297–3305, 2005.

[105] Florian Weigend. Accurate coulomb-fitting basis sets for H to Rn. *Physical chemistry Chemical Physics*, 8(9):1057–1065, 2006.

[106] Yu Takano and KN Houk. Benchmarking the conductor-like polarizable continuum model (CPCM) for aqueous solvation free energies of neutral and ionic organic molecules. *Journal of Chemical Theory and Computation*, 1(1):70–77, 2005.

[107] Gui Yu, Shiwei Yin, Yunqi Liu, Jiangshan Chen, Xinjun Xu, Xiaobo Sun, Dongge Ma, Xiaowei Zhan, Qian Peng, Zhigang Shuai, et al. Structures, electronic states, photoluminescence, and carrier transport properties of 1, 1-disubstituted 2, 3, 4, 5-tetraphenylsiloles. *Journal of the American Chemical Society*, 127(17):6335–6346, 2005.

[108] R.A. Marcus. On the theory of oxidation-reduction reactions involving electron transfer. i. *The Journal of Chemical Physics*, 24(5):966–978, 1956.

[109] R.A. Marcus. Chemical and electrochemical electron-transfer theory. *Annual Review of Physical Chemistry*, 15:155–196, 1964.

[110] R.A. Marcus. Electron transfer reactions in chemistry. theory and experiment. *Pure and Applied Chemistry*, 69(1):13–29, 1997.

[111] Joshua Jortner. Temperature dependent activation energy for electron transfer between biological molecules. *The Journal of Chemical Physics*, 64(12):4860–4867, 1976.

[112] M. Bixon and J. Jortner. Electron transfer - from isolated molecules to biomolecules. *Advances in Chemical Physics*, 106:35–202, 1999.

[113] N.R. Kestner, J. Logan, and J. Jortner. Thermal electron transfer reactions in polar solvents. *Journal of Physical Chemistry*, 78(21):2148–2166, 1974.

[114] Aleksey A. Kletsov. Electron propagator theory approach to ab initio calculations of electron transfer rate and molecular conductance. *Chemical Physics Letters*, 612:203 – 208, 2014.

[115] David Cahen, Gary Hodes, Michael Graetzel, Jean Francois Guillemoles, and Ilan Riess. Nature of photovoltaic action in dye-sensitized solar cells. *The Journal of Physical Chemistry B*, 104(9):2053–2059, 2000.

[116] John B Asbury, Yong-Qiang Wang, Encai Hao, Hirendra N Ghosh, and Tianquan Lian. Evidences of hot excited state electron injection from sensitizer molecules to TiO2 nanocrystalline thin films. *Research on Chemical Intermediates*, 27(4-5):393–406, 2001.

[117] Kenji Kakiage, Yohei Aoyama, Toru Yano, Takahiro Otsuka, Toru Kyomen, Masafumi Unno, and Minoru Hanaya. An achievement of over 12 percent efficiency in an organic dye-sensitized solar cell. *Chemical Communications*, 50(48):6379–6381, 2014.

[118] Jun-ichi Fujisawa, Ayumi Osawa, and Minoru Hanaya. A strategy to minimize the energy offset in carrier injection from excited dyes to inorganic semiconductors for efficient dye-sensitized solar energy conversion. *Physical Chemistry Chemical Physics*, 18(32):22244–22253, 2016.

[119] Mireille Blanchard-Desce, Rüdiger Wortmann, Sonja Lebus, Jean-Marie Lehn, and Peter Krämer. Intramolecular charge transfer in elongated donor-acceptor conjugated polyenes. *Chemical Physics Letters*, 243(5-6):526–532, 1995.

[120] Jiangpu Hu, Yang Li, Huaning Zhu, Shuhai Qiu, Guiying He, Xiaozhang Zhu, and Andong Xia. Photophysical properties of intramolecular charge transfer in a tribranched donor–π–acceptor chromophore. *ChemPhysChem*, 16(11):2357–2365, 2015.

[121] Wei Ma, Yang Jiao, and Sheng Meng. Modeling charge recombination in dye-sensitized solar cells using first-principles electron dynamics: effects of structural modification. *Physical Chemistry Chemical Physics*, 15(40):17187–17194, 2013.

[122] Hirofumi Naito, Kenta Nishino, Yasuhiro Morisaki, Kazuo Tanaka, and Yoshiki Chujo. Solid-state emission of the anthracene-o-carborane dyad from the twisted-intramolecular charge transfer in the crystalline state. *Angewandte Chemie International Edition*, 56(1):254–259, 2017.

[123] Shreetama Karmakar, Abhinandan Ambastha, Ajay Jha, Aditya K Dharmadhikari, Jayashree A Dharmadhikari, Ravindra Venkatramani, and Jyotishman Dasgupta. Transient raman snapshots of the twisted intramolecular charge transfer state in a stilbazolium dye. *The Journal of Physical Chemistry Letters*, 2020.

[124] Yifan Liu, Xiaomin Zhang, Chen Li, Yuqi Tian, Fengyu Zhang, Yajun Wang, Wenjun Wu, and Bo Liu. Energy-level control via molecular planarization and its effect on interfacial charge-transfer processes in dye-sensitized solar cells. *The Journal of Physical Chemistry C*, 123(22):13531–13537, 2019.

[125] L S Cederbaum. One-body Green's function for atoms and molecules: theory and application. *Journal of Physics B: Atomic and Molecular Physics*, 8(2):290–303, Feb 1975.

[126] Jaroslav Rejnek, Michal Hanus, Martin Kabeláč, Filip Ryjáček, and Pavel Hobza. Correlated ab initio study of nucleic acid bases and their tautomers in the gas phase, in a microhydrated environment and in aqueous solution. part 4. uracil and thymine. *Physical Chemistry Chemical Physics*, 7(9):2006–2017, 2005.

[127] Yuko Tsuchiya, Teruhiko Tamura, Masaaki Fujii, and Mitsuo Ito. Keto-enol tautomer of uracil and thymine. *The Journal of Physical Chemistry*, 92(7):1760–1765, 1988.

[128] Diego D Colasurdo, Matías N Pila, Dacio A Iglesias, Sergio L Laurella, and Danila L Ruiz. Tautomerism of uracil and related compounds: A mass spectrometry study. *European Journal of Mass Spectrometry*, 24(2):214–224, 2018.

[129] Kafila Saïagh, Hervé Cottin, Aicha Aleian, and Nicolas Fray. VUV and Mid-UV photoabsorption cross sections of thin films of guanine and uracil: Application on their photochemistry in the solar system. *Astrobiology*, 15(4):268–282, 2015.

[130] Kalyani Chordiya, Victor Despré, Mousumi U Kahaly, and Alexander I Kuleff. Distinctive onset of electron correlation in molecular tautomers. *Physical Review A*, 105(6):062808, 2022.

[131] Kalyani Chordiya, Victor Despré, Balázs Nagyillés, Felix Zeller, Zsolt Diveki, Alexander I Kuleff, and Mousumi U Kahaly. Photo-ionization initiated differential ultrafast charge migration: Impact of molecular symmetries and tautomeric forms. *Physical Chemistry Chemical Physics, in press*, 2022.

[132] Hans-Joachim Werner and Peter J Knowles. A second order multiconfiguration SCF procedure with optimum convergence. *The Journal of Chemical Physics*, 82(11):5053–5063, 1985.

[133] P.J. Knowles, G.J. Sexton, and N.C. Handy. Studies using the CASSCF wavefunction. *Chemical Physics*, 72(3):337 – 347, 1982.

[134] Martyn F Guest, Ian J Bush, Huub JJ Van Dam, Paul Sherwood, Jens MH Thomas, Joop H Van Lenthe, Remco WA Havenith, and John Kendrick. The GAMESS-UK electronic structure package: algorithms, developments and applications. *Molecular physics*, 103(6-8):719–747, 2005.

[135] Florian Weigend and Reinhart Ahlrichs. Balanced basis sets of split valence, triple zeta valence and quadruple zeta valence quality for H to Rn: Design and assessment of accuracy. *Physical Chemistry Chemical Physics*, 7:3297–3305, 2005.

[136] Thom H Dunning Jr. Gaussian basis sets for use in correlated molecular calculations. I. the atoms boron through neon and hydrogen. *The Journal of Chemical Physics*, 90(2):1007–1023, 1989.

[137] J. Schirmer, L. S. Cederbaum, and O. Walter. New approach to the one-particle Green's function for finite Fermi systems. *Physical Review A*, 28:1237–1259, 1983.

[138] J. Schirmer, A. B. Trofimov, and G. Stelter. A non-Dyson third-order approximation scheme for the electron propagator. *The Journal of Chemical Physics*, 109(12):4734–4744, 1998.

[139] Cornelius Lanczos. An iteration method for the solution of the eigenvalue problem of linear differential and integral operators. *Journal of Research of the National Bureau of Standards*, 1950.

[140] Al Mokhtar Lamsabhi, Soledad Gutiérrez-Oliva, Otilia Mó, Alejandro Toro-Labbé, and Manuel Yáñez. Effects of the ionization in the tautomerism of uracil: A reaction electronic flux perspective. *Journal of Computational Chemistry*, 36(28):2135–2145, 2015.

[141] Erik P Månsson, Simone Latini, Fabio Covito, Vincent Wanie, Mara Galli, Enrico Perfetto, Gianluca Stefanucci, Umberto De Giovannini, Mattea Carmen Castrovilli, Andrea Trabattoni, et al. Ultrafast dynamics of adenine following XUV ionization. *Journal of Physics: Photonics*, 2022.

[142] Victor Despré and Alexander I Kuleff. Correlation-driven charge migration as an initial step of the dynamics in correlation bands. *Physical Review A*, 106:L021501, 2022.

[143] Roald Hoffmann. Interaction of orbitals through space and through bonds. *Accounts of Chemical Research*, 4(1):1–9, 1971.

[144] John B Mullenix, Victor Despré, and Alexander I Kuleff. Electronic decay through non-linear carbon chains. *Journal of Physics B: Atomic, Molecular and Optical Physics*, 53(18):184006, jul 2020.

[145] V Despré, A Marciniak, V Loriot, MCE Galbraith, A Rouzée, MJJ Vrakking, F Lépine, and AI Kuleff. Attosecond hole migration in benzene molecules surviving nuclear motion. *The Journal of Physical Chemistry Letters*, 6(3):426–431, 2015.

[146] V. Despré, N. V. Golubev, and A. I. Kuleff. Charge migration in propiolic acid: A full quantum dynamical study. *Physical Review Letters*, 121(20):203002, 2018.

[147] Péter Sándor, Adonay Sissay, François Mauger, Mark W Gordon, TT Gorman, TD Scarborough, Mette B Gaarde, Kenneth Lopata, KJ Schafer, and RR Jones. Angle-dependent strong-field ionization of halomethanes. *The Journal of Chemical Physics*, 151(19):194308, 2019.

[148] M. S. Deleuze and L. S. Cederbaum. Formation of satellite bands in the ionization spectra of extended systems. *Physical Review B*, 53(20):13326, 1996.

[149] M. Hervé, V. Despré, P. Castellanos Nashn, V. Loriot, A. Boyer, A. Scognamiglio, G. Karras, R. Brédy, E. Constant, A. G. G. M. Tielens, A. I. Kuleff, and F. Lépine. Ultrafast dynamics of correlation bands following XUV molecular photoionization. *Nature Physics*, 17:327–331, 2021.

[150] Erik P Månsson, Simone Latini, Fabio Covito, Vincent Wanie, Mara Galli, Enrico Perfetto, Gianluca Stefanucci, Hannes Hübener, Umberto De Giovannini, Mattea C Castrovilli, et al. Real-time observation of a correlation-driven sub 3 fs charge migration in ionised adenine. *Communications Chemistry*, 4(1):1–7, 2021.

[151] Ewa Daniela Raczyńska, Wanda Kosińska, Borys Ośmiałowski, and Ryszard Gawinecki. Tautomeric equilibria in relation to pi-electron delocalization. *Chemical reviews*, 105(10):3561–3612, 2005.

[152] Clemens von Sonntag. Pulse radiolysis of nucleic acids and their base constituents: an updating review. *International Journal of Radiation Applications and Instrumentation. Part C. Radiation Physics and Chemistry*, 30(5-6):313–330, 1987.

[153] P O'Neill. *The Chemical Basis of Radiation Biology*. Taylor & Francis, 1987.

[154] U Hagen. Molecular radiation biology: future aspects. *Radiation and Environmental Biophysics*, 29(4):315–322, 1990.

[155] M Dizdaroglu. Measurement of radiation-induced damage to DNA at the molecular level. *International Journal of Radiation Biology*, 61(2):175–183, 1992.

[156] Jürgen Huettermann, Wolfgang Koehnlein, and Robert Teoule. *Effects of ionizing radiation of DNA: physical, chemical, and biological aspects*. Springer-Verlag New York Inc., New York, NY, 1978.

[157] AT Al-Kazwini, P O'Neill, EM Fielden, and GE Adams. Radiation-induced luminescence from "dry" and hydrated DNA and related macromolecules. *International Journal of Radiation Applications and Instrumentation. Part C. Radiation Physics and Chemistry*, 32(3):385–389, 1988.

[158] Luis Pedro Candeias and Steen Steenken. Electron transfer in di (deoxy) nucleoside phosphates in aqueous solution: rapid migration of oxidative damage (via adenine) to guanine. *Journal of the American Chemical Society*, 115(6):2437–2440, 1993.

[159] S Maclot, R Delaunay, Dariusz Grzegorz Piekarski, A Domaracka, BA Huber, L Adoui, F Martín, Manuel Alcamí, L Avaldi, P Bolognesi, et al. Determination of energy-transfer distributions in ionizing ion-molecule collisions. *Physical Review Letters*, 117(7):073201, 2016.

[160] EP Månsson, Simone De Camillis, Mattea C Castrovilli, M Galli, M Nisoli, F Calegari, and JB Greenwood. Ultrafast dynamics in the DNA building blocks thymidine and thymine initiated by ionizing radiation. *Physical Chemistry Chemical Physics*, 19(30):19815–19821, 2017.

[161] Kyo-Won Choi, Joo-Hee Lee, and Sang Kyu Kim. Ionization spectroscopy of a DNA base: Vacuum-ultraviolet mass-analyzed threshold ionization spectroscopy of jet-cooled thymine. *Journal of the American Chemical Society*, 127(45):15674–15675, 2005.

[162] James A Green, Martha Yaghoubi Jouybari, Haritha Asha, Fabrizio Santoro, and Roberto Improta. Fragment diabatization linear vibronic coupling model for quantum dynamics of multichromophoric systems: Population of the charge-transfer state in the photoexcited guanine–cytosine pair. *Journal of Chemical Theory and Computation*, 17(8):4660–4674, 2021.

[163] Steen Steenken and Slobodan V Jovanovic. How easily oxidizable is DNA? one-electron reduction potentials of adenosine and guanosine radicals in aqueous solution. *Journal of the American Chemical Society*, 119(3):617–618, 1997.

[164] Isao Saito, Takashi Nakamura, Kazuhiko Nakatani, Yasunori Yoshioka, Kizashi Yamaguchi, and Hiroshi Sugiyama. Mapping of the hot spots for DNA damage by one-electron oxidation: efficacy of GG doublets and GGG triplets as a trap in long-range hole migration. *Journal of the American Chemical Society*, 120(48):12686–12687, 1998.

[165] Alessandro Troisi. Charge dynamics through pi-stacked arrays of conjugated molecules: effect of dynamic disorder in different transport/transfer regimes. *Molecular Simulation*, 32 (9):707–716, 2006.

[166] Halina Szatylowicz, Olga A Stasyuk, Miquel Solà, and Tadeusz M Krygowski. Aromaticity of nucleic acid bases. *Wiley Interdisciplinary Reviews: Computational Molecular Science*, 11 (4):e1509, 2021.

[167] L Nyulászi, G Csonka, J Réffy, T Veszprémi, and J Heinicke. Investigation of heterocyclic compounds containing a P-C or As-C bond by ultraviolet photoelectron spectroscopy. *Journal of organometallic chemistry*, 373(1):49–55, 1989.

[168] Ziyong Chen, Kai-Chung Lau, Gustavo A Garcia, Laurent Nahon, Dušan K Božanić, Lionel Poisson, Muneerah Mogren Al-Mogren, Martin Schwell, Joseph S Francisco, Ayad Bellili, et al. Identifying cytosine-specific isomers via high-accuracy single photon ionization. *Journal of the American Chemical Society*, 138(51):16596–16599, 2016.

[169] Guangyu Sun and Marc C Nicklaus. Natural resonance structures and aromaticity of the nucleobases. *Theoretical Chemistry Accounts*, 117(2):323–332, 2007.

[170] Michał K Cyrański, Mirosław Gilski, Mariusz Jaskólski, and Tadeusz Marek Krygowski. On the aromatic character of the heterocyclic bases of DNA and RNA. *The Journal of Organic Chemistry*, 68(22):8607–8613, 2003.

[171] Simon Mathew, Aswani Yella, Peng Gao, Robin Humphry-Baker, Basile FE Curchod, Negar Ashari-Astani, Ivano Tavernelli, Ursula Rothlisberger, Md Khaja Nazeeruddin, and Michael Grätzel. Dye-sensitized solar cells with 13% efficiency achieved through the molecular engineering of porphyrin sensitizers. *Nature chemistry*, 6(3):242–247, 2014.

[172] Omar Britel, Asmae Fitri, Adil Touimi Benjelloun, Ahmed Slimi, Mohammed Benzakour, and Mohammed Mcharfi. Theoretical investigation of the influence of π-spacer on photovoltaic performances in carbazole-based dyes for dye-sensitized solar cells applications. *Journal of Photochemistry and Photobiology A: Chemistry*, 428:113870, 2022.

[173] Bo Hyung Kim and Harold S Freeman. Structure–photovoltaic performance relationships for DSSC sensitizers having heterocyclic and benzene spacers. *Journal of Materials Chemistry*, 22(38):20403–20409, 2012.

[174] Kate E Horner and Peter B Karadakov. Shielding in and around oxazole, imidazole, and thiazole: how does the second heteroatom affect aromaticity and bonding? *The Journal of Organic Chemistry*, 80(14):7150–7157, 2015.

[175] CW Bird. A new aromaticity index and its application to five-membered ring heterocycles. *Tetrahedron*, 41(7):1409–1414, 1985.

[176] Kazuaki Kawashima, Itaru Osaka, and Kazuo Takimiya. Effect of chalcogen atom on the properties of naphthobischalcogenadiazole-based π-conjugated polymers. *Chemistry of Materials*, 27(19):6558–6570, 2015.

[177] Freek JM Hoeben, Pascal Jonkheijm, EW Meijer, and Albertus PHJ Schenning. About supramolecular assemblies of π-conjugated systems. *Chemical reviews*, 105(4):1491–1546, 2005.

[178] Margarida S Miranda, M Agostinha R Matos, Victor MF Morais, and Joel F Liebman. Paradigms and paradoxes: en route to the understanding of the aromaticity of the “iso-species” isobenzofuran, anthranil, benzofurazan and 2, 1, 3-benzothiadiazole. *Structural Chemistry*, 23(4):1241–1243, 2012.

[179] Margarida S Miranda, M Agostinha R Matos, Victor MF Morais, and Joel F Liebman. 2, 1, 3-benzothiadiazole: Study of its structure, energetics and aromaticity. *The Journal of Chemical Thermodynamics*, 50:30–36, 2012.

[180] R F W Bader. *Atoms In Molecules: A Quantum Theory*. Clarendon Press, Oxford, 1990.

[181] R S Mulliken. Electronic population analysis on LCAO–MO molecular wave functions. II. overlap populations, bond orders, and covalent bond energies. *Journal of Chemical Physics*, 23(10):1841–1846, 1955.

[182] M. Vacher, M. J. Bearpark, M. A. Robb, and J. P. Malhado. Electron dynamics upon ionization of polyatomic molecules: Coupling to quantum nuclear motion and decoherence. *Physical Review Letters*, 118(8):083001, 2017.

[183] C. Arnold, O. Vendrell, and R. Santra. Electronic decoherence following photoionization: Full quantum-dynamical treatment of the influence of nuclear motion. *Physical Review A*, 95(3):033425, 2017.

[184] Mariana Assmann, Horst Köppel, and Spiridoula Matsika. Photoelectron spectrum and dynamics of the uracil cation. *The Journal of Physical Chemistry A*, 119(5):866–875, 2015.

[185] Hugh Christopher Longuet-Higgins. The intersection of potential energy surfaces in polyatomic molecules. *Proceedings of the Royal Society of London. A. Mathematical and Physical Sciences*, 344(1637):147–156, 1975.

[186] Martina Döscher, Horst Köppel, and Péter G Szalay. Multistate vibronic interactions in the benzene radical cation. I. electronic structure calculations. *The Journal of Chemical Physics*, 117(6):2645–2656, 2002.

[187] Horst Köppel, M Döscher, I Bâldea, H-D Meyer, and PG Szalay. Multistate vibronic interactions in the benzene radical cation. II. quantum dynamical simulations. *The Journal of Chemical Physics*, 117(6):2657–2671, 2002.

[188] Graham Worth, LS Cederbaum, S Leone, P Alvisatos, and A McDermott. Beyond Born-Oppenheimer: Conical intersections and their impact on molecular dynamics. *Annual Review Physical Chemistry*, 2004.

[189] H Köppel, WCLS Domcke, and LS Cederbaum. Multimode molecular dynamics beyond the Born-Oppenheimer approximation. *Advances in Chemical Physics*, 57(59):140, 1984.

[190] Martin Head-Gordon, John A Pople, and Michael J Frisch. MP2 energy evaluation by direct methods. *Chemical Physics Letters*, 153(6):503–506, 1988.

[191] Th H Dunning and P Jeffery Hay. *Methods of electronic structure theory*, volume 3. Springer New York, NY, 1977.

[192] MJ Frisch, GW Trucks, HB Schlegel, GE Scuseria, MA Robb, JR Cheeseman, G Scalmani, V Barone, B Mennucci, GA Petersson, et al. Gaussian 09, revision A. 09; gaussian, inc: Wallingford, ct, 2009. 2009.

[193] R Torres, R De Nalda, and JP Marangos. Dynamics of laser-induced molecular alignment in the impulsive and adiabatic regimes: A direct comparison. *Physical Review A*, 72(2):023420, 2005.

[194] N Hay, R Velotta, M Lein, R de Nalda, E Heesel, M Castillejo, and JP Marangos. High-order harmonic generation in laser-aligned molecules. *Physical Review A*, 65(5):053805, 2002.

[195] S. Chatziathanasiou, I. Liontos, E. Skantzakis, S. Kahaly, M. Upadhyay Kahaly, N. Tsatrafyllis, O. Faucher, B. Witzel, N. Papadakis, D. Charalambidis, and P. Tzallas. Quantum path interferences in high-order harmonic generation from aligned diatomic molecules. *Physical Review A*, 100(6), December 2019.

[196] Igor V Litvinyuk, Kevin F Lee, Patrick W Dooley, David M Rayner, David M Villeneuve, and Paul B Corkum. Alignment-dependent strong field ionization of molecules. *Physical Review Letters*, 90(23):233003, 2003.

[197] Caterina Vozzi, Matteo Negro, Francesca Calegari, Giuseppe Sansone, Mauro Nisoli, Sandro De Silvestri, and Salvatore Stagira. Generalized molecular orbital tomography. *Nature Physics*, 7(10):822–826, 2011.

[198] Cheng Jin, Su-Ju Wang, Xi Zhao, Song-Feng Zhao, and CD Lin. Shaping attosecond pulses by controlling the minima in high-order harmonic generation through alignment of CO2 molecules. *Physical Review A*, 101(1):013429, 2020.

[199] Lotte Holmegaard, Jonas L Hansen, Line Kalhøj, Sofie Louise Kragh, Henrik Stapelfeldt, Frank Filsinger, Jochen Küpper, Gerard Meijer, Darko Dimitrovski, Mahmoud Abu-Samha, et al. Photoelectron angular distributions from strong-field ionization of oriented molecules. *Nature Physics*, 6(6):428–432, 2010.

[200] Henrik Stapelfeldt and Tamar Seideman. Colloquium: Aligning molecules with strong laser pulses. *Reviews of Modern Physics*, 75(2):543, 2003.

[201] Moshe Shapiro and Paul Brumer. *Principles of the quantum control of molecular processes*. Wiley VCH, 2003.

[202] Christiane P Koch, Mikhail Lemeshko, and Dominique Sugny. Quantum control of molecular rotation. *Reviews of Modern Physics*, 91(3):035005, 2019.

[203] Tamar Seideman. Revival structure of aligned rotational wave packets. *Physical Review Letters*, 83(24):4971, 1999.

[204] Juan Ortigoso, Mirta Rodrıguez, Manish Gupta, and Bretislav Friedrich. Time evolution of pendular states created by the interaction of molecular polarizability with a pulsed nonresonant laser field. *The Journal of Chemical Physics*, 110(8):3870–3875, 1999.

[205] Lotte Holmegaard, Simon S Viftrup, Vinod Kumarappan, Christer Z Bisgaard, Henrik Stapelfeldt, Edward Hamilton, and Tamar Seideman. Control of rotational wave-packet dynamics in asymmetric top molecules. *Physical Review A*, 75(5):051403, 2007.

[206] Peng Peng, Ya Bai, Na Li, and Peng Liu. Measurement of field-free molecular alignment by balanced weak field polarization technique. *AIP Advances*, 5(12):127205, 2015.

[207] Jing-Song Liu, Qi-Yuan Cheng, Da-Guang Yue, Xu-Cong Zhou, and Qing-Tian Meng. Influence factor analysis of field-free molecular orientation. *Chinese Physics B*, 27(3):033301, 2018.

[208] Kevin M Dunn, James E Boggs, and Peter Pulay. Vibrational energy levels of methyl fluoride. *The Journal of Chemical Physics*, 86(9):5088–5093, 1987.

[209] A. Owens, S. N. Yurchenko, W. Thiel, and V. Špirko. Enhanced sensitivity to a possible variation of the proton-to-electron mass ratio in ammonia. *Physical Review A*, 93:052506, May 2016.

[210] Sergei Kühn, Mathieu Dumergue, Subhendu Kahaly, Sudipta Mondal, Miklós Füle, Tamás Csizmadia, Balázs Farkas, Balázs Major, Zoltán Várallyay, Eric Cormier, et al. The ELI-ALPS facility: the next generation of attosecond sources. *Journal of Physics B: Atomic, Molecular and Optical Physics*, 50(13):132002, 2017.

[211] Rimantas Budriūnas, Tomas Stanislauskas, Jonas Adamonis, Aidas Aleknavičius, Gediminas Veitas, Darius Gadonas, Stanislovas Balickas, Andrejus Michailovas, and Arūnas Varanavičius. 53 W average power CEP-stabilized OPCPA system delivering 5.5 TW few cycle pulses at 1 kHz repetition rate. *Optics express*, 25(5):5797–5806, 2017.

[212] Kalyani Chordiya, Irén Simkó, Tamás Szidarovszky, and Mousumi Upadhyay Kahaly. Achieving high molecular alignment and orientation for CH3F through manipulation of rotational states with varying optical and THz laser pulse parameters. *Scientific Reports*, 12(1):1–10, 2022.

[213] Jozef Noga and Rodney J Bartlett. The full CCSDT model for molecular electronic structure. *The Journal of Chemical Physics*, 86(12):7041–7050, 1987.

[214] K. Raghavachari, G. W. Trucks, J. A. Pople, and M. Head-Gordon. A fifth-order perturbation comparison of electron correlation theories. *Chemical Physics Letters*, 157:479–483, 1989.

[215] John D Watts and Rodney J Bartlett. The coupled-cluster single, double, and triple excitation model for open-shell single reference functions. *The Journal of Chemical Physics*, 93(8): 6104–6105, 1990.

[216] D Papousek, Yen-Chu Hsu, Hann-Sen Chen, P Pracna, S Klee, and M Winnewisser. Far infrared spectrum and ground state parameters of $^{12}CH_3F$. *Journal of Molecular Spectroscopy*, 159(1):33–41, 1993.

[217] Takehiko Shimanouchi, Hiroatsu Matsuura, Yoshiki Ogawa, and Issei Harada. Tables of molecular vibrational frequencies part 10. *Journal of Physical and Chemical Reference Data*, 9(4):1149–1254, 1980.

[218] Uzi Even, J Jortner, D Noy, N Lavie, and C Cossart-Magos. Cooling of large molecules below 1 K and He clusters formation. *The Journal of Chemical Physics*, 112(18):8068–8071, 2000.

[219] Jonas Grzesiak, Manish Vashishta, Pavle Djuricanin, Frank Stienkemeier, Marcel Mudrich, Katrin Dulitz, and Takamasa Momose. Production of rotationally cold methyl radicals in pulsed supersonic beams. *Review of Scientific Instruments*, 89(11):113103, 2018.

[220] LV Keldysh et al. Ionization in the field of a strong electromagnetic wave. *Soviet Physics-JETP*, 20(5):1307–1314, 1965.

[221] J Moxom, J Xu, G Laricchia, LD Hulett, DM Schrader, Y Kobayashi, B Somieski, and TA Lewis. Fragmentation and ionization of CH3F by positron and electron impact. *Nuclear Instruments and Methods in Physics Research Section B: Beam Interactions with Materials and Atoms*, 143(1-2):112–120, 1998.

[222] Ci-Ling Pan, Chih-Hsuan Lin, Chan-Shan Yang, and Alexey Zaytsev. Laser ablation of polymethylmethacrylate (PMMA) by phase-controlled femtosecond two-color synthesized waveforms. In *Chapter*, volume 15, pages 335–358. IntechOpen, 2016.

[223] Keita Oda, Masafumi Hita, Shinichirou Minemoto, and Hirofumi Sakai. All-optical molecular orientation. *Physical Review Letters*, 104(21):213901, 2010.

[224] Irén Simkó, Kalyani Chordiya, Attila G. Császár, Mousumi Upadhyay Kahaly, and Tamás Szidarovszky. A quantum-chemical perspective on the laser-induced alignment and orientation dynamics of the CH3X (X = F, Cl, Br, I) molecules. *Journal of Computational Chemistry*, 43 (8):519–538, 2022.

[225] Min Zhang, Yinglin Wang, Mingfei Xu, Wentao Ma, Renzhi Li, and Peng Wang. Design of high-efficiency organic dyes for titania solar cells based on the chromophoric core of cyclopentadithiophene-benzothiadiazole. *Energy & Environmental Science*, 6(10):2944–2949, 2013.

[226] Yanyan Duan, Kalyani Chordiya, Mousumi Upadhyay Kahaly, Freddy E Oropeza, Víctor A de la Peña O'Shea, De-Yi Wang, and Rubén D Costa. Rational amphiphilic ligand engineering enables enhanced stability and efficiency of cspbbr3 nanocrystals based light emitting diodes. *Advanced Optical Materials*, page 2201176, 2022.

[227] He Zhao, Kalyani Chordiya, Petri Leukkunen, Alexey Popov, Mousumi Upadhyay Kahaly, Krisztian Kordas, and Satu Ojala. Dimethylammonium iodide stabilized bismuth halide perovskite photocatalyst for hydrogen evolution. *Nano Research*, 14(4):1116–1125, 2021.

[228] Jiangjian Shi, Yiming Li, Yusheng Li, Dongmei Li, Yanhong Luo, Huijue Wu, and Qingbo Meng. From ultrafast to ultraslow: charge-carrier dynamics of perovskite solar cells. *Joule*, 2(5):879–901, 2018.

[229] Swathi Erekath, Kalyani Chordiya, KV Vidhya, Mousumi Upadhyay Kahaly, and Sreeram K Kalpathy. Self-aggregation, h-bonding, and photoresponse in film and solution states

of azobenzene containing polyurea. *Physical Chemistry Chemical Physics*, 24(38):23447–23459, 2022.

[230] Ritu Rai, Zubair Ahmed, Rajinder Kumar, Rameshwar L Kumawat, Kalyani Chordiya, Takahiro Maruyama, Md Ehesan Ali, and Vivek Bagchi. Environmentally benign metal-free reduction of go using molecular hydrogen: A mechanistic insight. *ACS omega*, 3(11): 15112–15118, 2018.

[231] Vyacheslav V Kim, Rashid A Ganeev, Srinivasa Rao Konda, Ganjaboy S Boltaev, Ibrohim B Sapaev, Weili Yu, and Wei Li. High-order harmonics generation in the laser-induced lead-free perovskites-containing plasmas. *Scientific Reports*, 12(1):1–13, 2022.